İSTANBUL TECHNICAL UNIVERSITY ★ INSTITUTE OF SCIENCE AND TECHNOLOGY

REDOX BEHAVIOUR OF PLASMA SPRAYED METAL SUPPORTED SOFC

M.Sc Thesis by

Esra KUNT, B.Sc.

Department : Renewable Energy

Programme: Energy Science and Technology

JANUARY 2008

İSTANBUL TECHNICAL UNIVERSITY ★ INSTITUTE OF SCIENCE AND TECHNOLOGY

REDOX BEHAVIOUR OF PLASMA SPRAYED METAL SUPPORTED SOFC

M.Sc Thesis by

Esra KUNT, B.Sc Che. Eng.

(301051006)

Date of submission : 24 December 2007

Date of defence examination: 28 January 2008

Supervisors (Chairmans): **Assoc. Prof. Dr. Nesrin ALTINSOY**

Assoc. Prof. Dr. Nilgün KARATEPE YAVUZ

Members of the Examining Committee: **Prof. Dr. Figen KADIRGAN (I.T.U.)**

Assoc.Prof. Dr. Ali ATA (G.Y.T.U.)

Assoc. Prof. Dr. Filiz SAHIN (I.T.U.)

JANUARY 2008

İSTANBUL TEKNİK ÜNİVERSİTESİ ★ FEN BİLİMLERİ ENSTİTÜSÜ

TERMAL PLAZMA SPRAY TEKNİĞİ İLE ÜRETİLEN METAL DESTEKLİ KATI OKSİT YAKIT HÜCRELERİNİN REDOKS DAVRANIŞI

Yüksek Lisans TEZİ

Kim. Müh. Esra KUNT

(301051006)

Tezin Enstitüye Verildiği Tarih : 24 Aralık 2007

Tezin Savunulduğu Tarih : 28 Ocak 2008

Tez Danışmanları:	**Doç. Dr. Nesrin ALTINSOY**
	Doç. Dr. Nilgün KARATEPE YAVUZ
Diğer Jüri Üyeleri:	**Prof. Dr. Figen KADIRGAN (İ.T.Ü.)**
	Doç. Dr. Ali ATA (G.Y.T.Ü.)
	Doç. Dr. Filiz ŞAHIN (İ.T.Ü.)

OCAK 2007

FOREWORD

This Master Thesis was implemented at the German Aerospace Center (DLR) Stuttgart from 6th November 2006 to 19th July 2007, in order to complete the Master of Science Degree at the Istanbul Technical University, in Istanbul. The experiments described in this work were performed at the DLR Stuttgart. I would like to acknowledge Dr. Arnould from DLR - Stuttgart for giving me the opportunity to realize my thesis at DLR and for their continuous support. I especially owe my thanks to Dr. Syed from DLR Stuttgart who was the project advisor and who helped me throughout the project with his ideas and suggestions.

I would also like to thank Assoc. Prof. Dr. Nesrin ALTINSOY and Assoc. Prof. Dr. Nilgün KARATEPE YAVUZ from Istanbul Technical University for being my institute supervisor to write my thesis. Their help greatly improved this work.

I owe my special thanks to M.Sc. Zeynep İlhan who never hesitated to share her limited time, his precious knowledge and his experience on SOFCs during the period of this thesis. I would like to extend my acknowledgements to my colleagues Mr. Olaf Patz, Ms. Auer, Mr. Franco and Mr. Szabo, for their share of knowledge and experience and Mr. Rückdäschel, Mrs. Plock, for their technical support.

I would like to thank to my friends, Duygu, Utkan, Umut who supported with their friendships during my work. I would also give my special thanks and sincere gratitude to my friend Serdar who always with me in Germany. Finally, I would like to express my sincere gratitude and love to my mother Hafize, my father Muzaffer, my brother Nevrah and his wife Melike for their endless support all my life long.

January, 2008 ESRA KUNT

TABLE OF CONTENTS

ABBREVIATIONS

AC : Alternating Current
AFC : Alcaline Fuel Cell
APS :Air plasma spraying
APU : Auxiliary Power Unit
BOP : Balance of Plant
CAPS : Control pressure plasma spraying
CEA : Cathode, Electrolyte and Anode
CPE : Constant Phase Element
DC : Direct Current
DLR : Deutsches Zentrum für Luft- und Raumfahrt e.V.
EIS : Electrochemical Impedance Spectroscopy
I-V : Current Density vs. Voltage
ITT : Institut of Technical thermodynemic
MEA : Membrane-electrolyte-assembly
MIEC : Mixed ionic electronic Conductivity
LSCF : Strontium doped Lanthanum Cobalite
LSF : un-doped $LaFeO_3$
LSM : Strontium doped Lanthanum Manganite
LPPS : Low pressure plasma spraying
OCV : Open Circuit Voltage
PEMFC : Polymer Electrolyte Membrane Fuel Cell
PLC : Programmable Logic Controller
PM : Powder Metallurgically
RT : Room Temperature
SEM : Scanning Electron Microscopy
SLPM **:** Standard Liter per Minute
SOFC : Solid Oxide Fuel Cell
TEC : Thermal Expansion Coefficient
TPB : Triple Phase Boundary
UTC : United Technologies Corporation

VEE : Visual Engineering Environment

VPS : Vacuum Plasma Spraying

YSZ : Yttrium Stabilized Zirconia

ZeuS : Zellen und Stacks – Cells and Stacks

LIST OF TABLES

Sayfa No

LIST OF FIGURES

NOMENCLATURE

A^o	**:** Pre-exponential factor
A	**:** Area of a cell
e	**:** The flow-through thickness of the sample [m],
E_{rev}	**:** Reversible open circuit voltage
E_a	**:** Activation energy
F	**:** Faraday constant
ΔG°	**:** Change in Gibbs free enegy at standard conditions
ΔH°	**:** Change in reaction enhalpy at standard conditions
ΔG	**:** Change in Gibbs free enegy
ΔH	**:** Change in reaction enhalpy
I	**:** Electric current
i	**:** Electric current density
$i_\circ$	**:**Exchange Current Density
Ǐ	**:** Current amplitude
Im (Z)	**:**Imaginary part of impedance
k	**:**The Boltzmann constant
k_f0, k_r0	**:** Kinetic parameters for forward and reverse reactions
L	**:** Length
n	**:** Number of electrons
N_A	**:** Avogadro number
P	**:** Partial pressure of gas
Δp	**:** Pressure difference across the sample
R	**:** Gas constant
$R_{contact}$	**:** Contact resistance
R_{pol} (A)	**:** Polarization resistance at anode
R	**:** Electrolyte resistance
R Ω	**:** Ohmic resistance
Re Z	**:** Real part of impedance
Q	**:** Volume flow under the sample
j	**:** the complex number

T	**:** Temperature
Δt	**:** The change in time
Ŭ	**:** Voltage amplitude
V(i)	**:** Voltage measured as a function of current density
V	**:** Evucated Volume
Y'_{Zr}	**:** Y^{3+} -ion at the Zr^{4+} site, negatively charged
$V^{\cdot}_{0}$	**:** Oxide ion vacancy at electrolyte lattice, positively charged
O^{X}_{O}	**:** Oxide ion at the regular place in the oxide ion lattice
V_{cell},V_{open}	**:** Voltage at cell,OCV
$V_{act,ohm,conc}$	**:** Voltage losses from activation, ohmic, concentration
W_e	**:** Electrical Energy
Z	**:** Impedance
σ_i	**:** Ionic conductivity
σ_{el}	**:**Electrical conductivity
η	**:** Dynamic viscosity of the test fluid
η_{act}	**:** Activation Efficiency
η_{ohm}	**:** Ohmic Efficiency
η_{conc}	**:** Concentration Efficiency
η_{th}	**:** Thermodynamic efficiency
η_{el}	**:** Current or Faraday Efficiency
η_j	**:** Voltage Efficiency
η_{aD} ,η_{cD}	**:** Diffusion polarization (of anode and cathode respectively)
ρ_e, ρ_a, ρ_c	**:** Resistivity (of electrolyte, anode and cathode respectively)
l_e , l_a , l_c	**:** Thickness (electrolyte, anode and cathode respectively)
ϕ	**:** Phase angle
α	**:** Charge Transfer Coefficient
θ_R	**:** i and θ_P,j are reactant and product surface coverages

TERMAL PLAZMA SPRAY TEKNİĞİ İLE ÜRETİLEN METAL DESTEKLİ KATI OKSİT YAKIT HÜCRELERİNİN REDOKS DAVRANIŞI

ÖZET

Bu çalışmada, nano boyutlu Ni+YSZ malzemesinden oluşan anot bileşeni termal plazma sprey metodu ile üretilmiştir. Termal plazma sprey teknolojisi pek çok üstünlüklere sahiptir. Bu üstünlüklere örnek olarak; kısa üretim zamanı, kolay otomasyon ve kaliteli hücre bileşeni üretimi sayılabilir. Termal plazma sprey metodu, özellikle nano boyuttaki parçacıkların farklı değişkenler ile yakıt hücresi bileşenlerinin üretilmesinde kullanılır. Bu sayede yüksek verimlilik, daha sıkı anot ve elektrolit yapısı redoks döngüsü altında beklenir.

Yakıt hücresinde ana elemanlardan biri anottur. Anot yakıtı elektrokimyasal reaksiyon için üçlü faz bölgesine taşıyan aynı zamanda üçlü faz bölgesinde oluşturulan ürün ve elektronların geri taşınmasında görevlidir. Genel olarak kullanılan anot malzemesi Nikel ve YSZ oluşan sermet yapıdır, uzun dönem dayanıklılığından ve ticari olarak uygunluğundan ötürü. Nikel çok iyi katalitik aktivitesi ve yüksek elektronik iletkenliği vardır. Buna rağmen, nikelin termal uzama katsayısı elektrolit ile uyumsuzluk gösterir ve nikel yüksek sıcaklıkta tanecikli yapı oluşumu gösterir. YSZ, nikelin çevresine eklenerek, bu problemler kısıtlanır. Ni/YSZ tanecik boyutu, hâkim oranı, dağılımı önemli parametrelerdir. Bu parametreler ile içsel direnç, gözeneklilik, aktif yüzey alanı, kayıp direnci belirlenir. Dahası sermet yapı hem iyonik hem de elektronik iletkenlik gösterir, bu da elektrokimyasal reaksiyonların alanını artırır, daha düşük kayıplara sebep olur.

Redoks döngüsünden kaynaklanan hacim değişikliği sonucunda ciddi performans düşüklüğü beklenmektedir. Bunun sebebi anot ve elektrolit yüzeyindeki çatlamalar ve kırılmalardan kaynaklanan kayıplardandır. Yapılan tez çalışmasında redoks döngüsü esnasında bu tip hücrelerde çok az çatlama ya da hiç çatlama olmaması beklenmiştir. Bu amaçla, hücreler fırın içerisinde beş defa farklı sayılarda redoks döngüsüne maruz bırakılmış ve her çalışmada farklı hücreler kullanılmıştır. İlk çalışmada sadece indirgenme, ikincisinde bir indirgenme ve bir redoks, üçüncüsünde bir indirgenme ve beş redoks, dördüncüsünde bir indirgenme ve on redoks, beşincisinde bir indirgenme ve onbeş redoks uygulanmıştır. Redoks çalışmalarında kullanılan hücrelerin sızıntı ve geçirgenlikleri ölçülerek elektrokimyasal analizlerden çıkan sonuçlar ile karşılaştırılmıştır. Ayrıca, taramalı elektron mikroskobu (SEM) ile mikro yapılarındaki değişimler incelenmiştir. Mikroyapısal ve elektrokimyasal testlerinin sonuçları karşılaştırıldığında termal plazma sprey ile üretilmiş olan nanoyapılı Nİ+YSZ anot bileşeninin yüksek verimlilik, etkin reaksiyon yüzeyi, daha sıkı anot ve elektrolit yapısına sahip olduğu tespit edilmiştir. Sonuç olarak bu çalışma hücrede redoks işlemi boyunca az çatlama olduğunu yada hiç çatlama olmadığını göstermektedir

REDOX BEHAVIOUR OF PLASMA SPRAYED METAL SUPPORTED SOFC

SUMMARY

In this study, nanostructured Ni+YSZ anode layers are fabricated by air plasma spray. Air plasma spray is the one of the cell production technique which has discrete advantages such as, short fabrication time, simple automation and quality of cell layers. Especially, nano particle size can be produced with different parameters (pressure, NiO/YSZ weight ratio, etc) by thermal plasma spray. By this way, higher cell performance and much closer structure with anode and electrolyte are predictable under Redox Cycle.

One of the basic components of SOFC is anode, which brings fuel for electrochemical oxidation at the triple phase boundary, takes back the reaction products and transports electrons from reaction site to the external circuit. Nickel and yttria stabilized zirconia cermet is the most commonly used anode material due to its long term stability and commercial availability. Nickel has excellent catalytic activity and high electronic conductivity. However, the coefficient of thermal expansion (CTE) of nickel mismatches with that of electrolyte (normally fully stabilized YSZ) and nickel may agglomerate at operation temperature. YSZ is added around the Nickel particles in order to counter these issues. Ni/YSZ particle size, volume ratio and distribution are the important parameters for defining the internal resistance, porosity, active surface area and polarization resistance of the anode functional layer. Moreover, the cermet behaves as a mixed ionic electronic conductor (MIEC), increasing the active area for electrochemical reactions and combined with large internal surface in the porous structure may lead to low overpotential.

However, YSZ-Ni anode layer suffers from redox (reduction-oxidation) cycling. Ni can re-oxidize owning to numerous reasons such as switching off the system, breaking off the fuel supply, seal leak, etc, thus it is paramount to be reduced before the operation. During redox cycle nickel has a noticeable bulk volume change. The volume change due to the redox cycles may cause significant degradation of performance of the SOFC because of micro cracking of anode and electrolyte and delamination at the anode-electrolyte interface. According to that, the approach of this thesis is less or no cracking with this type of cell during the redox cycle. Though the porosity of the anode functional layer in the SOFC may compensate for some of this volume change, significant volume changes were previously reported. To demonstrate this approach, there are applied five runs of redox cycles in the furnace; first run was only reduction, second run was one reduction and 1 redox, third run was one reduction and 5 redox, forth run was one reduction and 10 redox, fifth run was one reduction and 15 redox. Redox cycled cells were compared with electrochemical

analyse by using leak rate and permeability measurements. In addition, microstructures changes are studied by SEM analyse. The microstructural and the elecrochemical test results were proved that the nanostructured Ni+YSZ anode layers fabrication with the thermal plasma spray had high cell performance, efficient cell reactions surface and much closer structure with anode and electrolyte. In conclusion, this study determined that nanostructured anode provided less or no cracking and delamination on the cell during the redox cycles.

1. INTRODUCTION

Because of their potential to reduce the environmental impact and geopolitical consequences of the use of fossil fuels, fuel cells have emerged as attractive alternatives to combustion engines. Like a combustion engine, a fuel cell uses some sort of chemical fuel as its energy source; but like a battery, the chemical energy is directly converted to electrical energy, without a relatively inefficient combustion step. Several classifications of fuel cells have appeared in the literature throughout the years. The most prevailing one is based on the type of the electrolyte. Fuel cells are grouped into five different types according to electrolyte structure. These are Polymer Electrolyte Membrane Fuel Cell, Alkaline Fuel Cell, Phosphoric Acid Fuel Cell, Molten Carbonate Fuel Cell and Solid Oxide Fuel Cell.

Solid oxide fuel cells (SOFC) allow conversion of a wide range of fuels, including various hydrocarbon fuels. The relatively high operating temperature allows for highly efficient conversion to power, internal reforming, and high quality by-product heat for cogeneration or for use in a bottoming cycle. Indeed, both simple-cycle and hybrid SOFC systems have demonstrated among the highest efficiencies of any power generation system, combined with minimal air pollutant emissions and low greenhouse gas emissions. These capabilities have made SOFC an attractive emerging technology for stationary power generation in the 2 kW to 100s MW capacity range. Solid oxide fuel cells (SOFCs) represent a very ambitious application of ceramic materials, with challenging issues ranging from processing, electrochemistry, thermodynamics, and solid state ionics to mechanics and design.

The master thesis has been carried out at the German Aerospace Center (DLR) at its Institute of Technical Thermodynamics (ITT) in Stuttgart, as part of the European Real-SOFC-Project. The aim of the Integrated Project Real-SOFC is to solve the persisting problems of ageing with planar Solid Oxide Fuel Cells (SOFC) in a concerted action of the European fuel cell industry and research institutions. This includes gaining full understanding of degradation processes, finding solutions to reduce ageing and producing improved materials that will then be tested in stacks. In

this process further consideration will be given to the design of cost effective materials, low cost components and optimised manufacturing processes. The partnership includes research institutes and companies from twelve European Countries. The Real-SOFC-Project is supported by the European Commission as part of the FP6 energy programme.

The German Aerospace Research Centre (DLR) is the largest engineering research organisation in Germany with about 4,500 employees. It belongs to the Helmholtz-Society. DLR undertakes applied research and development in the divisions' space flight, aeronautics, energy and transport.

The DLR-Institute of Technical Thermodynamics in Stuttgart, Germany, belongs to the division energy. It is mainly active in the field of renewable energy research and technology development for efficient and low emission energy conversion and utilisation. Staff of about 140 is working in the divisions Electrochemical Energy, Thermal Process Technology, SolarThermal Energy and System Analyse.

At DLR Stuttgart a new thin-film concept has been carried out. The entire membrane-electrolyte-assembly (MEA) is deposited onto a porous metallic substrate by an integrated multi-step vacuum plasma spray (VPS) process. This process enables the production of an electrolyte layer with a thickness of 20-30µm, which in comparison with the electrolyte-supported concept where electrolytes have to be a mechanical support, means a 60-80 µm reduction. This high reduction leads to an increase in the power density and a reduction of the cell ohmic losses.

At DLR a novel design of a planar thin-film SOFC was developed in order to reduce the operating temperature below 800°C. In this new concept the functional layers are deposited onto a porous metallic substrate using an integrated multistep air plasma spraying process. The thickness of the overall cell is reduced to approximately 160 µm.

The present work nanostructured Ni+YSZ anode layers were fabricated by vacuum plasma spray. Vacuum plasma spray is the one of the cell production technique which has discrete advantages such as, short fabrication time, simple automation and quality of cell layers. Different parameters of thermal plasma spray affect the quality of cell components which have nano particle size. With this technique, higher cell performance and much closer structure with anode and electrolyte are anticipated.

The aim of this study is to demonstrate that less or no cracking and high cell performance of this type of cell during the redox cycle. For this purpose, the effects of redox cycle on the electrochemical performance of full cell are compared with the redox cycle effects on the half cell by using leak rate and permeability measurements. In addition, microstructural changes are studied by SEM analyse.

2. FUEL CELLS

Fuel cells are energy conversion devices assuring power generation with high efficiency and low environmental effect. Different types of chemical fuel are used for supplying energy as similar as traditional combustion engine; on the other hand the important difference between combustion engine and fuel cell is inefficient intermediate. These steps are not necessary to produce electrical energy for fuel cell. When fuel cells are operating, pollutant gas emissions are at low level to the atmosphere. Moreover, at operation condition, they do not make any noise if subsystem is ignored, while balance of plant contains moving parts. One of the most appealing aspects of the fuel cell is its inherent modularity both its efficiency and cost per unit power are relatively insensitive to its size. This allows a wide range of applications from large power plants to power supplies for laptop computers [1].

2.1 History

The first fuel cell was invented by Sir William Grove in 1839. The cell was derived by two platinum electrodes surrounded by closed tubes. Those two platinum were soaked into dilute acid, were as an electrolyte. Additionally, hydrogen and oxygen were in closed tubes. Water was electrolyzed into hydrogen and oxygen by passing on electric current through the external lines. In 1889, L.Mond and C. Legner generated the first alkaline fuel cells and this application was the first patent in the fuel cell area [2]. At fifties, Nerst and his colleagues built the first operated fuel cell, its capacity was nearly 5 KW. As a result of this development, long term fuel cell research program has been started and continued until these days [3]. Additionally, W. Schottly invented the theoretical basic for solid oxide fuel cell, after that, E. Bauer and H. Preis reported to the first experimental work about SOFC relatively with the theoretical knowledge. The chronological steps of fuel cells can be seen in the Table 2.1 [4].

Table 2.1 Fuel cell developments by chronologically [4]

Years	Development of Fuel cell
1838	C.F. Schönbein "On the Voltaic Polarization of Certain Solid and Fluid Substance"
1839	R.W. Grove "On the Voltaic Series and Combination of Gasses by Platinum"
1843	Construction of a Gas Battery
1889	Work by L. Mond and C. Langer result in first alkaline
1896	W.W. Jaques used molten sodium hydroxide as the electrolyte intending direct conversion of coal
1900	W. Nerst conceptual work in the field of solid oxide fuel cell
1905	F. Haber carried out systematic thermodynamic investigations of hydrogen consuming fuel cells
1932	F.T. Bacon started a long term fuel cell research program
1935	W. Schottky developed the theoretical basics of the SOFC
1938	E. Baur and H. Preis reported on experimental SOFC-work
1959	F.T. Bacon built the first working 5 kW alkaline fuel cell stack
1964	Polymer Electrolyte membrane fuel cell supplied electricity to Gemini spacecraft
1967	Concept of phosphoric acid fuel cell (PAFC) by UTC
1960/80ies	Alkaline fuel cell were used for Apollo and Space Shuttle
1984	Rediscovery of Polymer electrolyte membrane fuel cell (Siemens/Ballard)

2.2 Definition of Fuel Cells

The most common characterization of fuel cell is an electrochemical device that directly converts chemical energy, from a reaction between a fuel and an oxidant, into electrical energy. As can be seen from the Figure 2.1, the basic structure fuel cells consist of three major component; porous cathode, porous anode and non-porous electrolyte.

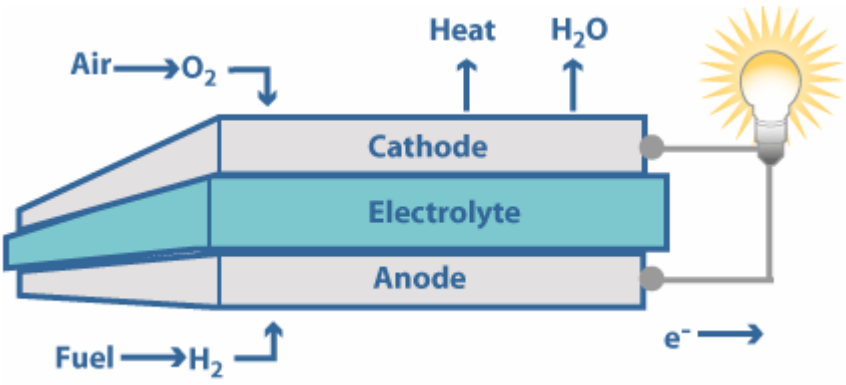

Figure 2.1 Schematic presentation of a planar fuel cell [5]

In a standard fuel cell, fuel is fed permanently to the anode and an oxidant (generally oxygen from air) is fed permanently to the cathode. Hydrogen is oxidized in the anode and oxygen is reduced in the cathode. External work is done by flow of electrons from anode to cathode through the external circuit; as a result, electrical energy is existed. There is an overall chemical driving force to occur a reaction between the oxygen and the hydrogen for producing water and heat.

The fuel and oxidant gasses are diffused through the electrode and they reach to the boundary of the electrolyte and the electrode where the electrochemical reactions are occurred. It is called three-phase-boundary region which is comprised from gas and electrolyte-electrode interface. Chemical energy can be converted to the electrical energy as long as fuel and oxidant are continuously supplied to the electrode. Sort of fuels can be used for anode, such as hydrogen, ethanol, methanol, or gaseous fossils. However solid or liquid fossil fuels need to be gasified first before they can be used as fuel [6].

2.3 Fuel Cell Stack System

For most practical fuel cell applications, unit cells must be combined in a modular fashion into a cell stack to achieve the voltage and power output level required for the application. Generally, the stacking involves connecting multiple unit cells in series via electrically conductive interconnects. Different stacking arrangements have been developed, which are described below.

2.3.1 Planar-Bipolar Stacking

The most common fuel cell stack design is the so-called planar-bipolar arrangement (Figure 2.2 depicts a PAFC). Individual unit cells are electrically connected with interconnects. Because of the configuration of a flat plate cell, interconnect becomes a separator plate with two functions:

1) To provide an electrical series connection between adjacent cells, specifically for flat plate cells, and

2) To provide a gas barrier that separates the fuel and oxidant of adjacent cells.

In many planar-bipolar designs, interconnect also includes channels that distribute the gas flow over the cells. The planar-bipolar design is electrically simple and leads to short electronic current paths (which helps to minimize cell resistance).

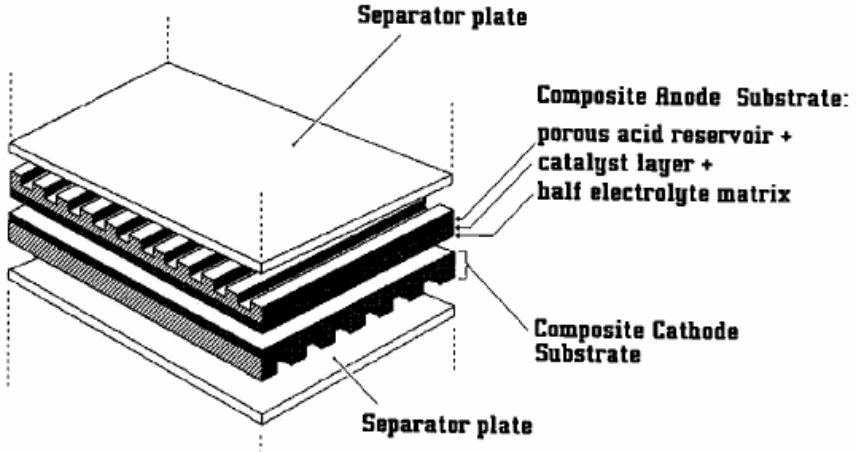

Figure 2.2 Expanded View of a Basic Fuel Cell Unit in a Fuel Cell Stack [7]

Planar-bipolar stacks can be further characterized according to arrangement of the gas flow:

- Cross-flow: Air and fuel flow perpendicular to each other
- Co-flow: Air and fuel flow parallel and in the same direction. In the case of circular cells, this means the gases flow radically outward
- Counter-flow: Air and fuel flow parallel but in opposite directions. Again, in the case of circular cells this means radial flow
- Serpentine flow: Air or fuel follow a zig-zag path
- Spiral flow: Applies to circular cells

The choice of gas-flow arrangement depends on the type of fuel cell, the application, and other considerations. Finally, the manifolding of gas streams to the cells in bipolar stacks can be achieved in various ways:

- Internal: the manifolds run through the unit cells
- Integrated: the manifolds do not penetrate the unit cells but are integrated in the interconnects
- External: the manifold is completely external to the cell, much like a wind-box

2.3.2 Stacks with Tubular Cells

Especially for high-temperature fuel cells, stacks with tubular cells have been developed. Tubular cells have significant advantages in sealing and in the structural integrity of the cells. However, they represent a special geometric challenge to the stack designer when it comes to achieving high power density and short current paths. In one of the earliest tubular designs the current is conducted tangentially around the tube. Interconnects between the tubes are used to form rectangular arrays of tubes. Alternatively, the current can be conducted along the axis of the tube, in which case interconnection is done at the end of the tubes. To minimize the length of electronic conduction paths for individual cells, sequential series connected cells are being developed. The cell arrays can be connected in series or in parallel.

To avoid the packing density limitations associated with cylindrical cells, some tubular stack designs use flattened tubes.

2.3.3 The Fuel Cell Systems

In addition to the stack, practical fuel cell systems require several other sub-systems and components; the so-called balance of plant (BoP). Together with the stack, the BoP forms the fuel cell system. The precise arrangement of the BoP depends heavily on the fuel cell type, the fuel choice, and the application. In addition, specific operating conditions and requirements of individual cell and stack designs determine the characteristics of the BoP. Still, most fuel cell systems contain:

Fuel preparation; Except when pure fuels (such as pure hydrogen) are used, some fuel preparation is required, usually involving the removal of impurities and thermal conditioning. In addition, many fuel cells that use fuels other than pure hydrogen require some fuel processing, such as reforming, in which the fuel is reacted with some oxidant (usually steam or air) to form a hydrogen-rich anode feed mixture.

Air supply; In most practical fuel cell systems, this includes air compressors or blowers as well as air filters.

Thermal management; All fuel cell systems require careful management of the fuel cell stack temperature.

Water management; Water is needed in some parts of the fuel cell, while overall water is a reaction product. To avoid having to feed water in addition to fuel, and to ensure smooth operation, water management systems are required in most fuel cell systems.

Electric power conditioning equipment; Since fuel cell stacks provide a variable DC voltage output that is typically not directly usable for the load, electric power conditioning is typically required.

While perhaps not the focus of most development effort, the BoP represents a significant fraction of the weight, volume, and cost of most fuel cell systems.

Figure 2.3 shows a simple rendition of a fuel cell power plant. Beginning with fuel processing, a conventional fuel (natural gas, other gaseous hydrocarbons, methanol, naphtha, or coal) is cleaned, then converted into a gas containing hydrogen. Energy conversion occurs when DC electricity is generated by means of individual fuel cells combined in stacks or bundles. A varying number of cells or stacks can be matched

to a particular power application. Finally, power conditioning converts the electric power from dc into regulated dc or ac for consumer use [7].

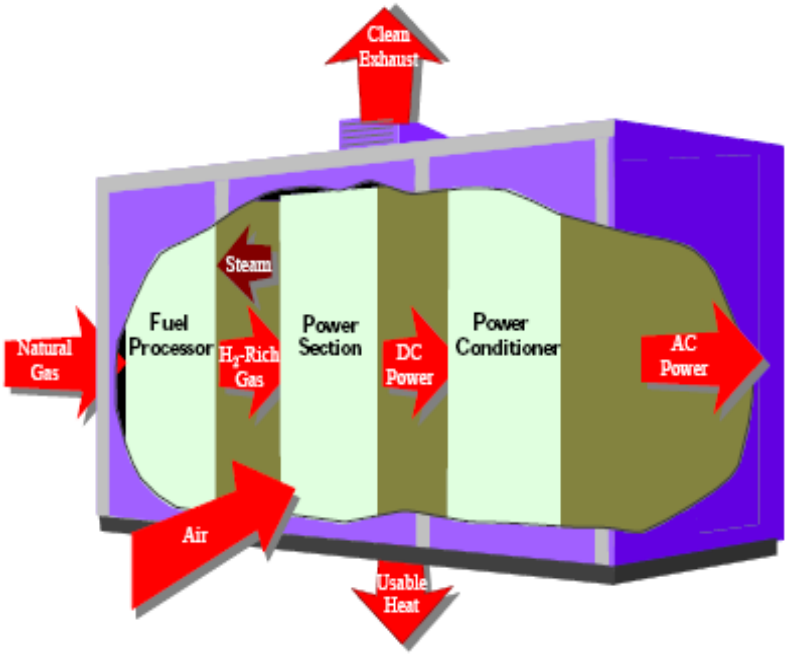

Figure 2.3 Fuel Cell Power Plant Major System [7]

2.4 The Types of Fuel Cells

Fuel Cells are grouped into five different types, generally named from their electrolyte structure. Fuel Cells are basically differenced from material of electrolyte; on the other hand the choice of electrolyte material depends on the operational temperature and the type of fuel and oxidant. Figure 2.4 describes the basic fundamental differences, for example the specific reactions at the anode and cathode, the source of oxidant and fuel as well as the operating temperature of the fuel cells for the optimal performance.

For the reasons of electrode activity (which translates into higher efficiency and fuel flexibility), higher temperature operation is preferred. However, for portable (intermittent) power applications, lower temperature operation is typically favored as it enables rapid start up and minimizes stresses due to thermal cycling. In this sense, the types of fuel cells are summarized in detail; it can be seen in the Table 2.2.

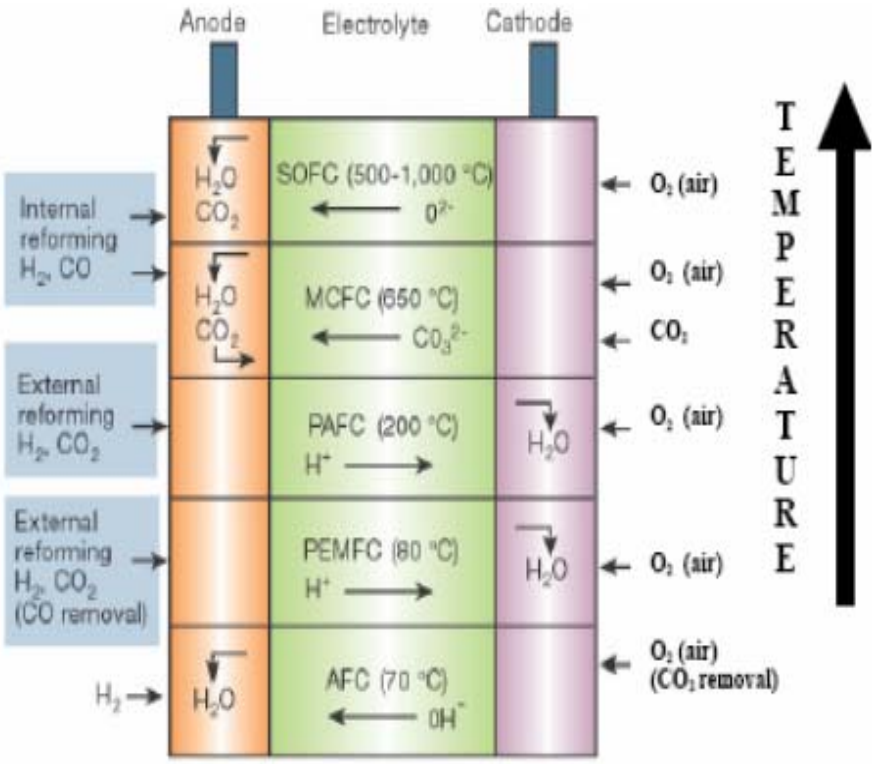

Figure 2.4 Types of fuel cells and their respective [8]

Table 2.2 Different fuel systems along with operating temperature and electrolyte [7]

	SOFC	PEMFC	MCFC	AFC	PAFC
Anode	Ni-YSZ Cermet	Pt black or Pt/C	Ni-10%Cr	Ni	Pt/C
Cathode	Sr-doped $LaMnO_3$	Pt black or Pt/C	Li-doped NİO	Li-doped NİO	Pt/C
Electolyte(mol%)	Yttria Stabilized ZrO_2(YSZ)	Nafion	62 Li_2Co_3-38K_2CO_3	85%KOH	100%H_3PO_4
Fuel	H_2,CO,CH_4	H_2 pure	H_2, CO, CH_4, C_3H_8	H_2,O_2	H_2 reformed natural gas
Charge carrier	O^{2-}	H^+	CO_3^{2-}	OH^-	H^+
Pressure(MPa)	0,1	0,1-0,5	0,1-1	~0,4	0,1-1
Temperature©	600-1000	60-80	650	65-200	200
Anode Reaction	$H_{2(g)}+O^{2-} \longrightarrow H_2O(g)+2e^-$	$H_2(g) \longrightarrow 2H^+(ag)+2e^-$	$H_{2(g)}+CO_3^{2-} \longrightarrow H_2O_{(g)}+CO_2+2e^-$	$H_{2(g)}+2(OH)^+_{(ag)} \longrightarrow H_2O(g)+2e^-$	$H_{2(g)} \longrightarrow 2H^+_{(ag)}+2e^-$
Cathode Reaction	$1/2O_{2(g)}+2e^- \longrightarrow O^{2-}$	$1/2O_{2(g)}+2H^-_{(ag)}+2e^- \longrightarrow H_2O(g)$	$1/2O_{2(g)}+CO_{2(g)}+2e \longrightarrow CO_3^{2-}$	$1/2O_{2(g)}+H_2O_{(g)}+2e^- \longrightarrow 2(OH)^-_{(ag)}$	$1/2O_{2(g)}+2H^-_{(ag)}+2e \longrightarrow H_2O$
Cell Reaction	$H_{2(g)}+1/2O_{2(g)} \longrightarrow H_2O_{(g)}$	$H_{2(g)}+1/2O_{2(g)}+CO_2 \longrightarrow H_2O_{(l)}+CO_2$	$H_{2(g)}+1/2O_{2(g)}+CO_{2(g)} \longrightarrow H_2O_{(g)}+CO_{2(g)})$	$H_{2(g)}+1/2O_{2(g)} \longrightarrow H_2O_{(g)}$	$H_{2(g)}+1/2O_{2(g)}+CO^2 \longrightarrow 2O_{(g)}+CO_2$
System Efficiency	60-85% (with cogeneration)	50-60%	60-85%	50-70%	55%

2.4.1 Polymer Electrolyte Membrane Fuel Cells

The mainly application fields of Polymer electrolyte Membrane fuel cells are space technology, vehicle propulsion, and portable electronic devices as well as, combined heat and power generators. The size of typical modules is approximately between 0.1-100 kW. PEMFC has the highest power density and efficiency than the other types of fuel cells. It has the fastest start up capability; in addition it could work with high efficiency at the low temperature. Besides that, expensive platinum catalyst and also insensitivity of CO and other contaminant are the weak points, which are under the investigation.

2.4.2 Alkaline Fuel Cells

Alkaline fuel cells were used for space application for long time and the first example was experienced in Apollo spacecraft. It was provided both electricity and drink water. Another application area is vehicle propulsion. The most important advantages of AFC are that; they have the lowest voltage losses at cathode, so the efficiency is at high level and non-noble metal can be used as catalyst. However it has poor tolerance to CO_2, moreover pure H_2 and O_2 are required without any contaminant.

2.4.3 Phosphoric Acid Fuel Cells

PAFC has a big difference from other type of fuel cell due to the 'commercial availability'. Their lifetime is around 40000 hours; thereby they have an excellent reliability for long term performance. Generally, they are used with combined heat and power generation. The size of commercial module is approximately 200 kW. Besides these positive behaviours, they have limited efficiency and also they are very sensitive to $CO_{(g)}$ and Sulfur.

2.4.4 Molten Carbonate Fuel Cells

The most common fields of application is stationary application, moreover the efficiency is at high level (% 60-85) with combined heat and power generation or combined power plant with gas turbine. The differences from the other types of fuel cells are high $CO_{(g)}$ tolerant and flexibility in regards to fuel kinds. It operates at high temperature; so that inexpensive electro-catalysts are acceptable. For instance, nickel exhibits high adequate activity at high temperature. Furthermore, complex gas

management is necessary for this system, especially CO_2-recycling because of corrosive electrolyte material. Apart from that, it is only possible to start at elevated temperature.

2.4.5 Solid Oxide Fuel Cells

Mainly, it operates at high temperatures, on the grounds of that, it has high efficiency with combined heat and power generator or combined power plant with gas turbine. It is possible to use direct natural gas without reforming and also it has a tolerant with CO. Controlling gas circulation is important point for this kind of fuel cells [4,9]. SOFC and its component “anode” is the subject of this master thesis. It will be explained in details in the following chapter.

3. SOLID OXIDE FUEL CELLS

Solid oxide fuel cells are composed with three main parts; two of them are permeable electrodes which are called cathode and anode. The other one is impermeable electrolyte which is placed between two electrodes. Operation principle of SOFC basically depends on reduction and oxidation cycling. When oxidant is reached to cathode, oxygen is reduced to their ions, as shown Equation 3.1. The oxygen ions are diffused into electrolyte interface and they removed to the direction of anode through the electrolyte. At the boundary of anode and electrolyte interface the oxygen ions come upon with hydrogen and hydrogen is oxidized by the oxygen ions, as shown Equation 3.2. As a result, water, heat, and electrons are generated at the total of these reactions (Equation 3.3). Afterwards, electrons are migrated through to the external circuit; therefore this migration is ensured the electrical energy [3]. The operation principle of SOFC can be seen in the Figure 3.1

Cathode: $$\frac{1}{2}O_2 + 2e^- \rightarrow O^{-2} \quad (3.1)$$

Anode: $$H_2 + O^{2-} \rightarrow H_2O + 2e^- \quad (3.2)$$

Overall: $$H_2 + \frac{1}{2}O_2 \rightarrow H_2O \quad (3.3)$$

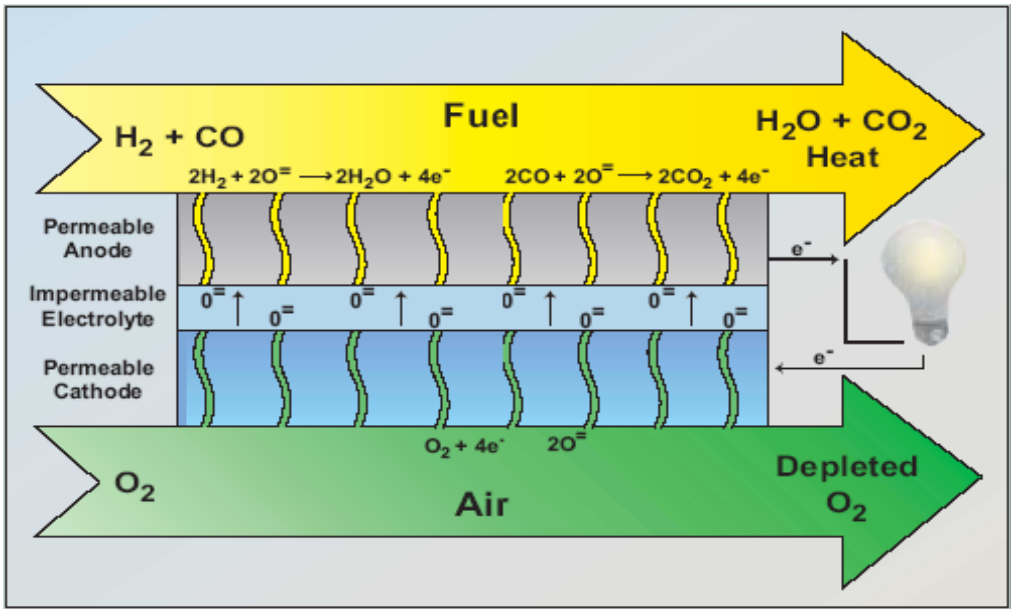

Figure 3.1 Operating principle of a Solid Oxide Fuel Cell [10]

3.1 The role of Gibbs free energy and Nernst Potential

The aim of fuel cell is to release the internal energy from fuel and convert it into electric and heat energy with high efficiency. The maximum amount of energy is obtained by the conception of ideal performance. The key parameter of the ideal performance is to analyze the process which takes place thermodynamically. Gibbs free energy and Nernst Potentials are used to determine the ideal condition of the system without any losses [11-12].

The total energy released in any chemical reaction is equal to the change in the enthalpy of formation (ΔH). This change in the enthalpy of formation is equal to the sum of the enthalpy of formation for the products minus the sum of the enthalpy of formation reactants. [13].

$$\Delta H = \sum (\Delta H) products - \sum (\Delta H) reac\tan ts \qquad (3.4)$$

Theoretically, all amount of reaction energy in enthalpy of formation could be converted into electrical energy, if none of it is converted into another form of energy. However, in a reversible reaction some of the chemical energy is converted into thermal energy and only the rest could be converted into electrical energy. The minimum amount of thermal energy that is generated in any reversible reaction at

constant temperature is $T\Delta S$. This is explained that the amount of produced electrical energy (W_e) in the fuel cell;

$$W_e \leq \Delta H - T\Delta S \tag{3.5}$$

Gibbs free energy G is a thermodynamic function that is defined as the enthalpy H minus the product of temperature and entropy S;

$$G = H - TS \tag{3.6}$$

In differential form above equation for an isothermal operation becomes

$$\Delta G = \Delta H - T\Delta S \tag{3.7}$$

In other words;

$$W_e \leq \Delta G \tag{3.8}$$

For the general chemical reaction;

$$aA + bB \rightarrow cC + dD \tag{3.9}$$

Where the change in Gibbs free energy for a given reaction (3.10);

$$\Delta G = \sum (\Delta G)_{products} - \sum (\Delta G)_{reac\tan ts} \tag{3.10}$$

Gibbs free energy depends on temperature and pressure, at which reaction occurs, as shown in the following equation (3.11),

$$G = G^{\circ} + RT \ln P \tag{3.11}$$

G° = Gibbs free energy at standard condition (J/mol)

When equation (3.9) is combined with equation (3.11), it is revised as the next equation (3.12),

$$\Delta G = \Delta G^{\circ} + RT \ln\left(\frac{P_A^a P_B^b}{P_C^c P_D^d}\right) \tag{3.12}$$

ΔG° = Change in Gibbs free energy at standard condition

For fuel cell, hydrogen is used as a fuel and the reaction takes place,

$$H_2 + \frac{1}{2}O_2 \rightarrow H_2O \tag{3.13}$$

For the hydrogen oxidation reaction (equation 3.13) is applied to equation (3.12). In Table 3.1 is shown the variation of Gibbs energy with temperature;

$$\Delta G = \Delta G^{\circ} + RT \ln \frac{P_{H_2} P_{O_2}^{1/2}}{P_{H_2O}} \tag{3.14}$$

Table 3.1 Enthalpy and gibbs free energy of formation for oxygen, hydrogen and water at normal conditions [14]

Component	ΔHº (kJ/mol)	**ΔGº (kJ/mol)**
O_2(g)	0	0
H_2 (g)	0	0
H_2O(l)	-285,83	-237,13
H_2O(g)	-241,82	-228,57

º:means at 25°C and 101325 Pa , (g) : gas , (l) : liquid

For hydrogen fuel cell, two electrons pass through the external circuit for each water molecule produced and each molecule of hydrogen used (see equation 3.3). So for one mole of hydrogen used 2N electrons pass round the external circuit where N is Avogadro's number. If –e is charge on one electron then, charge that flows is

$$-2Ne = -2F \text{ (coulombs)} \tag{3.15}$$

F = the faraday constant, or charge on one mole of electrons and its value is 96485.

If E is the voltage of the fuel cell, then the electrical work is done in moving this charge round the circuit. This is given by the Nernst equation.

$$Electrical\,work\,done = charge \times Voltage = -2FE \ [Joules] \tag{3.16}$$

If the system is reversible (no losses) then the electrical work done will be equal to the Gibbs free energy released. So,

$$\Delta G = -2FE$$
$$E = \frac{-\Delta G}{2F} \tag{3.17}$$

This fundamental equation gives the reversible open circuit voltage of the hydrogen fuel cell. Using equation 3.11 into equation 3.17;

$$E = \frac{\Delta G^{\circ}}{2F} + \frac{RT}{2F} \ln\left(\frac{P_{H_2} P_{O_2}^{1/2}}{P_{H_2O}} \right) \tag{3.18}$$

$$\frac{\Delta G^{\circ}}{2F} = E^{\circ} \tag{3.19}$$

Open Circuit Voltage (OCV) is the voltage which can actually be measured at the terminals of an idling cell and is commonly used value for a cell under no load conditions. At the open circuit situation, a voltage difference can be seen between anode and cathode according to electrochemical potential of the oxide ions present at both electrodes. Its theoretical value is 1.23 volt. The fundamental equation gives the potential difference, known as the reversible cell voltage [15, 16].

$$E_{rev} = \frac{-\Delta G}{n \times F} \tag{3.20}$$

n: number of electrons exchanged per mole of product molecule

F: Faraday constant, the charge on one mole of electrons, 96485 coulombs

3.2 Electrochemical Efficiency of SOFC

Reversible reactions, which are explained in previous part, are theoretical knowledge. Practically, the fuel cell reactions are not reversible. The system has variety reasons to be an irreversible; the reasons are defined by efficiency factor. In addition, the most paramount efficiency factor for SOFC is electrochemical efficiency. The electrochemical efficiency is generated by three dominant efficiencies as revealed in Equation (3.21); the thermodynamic efficiency (η_{th}), the current efficiency (η_j), the voltage efficiency (η_{el}).

$$\eta = \eta_{th} * \eta_{el} * \eta_j \tag{3.21}$$

3.2.1 Thermodynamic Efficiency

The thermodynamic efficiency is referred to change in Gibbs free energy to convert sufficiently to electrical energy. Actually, the maximum value of efficiency is defined by intrinsic fuel properties. It shows the tendency of electrochemically oxidizing of fuel. In addition, thermodynamic efficiency is known as the maximum efficiency limit.

$$\eta_{th} = \Delta G/\Delta H = 1-(T\Delta S/\Delta H) \quad (3.22)$$

In this Equation (3.22),

ΔH = the difference of in the enthalpy of the reaction,

ΔS = the entropy change of the reaction,

ΔG = the change in the Gibbs free energy.

3.2.2 Current or Faraday Efficiency

The current efficiency is defined as the ratio of complete conversion of the cell to the current density. It has two main reasons, first; all the reactant do not converted to reaction products, and second one; some of the electrons are occurred from other reactions (for example corrosion reactions). The current density is shown in Equation (3.23)

$$\eta_j = i/i_f \quad (3.23)$$

i_f = incomplete conversion of the cell current density

3.2.3 Voltage Efficiency

The system has voltage losses due to polarization. The polarization is originated by three main issues; activation, ohmic and concentration. Additionally, the net cell voltage can be seen in the following equation.

$$V_{cell} = V_{open}-V_{act}-V_{ohm}-V_{conc} \quad (3.24)$$

Also, the efficiency of total voltage losses is explained by the equation (3.25) [13].

$$\eta = \eta_{act}+ \eta_{ohm}+ \eta_{conc} \quad (3.25)$$

Figure 3.2 illustrates a typical current voltage curves. As can be seen from the Figure, all the polarization characteristics are defined and recorded in detail during loading of the cell. The voltage curve is begun from the OCV and continued to a defined cell voltage during the measurement. The most important point is that; the temperature should have to be stay at stable conditions.

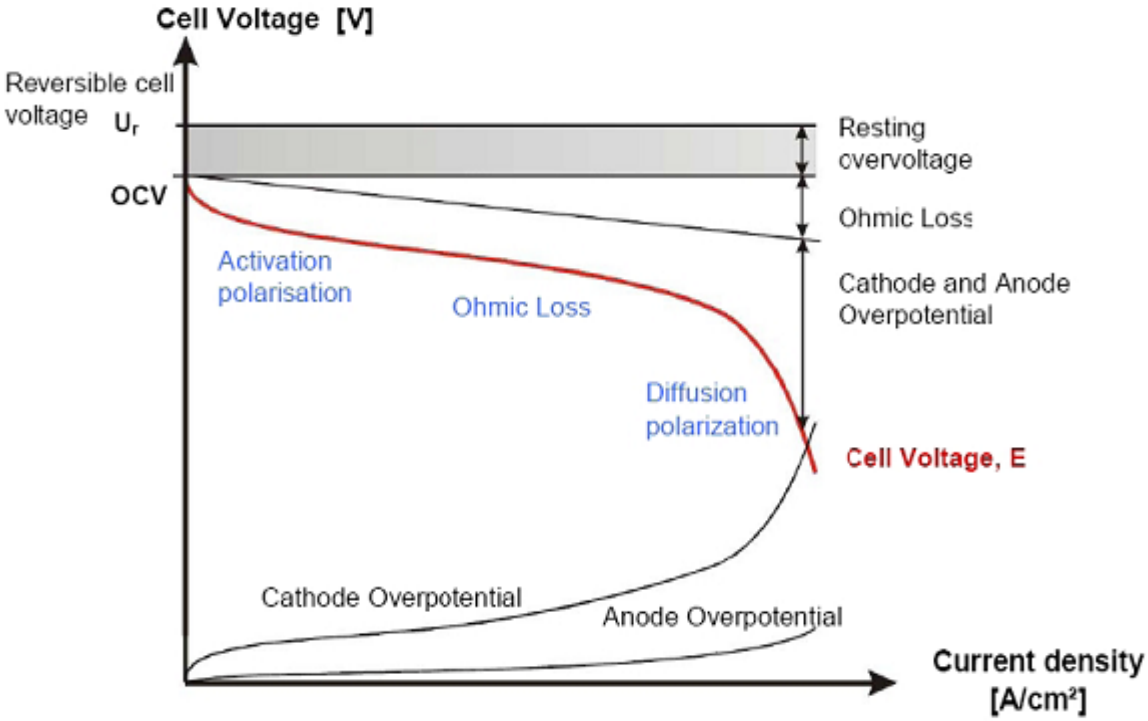

Figure 3.2 Current density versus to cell voltage [17]

Furthermore in the Figure 3.2, y-axis exhibited the cell voltage (V) and x-axis exhibited the current density (i/cm^2). Current density is the value, which can be obtained by dividing the measured current to the cell active area. Besides that, the reversible cell voltage value comes from the equation of Nernst and it could not be measured practically. On the other hand, the value of OCV is measured at the point of zero current. When the cell is loaded, firstly activation polarization is existed, just then ohmic polarization is occurred, and the last one is the diffusion polarization. After the voltage losses due to the kinds of polarization, the curve is reached to the net cell voltage.

3.2.3.1 Activation Polarization

The activation polarization is a voltage loss in regards to the reaction rates especially at the cathode side. These are caused by the slowness of the reactions taking place on the surface of the electrodes. A proportion of the generated voltage is lost in driving the chemical reaction that transfers the electrons through the electrode. When the reactants are arrived to electrode sides, the activation energy should be passed over limit value to achieve the reactions. Therefore, it is the reason of voltage drop due to the chemical reaction. Furthermore, it is the largest voltage losses during the operation. As well as, the activation polarization has a nonlinear behavior during the plot of the cell voltage and the current density, added it is dominant at low current. Activation polarization depends on some variables, can be seen on following function.

η_{act}= F{ material properties, microstructure, temperature, atmosphere, current density}

It is customary to express the voltage drop due to activation polarization by a semi-empirical equation, called the Tafel equation. The equation for activation polarization is shown below,

$$\eta_{act} = \frac{RT}{\alpha nF} \ln\left(\frac{i}{i_{\circ}}\right) \tag{3.26}$$

Where;

α = Charge transfer coefficient and its value depends on the reaction involved and electrode material. Its value is from 0 to 1. For hydrogen electrode its value is about 0.5 for a great variety of materials.

F = Faraday constant (96485)

i = Current density [mA/cm^2]

$i_{\circ}$ = Exchange current density. It can be considered as the current density where the over voltage begins to move from zero. It is obvious from the above equation that higher the value of $i_{\circ}$, lower is polarization (more active is the surface of electrode)

n = number of electrons involved in reaction

3.2.3.2 Ohmic Polarization

This voltage drop is the straightforward resistance to the flow of electrons through the material of the electrodes and the resistance to the flow of ions through the electrolyte. This voltage drop is essentially proportional to current density, linear, and so is called “ohmic” loss or sometimes resistive loss. Essentially, the dominant ohmic losses through the electrolyte are reduced by decreasing the electrolyte thickness and increasing the ionic conductivity of electrolyte. Ohmic losses can be expressed by Ohm’s law as [3],

$$\eta_{ohm} = [(\rho_e\lambda_e) + (\rho_c\lambda_c) + (\rho_a\lambda_a) + R_{contact}] \times i \quad (3.27)$$

ρ_e, ρ_c, ρ_a = resistivity (of electrolyte, cathode and anode)

$\lambda e, \lambda c, \lambda a$ = thickness (of electrolyte, cathode and anode)

i = current density (mA/cm^2)

3.2.3.3 Concentration Polarization

Concentration polarization is a voltage loss in regards to resistance of electrodes to transportations of mass and diffusion during the replacement of ions in the electrodes. The decreasing of concentration is caused to failure in sufficient transportations of reactants to the electrode surface. This change in concentration brings a drop in partial pressure of reactants. This pressure drop depends on the current which are coming from three phase boundary. Typically, the diffusion of polarization depends on some additional variables.

η_{conc}= F{binary diffusivity of reactants, microstructure, partial pressure, current density}

The reduction of partial pressure at the cathode side is caused a drop in voltage which is given in the equation (3.28). Additionally, hydrogen at the anode side has high diffusivity because of its low molecular weight; in that case the diffusion polarization at the anode side is lower than the diffusion polarization at the cathode side [17-18]

$$\eta_{conc} = RT/nF * \ln(P_2/P_1) \quad (3.28)$$

3.3 Electronic Impedance Spectroscopy

Electrochemical impedance spectroscopy is relatively new and powerful method of characterizing many of the electrically properties of materials and their interfaces with electronically conducting electrodes. The general approach is to apply an electrical stimulus (a known as voltage or current) to the electrodes and observe the response (the resulting current or voltage). The principle of impedance spectroscopy is based on applying a single-frequency voltage or current to the interface and measuring the phase shift and amplitude or real and imaginary parts, of resulting current at the frequency using either analogue circuit or fast Fourier transform analysis of responses [19].

Impedance is the opposition of a circuit to the flow of an alternating current (AC) at a given frequency. Mathematically, it is represented by a complex quantity. Impedance is an important parameter used to characterize electronic circuits, components and the material used in production of components. A fuel cell system can be considered as an electrical circuit with various components as it can be seen on the Figure 3.3. Therefore the electrochemical impedance spectroscopy is often used in explaining the changes in fuel cell performance, which can be observed at measured I-V curves. In this equivalent circuit a simple resistance symbolizes the electrolyte because its ionic conductivity is much higher than the ionic conductivity of the electrodes. On the contrary, a resistance and a capacitor are connected in parallel, symbolize each anode and cathode electrodes. Indeed there is gas diffusion through these two layers. That means it is controlled mass transport. This phenomenon can be explained by the modelling of the double layer. The other components like wires and platinum meshes are represented by an inductance connected in series. Thus the impedance of every component of the cell adds up to the measured overall impedance [12].

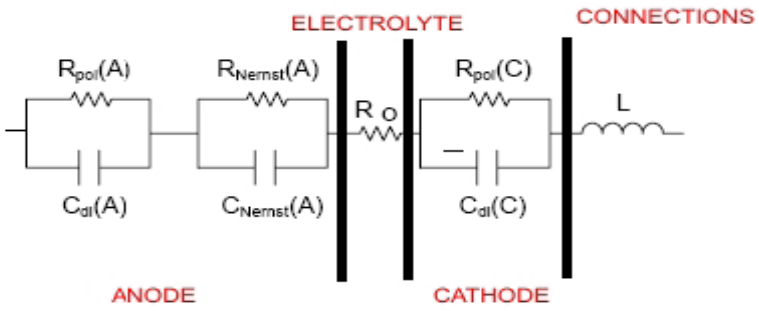

Figure 3.3 Electrical Circuit Model of SOFC [17]

3.4 Electrical and Ionic Conduction in SOFC

The important role of electrolyte in the fuel cell is to conduct ions between anode and cathode. Moreover, electrons are brought one side to another by the driving force of electrochemical reaction. Ions and electrons are trigged the electrochemical reactions. When voltage (V) is gone across a material, current of magnitude (I) is flown through the material. In most metals, the current is proportional to V, according to Ohm's law:

$$I=V/R \tag{3.29}$$

R = the electrical resistance ($J \cdot s/C^2$)

V = Electrical potential differences (Volt)

I = Current (ampere)

Electrical resistance (Eq 3.30) is a measurement of the degree which is opposed to the passage of an electric current. Electrical resistance depends on the intrinsic resistivity, ρ, also called specific electrical resistance of the material, measured in ohm · meter. Resistivity is a measure of the material's ability to oppose the flow of electric current [20].

$$R= \rho * l/A \tag{3.30}$$

L = The length of the conductor (m)

A = The cross sectional area(m^2)

ρ = Electrical resistivity

Moreover, the electrical conductivity is the inverse of the resistivity: $\sigma = 1/\rho$. The electrical conductivity is exhibited by both the electric field in the material (E) and current density (i) (divided by active area). Finally, the electrical conductivity function can be seen Equation (3.31)

$$i*E_{el} = \sigma \tag{3.31}$$

The conductivity is one of the properties of materials that is varied most widely from 10^{7} $(\Omega \cdot m)^{-1}$ (typical of metals) to 10^{-20} $(\Omega \cdot m)^{-1}$ for good electrical insulators. Semiconductors have conductivities in the range 10^{-6} to 10^{4} $(\Omega \cdot m)^{-1}$. Generally, the electrical conductivity is usually in the units of a Siemens per unit length, i.e. S/cm, where one Siemens is equivalent Ω^{-1} [21]

The operation of a SOFC is fundamentally predicated on electrical conduction in the ceramic component as electrode. Generally, electrical conduction in ceramics or crystalline solids depends on the material lattice defects. Some oxide ion conductors exhibit both electronic and ionic conductivity. Regarding to the oxygen partial pressure, the concentration of oxygen vacancies changes; therefore, the concentration of electrons and electron holes are affected in the lattice. The compounds, which have both ionic and electronic conductivity, are called Mixed Ionic Electronic Conductors (MIECs) in Figure 3.4. However, MIEC electrodes have advantages compared to pure electronically conductive electrodes owning to increase the effective Triple Phase Boundary (TPB) (where electrochemical reaction can take place). The Three phase boundary of electrochemical activity is affected only if electrons, oxygen vacancies or ions, and oxygen can transport to or away from the boundary.

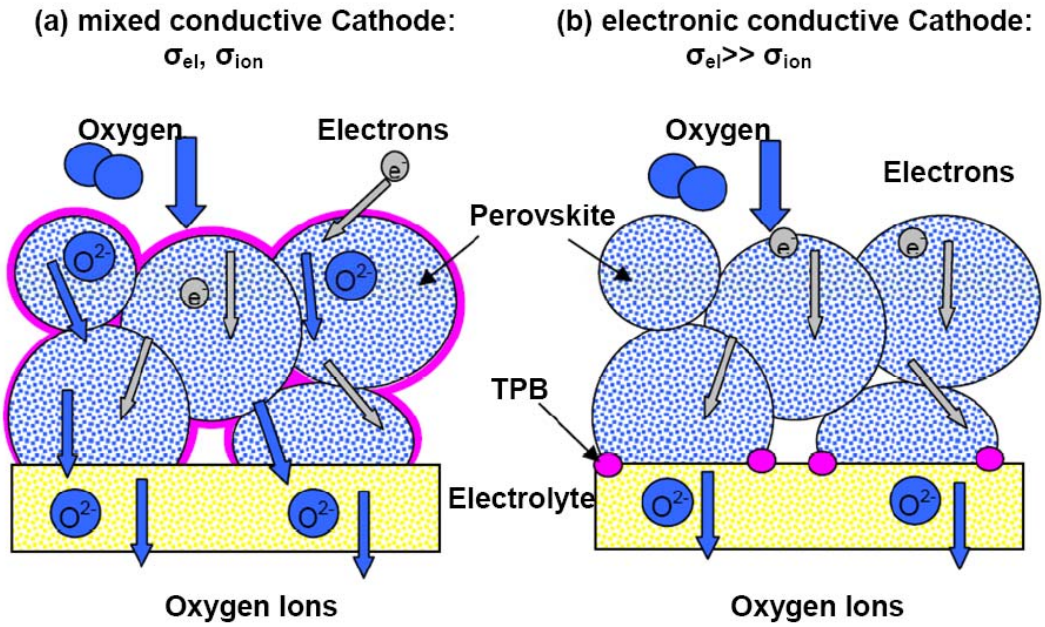

Figure 3.4 Oxygen transfer at the TPB with a mixed conductive and electronic Conductivity[22]

The ionic and electronic transfer numbers can be used to describe the respective contribution of ionic and electronic conductivity to the total conductivity σ, is written in the following Equation (3.32);

$$\sigma = \sigma_i + \sigma_e \tag{3.32}$$

σ = total conductivity

σ_i=ionic conductivity

σ_e =electronic conductivity

For electrolyte materials, an ionic transfer number is desirable close to unity. The ionic transfer number (ti), is explained by the following function (Eq 3.33);

$$t_i = \sigma_i / \sigma \tag{3.33}$$

The electronic transfer number in the electrode materials t_e, is explained by the following function (Eq3.34) [22];

$$t_e = \sigma_e / \sigma \tag{3.34}$$

The most important dependency of electronic conductivity depends on the temperature. Additionally, it is aided to determine the electrolyte performance. It can be seen in the Equation (3.35) which is called Arrhenius equation.

$$\emptyset_e = \frac{A_\emptyset}{T} exp\left(\frac{E_a}{kT}\right) \quad (3.35)$$

Where

Ea = activation energy for conduction, (Ea can be calculated from the slope of the ln(ØT) versus T^{-1} plots)

$A_\emptyset$ = the pre-exponential factor, (includes the carrier concentration as well as other material dependent parameters)

k = the Boltzmann constant

T = the temperature (K).

When comparing Ea values for different materials, the material with a higher Ea value exhibits a stronger temperature dependency of conductivity [12].

3.5 SOFC Component

In fabrication of SOFC different materials are used for each functional layer, but one common property of these materials is selected by their high temperature stability. The materials are consequently based on ceramics well known for their high temperature resistance. For example a cermet is used as anode material. It is a ceramic material based on Zirconia containing Ni-metal particles whose the properties are fundamental to assure all the function mentioned in the Table 3.2. As it can be seen, specific physical and electrical properties are required to allow good performance. In this Table, the different components are disposed exactly like in an SOFC. Indeed the substrate is the base of the cell, and then come successively the anode, the electrolyte and the cathode layers [18]. The properties of each layer will be detailed in the next part of this section.

Table 3.2 Typical Properties of the Layers of an SOFC [17]

Thickness (µm)	Physical Properties	Layer	Electrical Properties
40-50	High porosity TEC(1) Adherence to electrolyte	CATHODE	Electrical + Ionic conductivity Catalytic activity
40-50	Adherence to cathode Impermeability to gases Strengh TEC(1) Adherence to anode	ELECTROLYTE	Ionic conductivity
40-50	High porosity TEC(1) Adherence to substrate	ANODE	Electrical + Ionic conductivity Catalytic activity
700-1500	High mechanical strengh High porosity TEC(1)	SUBSTRATE	Electrical conductivity

(1) Thermal Expansion Coefficient

3.5.1 Cathode Side

The priority mission of the cathode is to provide reaction sites for the electrochemical reduction of the oxidant. The used cathode materials are explained in the following titles.

3.5.1.1 LSM

Generally, $La_{1-x}Sr_xMnO_3$ (LSM) (x between 0,15 and 0,5) is used as a cathode material. It has high electrical conductivity in oxidizing atmospheres, chemical and thermal expansion. These are compatible with YSZ electrolyte. As well as, chemical and physical stability are confronted with the environment effects during cell operation and fabrication. For transportation of molecular oxygen from the gas phase to the air electrode/electrolyte interface has to be sufficient porosity [23]. The principle of function is shown in Figure 3.5.

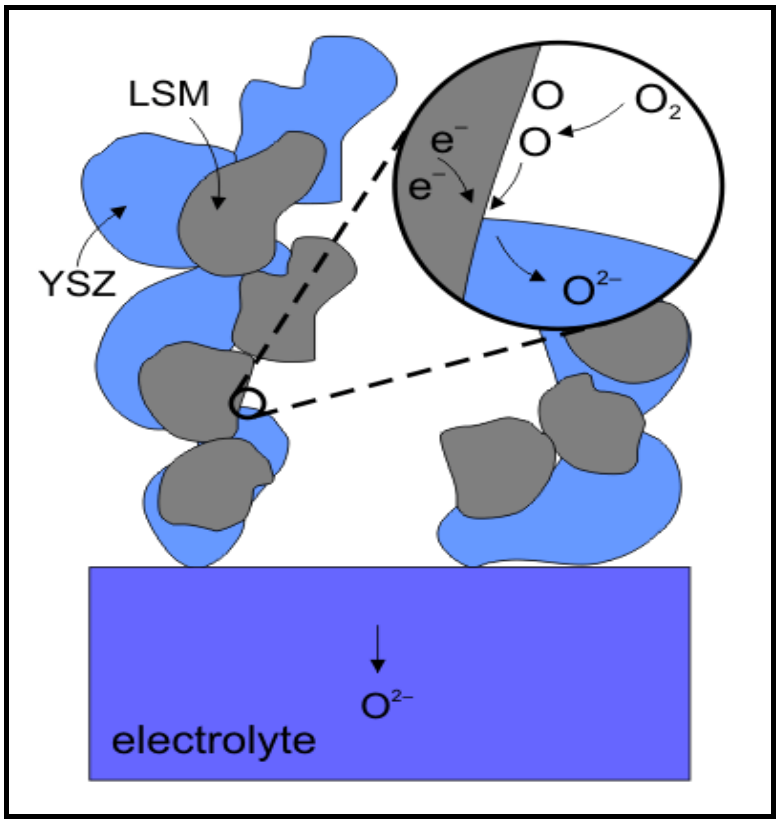

Figure 3.5 Schematic of an SOFC cathode [24]

Strontium doped lanthanum manganite ($LaSrMnO_3$, LSM) has a high catalytic activity for oxygen reduction, which is the main reaction occurred at the cathode side. LSM has a perovskyte structure and a p-type conductivity that means; the conduction in the material is accorded to the holes, formed on the Mn^{3+} site to maintain electron neutrality because of Sr^{2+} ion replacing La^{3+} ion. The ideal perovskyte structure is cubic. The LSM crystal lattice is shown on the Figure 3.6.

$$LaMnO_3 \rightarrow La_{1-x}{}^{3+}\ Sr_x{}^{2+}\ Mn_{1-x}{}^{3+}\ Mnx{}^{4+}\ O_3 \qquad (3.36)$$

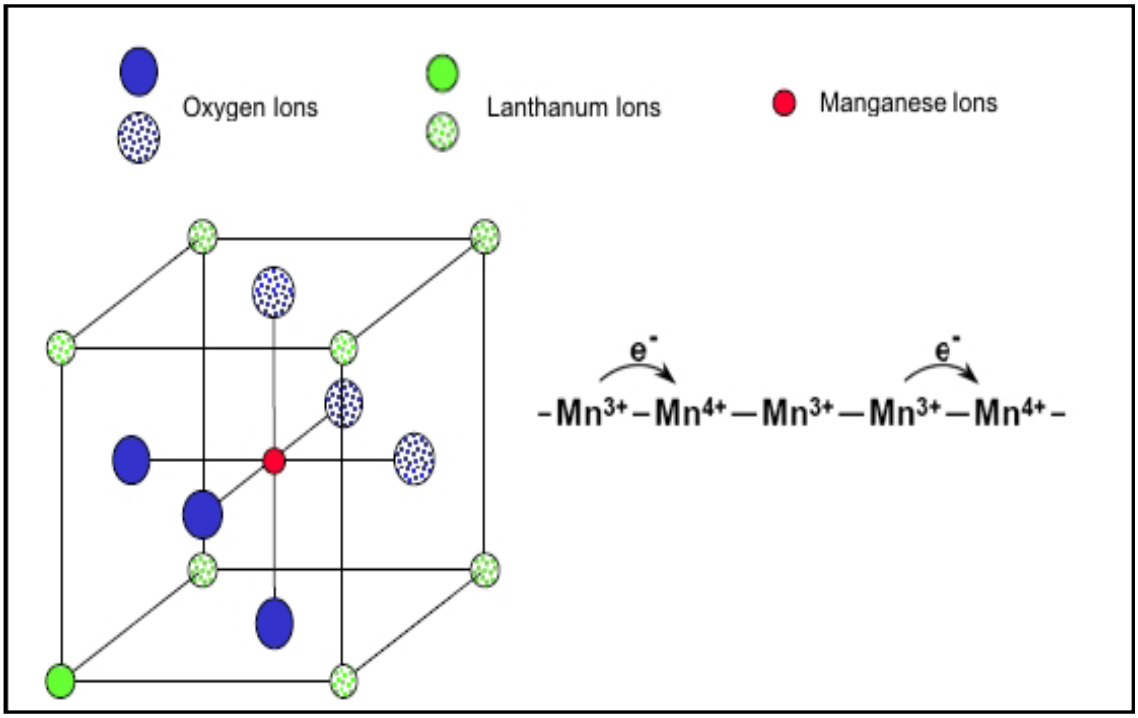

Figure 3.6 The LSM Crsytal Lattice [24]

Several problems might occur at high temperatures because of the surface layer. Indeed LSM and YSZ can react together and form $La_2Zr_2O_7$ at a temperature range above 1000°C. There is also an inter diffusion of manganese, strontium and lanthanum ions across the interface into the YSZ electrolyte. This change induces the creation of a novel layer which results in a higher overall resistance of the cell. The oxygen reduction takes place at the triple phase boundaries (TPB). Besides that, the polarization resistance decreases by applying a thin porous layer of Yttria-Stabilized-Zirconia (YSZ). The Thermal expansion coefficient (TEC) of LSM is in the same order of magnitude as the other SOFC components [1].

3.5.1.2 LSF

The un-doped $LaFeO_3$ has a low electronic and ionic conductivity due to few numbers of anion vacancies and as a result of the 3+, - valence is connected to nearly all the iron ions. The substitution of La^{3+} to the divalent Sr^{2+} -ions forms anion vacancies as well as a local change of the valence from Fe^{3+} to Fe^{4+} -ions takes place in order to ensure the charge neutrality in the perovskite [23]. The strontium subsequently enhances both the ionic and electronic conductivities.

doped with Strontium (Sr)

$$LaFeO_3 \longrightarrow \underset{A}{La_{1-x}}\ Sr_x\ Fe\ \underset{B}{O_3} \qquad (3.37)$$

As a result, an increase in the electronic and ionic conductivity is observed. The ionic conductivity of LSF increases directly with the inclination of the temperature while the electronic conductivity decreases. It is found in literature that for the composition $La_{0,8}Sr_{0,2}Fe0_3$ at 750 °C, the electronic and ionic conductivity is equivalent to 155 S/cm and 0,02 S/cm, respectively [25].

3.5.1.3 LSCF

Lanthanum cobalite, $LaCoO_3$ belongs to the same class of perovskite type structures as lanthanum manganite and shows both electronic and ionic conductivity. The critical oxygen partial pressure, below which decomposition occurs (Table 3.3), is higher (in a range of about 10^{-2} Pa at 1000 °C) when compared to lanthanum manganite. Furthermore, the partial substitution of strontium for lanthanum and iron for cobalt in $LaCoO_3$ affect the TEC and the conductivity of the material. Unlike LSM, LSCF exhibits rhombohedra phase symmetry. Their coefficient of thermal expansion is no longer matching with the electrolyte [26].

Table 3.3 TEM and electrical conductivity of LSM, LSCF, YSZ

Properties	**LSM**	**LSCF**	**YSZ**
Coefficient of thermal expansion [x10^4 cm/cm.K]	12,4	19,5	11
Electrical conductiviy [S. cm^{-1}] at 800^{O}C	30	335	2x10^{-2}

$LaCoO_3$ has no oxygen excess but shows a large oxygen deficiency at high temperatures, especially when doped with a lower-valance caution such as strontium. The $LaCoO_3$ is doped with strontium to increase the electrical conductivity, but the iron is added in order to have compatible thermal expansion coefficient with YSZ. The composite is doped with iron in order to allow the thermal expansion coefficient to be compatible with YSZ [23].

doped with Strontium (Sr) and Iron (Fe)

$$LaCoO_3 \longrightarrow La_{1-x}\,Sr_x\,Co_{1-y}\,Fe_y\,O_3 \qquad (3.38)$$

A B

DLR is now studying at this new kind of cathode material as well as Lanthanum Strontium Cobalt Iron Oxide is used for this master thesis.

3.5.2 Electrolyte Side

The priority mission of the electrolyte is to conduct ions between the anode and cathode. The electrolyte also provides to distinguish the fuel from the oxidant in the fuel cell. Therefore, the electrolyte material has to be impermeable to the reacting gases and sufficiently conductive (ionically) at the operating conditions. The electrolyte material is being studied Yttria Stabilized Zirconia which can be showed in the following Figure 3.7.

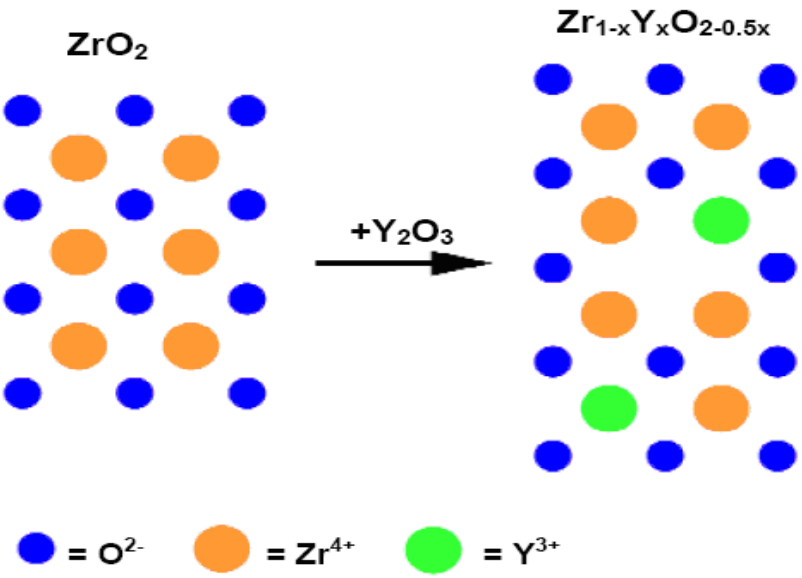

Figure 3.7 Example of a non-stochiometric defect [27]

For determining the material of electrolyte, key parameter is to have a sufficient high ionic and low electronic conductivity at the cell operation temperature. Related to the higher operating temperatures of SOFCs (from 600 °C to 1000 °C), the electrolyte has to be chemically and thermally stability with the other cell components from room temperature to the fabrication and especially operation temperature [26].

In details, the crystalline array of ZrO_2 has two oxide ions to every zirconium ion, however there are 1.5 oxide ions to every yttrium ion (in Y_2O_3). By this way, oxide ions are migrated by following the next vacancy in the crystal structure from the cathode side until they reach the anode side [28].

$$Y_2O_3 \xrightarrow{ZrO_2} 2Y_{Zr} + 3\,O^x_0 + V_0^{\bullet\bullet} \qquad (3.39)$$

Y_{Zr} = Y^{3+} -ion at the Zr^{4+} site, negatively charged

$V_0^{\bullet\bullet}$ = oxide ion vacancy at electrolyte lattice, positively charged

O^x_0 = oxide ion at the regular place in the oxide ion lattice

For example, an oxygen vacancy is created for every mole of the dopant Y_2O_3. The high oxygen vacancy concentration gives rise to high oxygen-ion mobility. Oxygen ion conduction takes place by the movement of oxygen ions by way of the vacancies. The ionic conductivity behaviour is influenced by such factors as: dopant material and concentration, temperature, atmosphere, grain boundary, and time. As the amount of dopants increase the conductivity of the resulting material [25]. The electrolyte crystal structure with and without dopping are shown on the Figure 3.8 and 3.9 respectively in order to evidence the changes in material to assure an electrical neutrality.

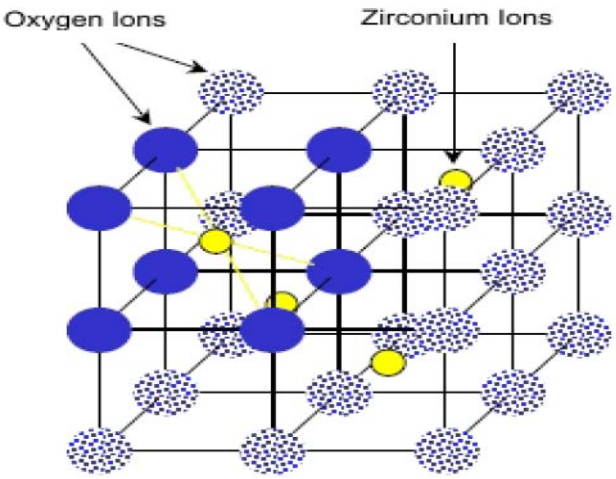

Figure 3.8 Crystal lattice of the zirconia[25]

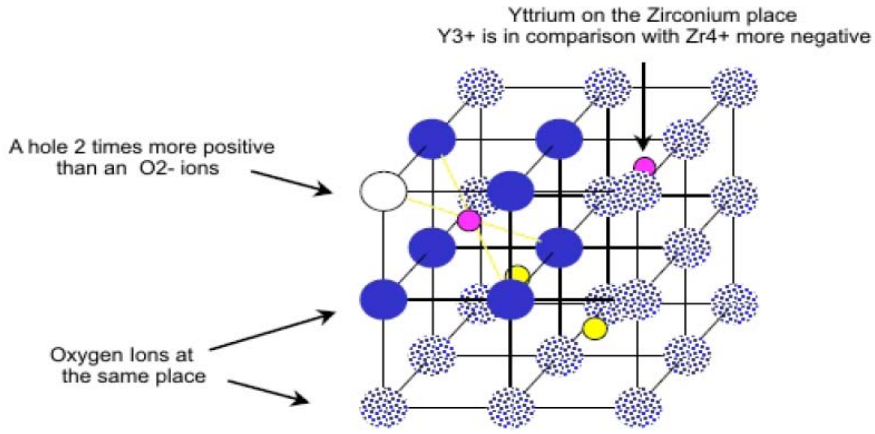

Figure 3.9 Crystal lattice of the yttria doped zirconia [25]

3.5.3 Anode Side

The priority mission of the electrolyte is to provide reaction sites for the electrochemical oxidation of the fuel and/or the reformation of hydrocarbons to hydrogen-rich fuels. Therefore, the key parameter of anode material is to be stable in the fuel reducing environmental and have sufficient electronic conductivity and catalytic activity for the fuel gas reaction at the operating conditions. In the following chapter, anode will be explained in details [12].

3.5.4 Substrate

The main degradation of an SOFC is due to high temperature corrosion of the used materials. Therefore, the operating temperature can be decreased for the improvement of the stability of the whole construction. On the other hand, the lower temperature increases the resistances of the functional layers which in turn to reduce the power output. This resistance can be easily reduced by changing the layer thickness. Therefore, a thin layer SOFC concept was developed by DLR, using the vacuum plasma spraying process (VPS) on a metallic substrate, as an alternative fabrication method, which will be explained in detail in the following chapter of this thesis. This new planar design is called metallic substrate-supported thin-film SOFC. This new design brings about a new problem of fragility of the cell due to its thin

structure. Therefore the most important criteria for the substrate is to have a high mechanical strength. It has to have high gas permeability as well, because hydrogen gas should be transported through this component in order to react with oxygen ions. A high electrical conductivity and an adapted thermal expansion behaviour relating to the ceramic layers are required. To possess all these qualities, the substrate is based on metals. Several types were experimented in DLR as it is shown on the Table 3.4, recently, a new ceramic alloy fabricated by Plansee (Austria) is exclusively used. It has been found to have a good high-temperature corrosion resistance while a good thermal conductivity combined with a high mechanical strength and a relatively lower thermal expansion coefficient. The metal cermet is based on a CrFe stainless steel metallic component mixed with an Yttrium oxide ceramic. It has high chromium content and impurities of silicon, aluminium, manganese[29]. In general, such alloys designed as porous structures offer an inadequate chemical stability in anode gas atmospheres. In contrast to the other substrates used, Plansee substrate is powder metallurgically (PM) manufactured. In PM process the material does not reach to the melting point, hence no significant evaporation or segregation process occurs. Thus the product has a more homogeneous elemental distribution in the alloy, thus more sufficient protective oxide layer forms during operation [30]. As a result the corrosion behaviour at high temperature is better than other substrates. With its 1-millimeter thickness and its 50% porosity, it has turned out to be an essential key component for the DLR SOFC concept.

Table 3.4 Different metallic substrates used for cell supported SOFC[17]

Substrate	Material	Thickness [mm]	Porosity [vol.-%]	Supplier/Partner
Fibre Felts	Ni and/or Fe-22Cr-5Al-0,1Y	~1,8	>85	Bekaert, Belgium/Technetics, USA
Woven Wire Structure	Crofer22APU	~1	~60	Rhodius, Germany/ Haver&Boecker, Germany
Knitted Wire Strucure	Crofer22APU	~1	~35	Rhodius, Germany
Sintered Porous Metal Plate	FE-26Cr-(Mo,Ti,Mn, Y_20_3,TM 14)	~1	~50	Plansee,Austria

3.5.5 Interconnect

Interconnection serves as the electric contact to the air electrode and also protects the air electrode material from the reducing environment of the fuel on the fuel electrode side. The requirements of the interconnection are most severe of all cell components and include the following:

• High electronic conductivity

• Chemical stability in both oxidising and reducing atmospheres at the cell operating temperature

• Low permeability for oxygen and hydrogen to minimise direct combination of oxidant and fuel during cell operation

• An adapted thermal expansion coefficient with other cell components

• Non-reactivity with the air electrode and the electric contact material (e.g. nickel).

To satisfy these requirements, doped lanthanum chromites have been extensively investigated to use them as the interconnection material. The reduction of the cell operating temperature to 800°C in case of DLR's SOFC concept makes the use of metallic materials for the interconnect feasible. Metallic interconnectors fulfill the above required properties.

3.5.6 Diffusion Barrier Layer

A diffusion barrier layer is ought to be developed by vacuum plasma spray process at substrate/anode interface to inhibit the "Substrate/Anode" material transport. Because of high process temperature of about 800°C, atomic transport processes emerge which can cause the destructive changes in the structure during long cell operation in the SOFC. In particular, the "Substrate/Anode" interface represents a problem area. For example, exchange processes of Fe-, Cr- and Ni- species between the anode and the metallic substrate material take place during the cell operation that can induce significant structure changes in both the anode and in the substrate. Schematic Transport of these species is shown in Figure 3.10.

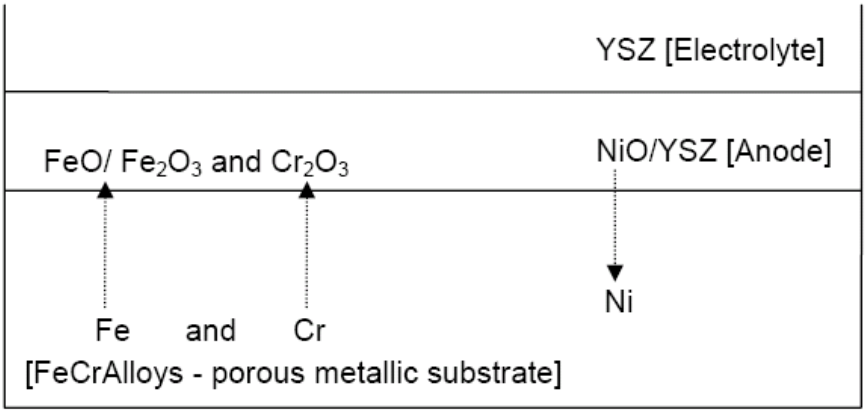

Figure 3.10 Simple schematic showing exchange processes of Fe, Cr and Ni between substrate and anode of a SOFC ate and anode of a SOFC

This barrier layer should be possibly thin, porous and high electrical conductive representing the SOFC anode side electrochemical relevant conditions. Other requirements include an adopted thermal expansion coefficient with other components of the cell, chemical stability in reducing and humid anode gas atmosphere and electrochemical compatibility. Because lanthanum chromites exhibit the above mentioned properties, these are possible interesting candidates to serve as "diffusion barrier layer" particularly when doped with alkali metals (e.g. Sr. Ca. etc.). Lanthanum chromite is a p-type conductor. Conductivity in $LaCrO_3$ is due to small polar on hopping from room temperature to 1400°C at oxygen pressures as low as 10-18 atm. The conductivity is enhanced as lower valence ions (e.g., Ca, Mg, Sr,

etc), are substituted on either the La^{3+} or the Cr^{3+} sites. Doped $LaCrO_3$ exhibit adapted TEC with other cell components and are chemical compatible [31].

3.6 Thermal Plasma Spray Method

Several processes have been applied to fabricate SOFC layers such as, tape casting, screen-printing and dip molding and thermal plasma spray. These coating techniques require high temperature sintering process except thermal plasma spray. For large area cells, this step will inevitably introduce a lot of defects, such as warp, crackle and pore. At the same time, in order to assure, dense electrolyte, porous electrode and good electrochemical inter lamellar contact, the sintering step would procedurally be complex. This time consuming and sintering process is a shortage for mass production, and therefore it is difficult to meet the strict cost targets for the successful introduction of SOFCs in the strongly competitive energy market. In comparison to the above mentioned processes plasma spraying has appeared as one of the promising candidates. Plasma spraying is a fast single step, low cost process, especially concerning the mass production of SOFC. The main advantage of porous metallic supported thin-coating cell, fabricated by plasma spraying, is to allow enlarging the cell area without sintering defects and improve its mechanical properties. In addition plasma spraying controls the deposit composition and microstructure through variation of spray parameters [32]. Based upon the processing conditions plasma spraying can be classified into two general classes' i.e. atmospheric plasma spraying (APS) and controlled atmosphere plasma spraying (CAPS). The plasma generation principle is identical for both types of spraying. The only difference being that APS is carried out at atmospheric pressure in the presence of air while in CAPS the atmosphere is controlled as per requirement. At DLR Stuttgart plasma spraying is done at low pressure in the presence of argon called low pressure plasma spraying (LPPS). LPPS is sometimes referred to as vacuum plasma spraying (VPS), therefore in the coming discussion LPPS will be named VPS. The layers deposited through VPS are denser than the one deposited by APS. But through variation of parameters it is also possible to deposit porous layers by VPS. As mentioned earlier for SOFC, denser electrolyte and porous cathode/anode are required.

In the new thin-film SOFC concept of DLR in Stuttgart, the entire membrane electrode assembly (MEA) is deposited onto a porous metallic substrate by an integrated multi-step Vacuum Plasma Spray (VPS) process. This concept provides the production of an electrolyte layer of thickness of only less than 50 µm resulting in a significantly reduced overall thickness of the cell to 100 µm to 120 µm. Additionally, VPS enables the reduction of the cell temperature from 800 °C to 700°C without a significant decrease in power density due to reduction of the ohmic cell losses. Cells with a high mechanical stability and large active areas are able to be fabricated due to the substrate support. Its characteristic properties such as short process time, high material deposition rate and the ability to be transferred to an automated production line promise a fast and cost effective fabrication of cells with large active cell areas [33].

3.6.1 Plasma

Plasma is a conglomeration of positively and negatively charged particles. It is on the average neutral, because the number density of the positive charges is equal to that of negative ones. The plasma may also contain neutral particles or may be fully ionized (when all the particles are charged). The plasma will then contain two or more kinds of charge carriers: free electrons and positive ions. Sometimes it has also negative ions and more than one kind of positive ion. The ions may be singly charged or multiply charged; they may also be atomic or molecular.

An important parameter is the degree of ionization, which is the percentage of those gaseous atoms or molecules initially present that has been decomposed into charge carriers. When the plasma contains neutral particles, the degree of ionization is less than one. It is closer to unity when the plasma is strongly ionized and closer to zero when it is weakly ionized. Sometimes, multiply ionized atoms account conventionally for a degree of ionization greater than one. The word plasma itself was introduced by Langmuir before any interest began to be devoted to fully ionized gases, and cannot be restricted to fully ionized gases.

The fully ionized plasma is sometimes considered as a particular state of matter. Indeed, Matter can be found in four different states: solid, liquid, gas or plasma. It is well known that when enough energy is added to a solid, the solid will change its state and become a liquid which in turn with enough energy added to it will become

a gas. The molecules of such a gas will assume a variety of degrees of freedom. If one keeps adding energy, the kinetic energy of the particles will increase and molecular impacts will become so intense so that dissociation will result between some of the electrons and rest of each molecule. The gas will become plasma. The energy added is partly converted into random kinetic energy and partly into dissociation energy. The physical properties are different from one state of matter to the other.

3.6.2 Plasma Sprayed Equipment

Having defined the plasma, the next question is how to utilize it for required applications. For this purpose plasma spray equipment is used. A plasma spray equipment Figure 3.11 mainly consists of, Plasma gun/torch mounted on a robot, substrate holder, powder feeders, vacuum pumps (for vacuum plasma spraying), filters and exhaust system, gas feed pumps, cooling water supply unit, computer interface control panel and a sealed chamber/vessel enclosing the plasma torch and substrate holder. The environment inside the chamber may be controlled as required i.e. vacuum or atmospheric. The powder feeder and pumps are not the part of the chamber, but situated outside. The substrate holder is provided with heating elements in order to heat the substrate when required [34]. The major component of the equipment is plasma torch explained next.

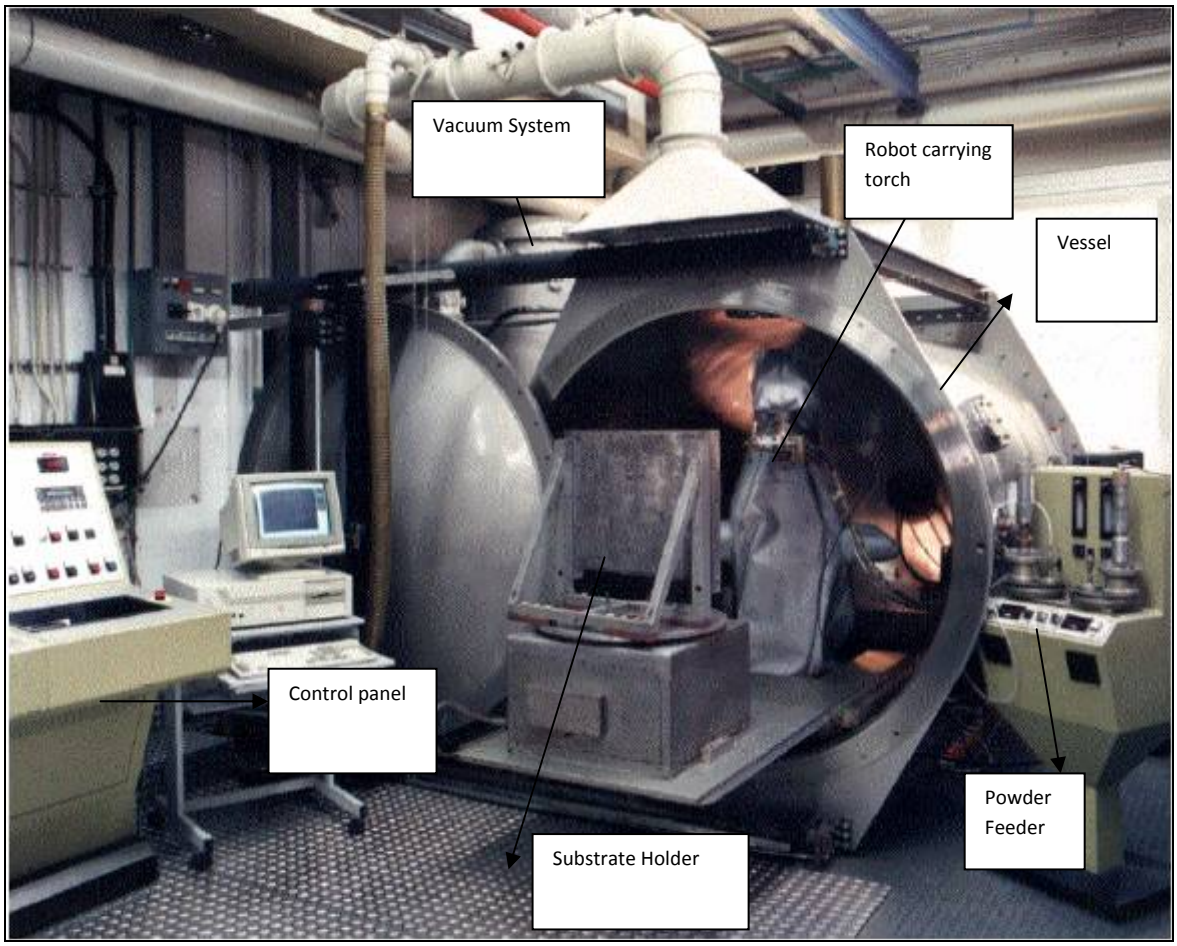

Figure 3.11 Plasma spray equipment

Plasma Equipment: Plasma Technik AG Switzerland

Robot: ABB Germany

Nozzle: Mach 3

Powder Feeder: Sulzer Metco Twin feeder (10-C)

3.6.3 The Plasma Torch

Vacuum plasma spray can be used as a deposition technology for powders and substrates, which are sensitive to oxidation or if very dense coatings are required. VPS technique is applied in a low pressure environment of an evacuated chamber which is floated with purge gases. The plasma spray process is based on the generation of a plasma jet consisting of argon with a mixtures of H_2 and He which are ionized by a high current arc discharge in a plasma torch. Novel plasma torches spray the particles at a velocity from 800 m/s to 900 m/s [35]. Figure 3.12 shows schematic principle of the DLR plasma torch with a laval-like nozzle contour. The

powders used can be injected at different ports along the nozzle of the plasma torches depending on melting properties. Spray parameters and conditions for electrolyte and porous electrodes with desired properties have already been developed separately at DLR. The metallic powder particles are fed into a high temperature plasma jet escaping from the supersonic nozzle of the plasma torch. Powders to be sprayed are injected into the plasma where they are accelerated, melted and finally projected onto a substrate. The solidification and flattening of the particles at impact on the substrate form the coating and layers. A long and laminar plasma jet with high velocity and reduced interaction with the surrounding cold gas is formed resulting in improved spray conditions by carrying out the whole spray process in vacuum chamber. The plasma torch is moved by means of robot system to ensure uniform and reproducible deposition of the layers [36].

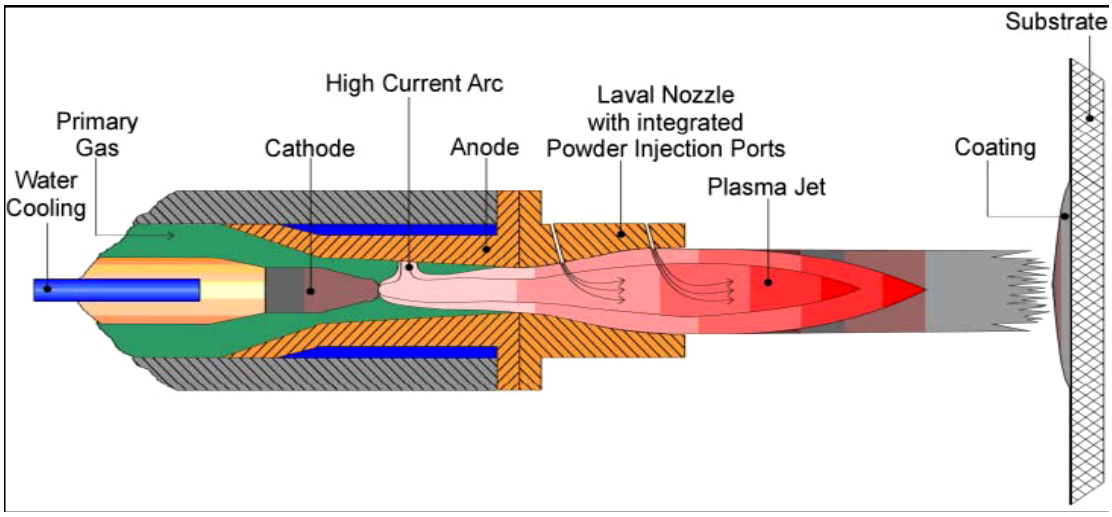

Figure 3.12. Cross-section of VPS gun with substrate (DLR, Stuttgart) [17]

In plasma spraying equipment, this process is carried out by using a plasma generator or torch shown in Figure 3.13 and Figure 3.14. The plasma torch, consists of the following major parts[11];

- Cylindrical anode as front nozzle
- Cone shaped cathode
- Water cooling system for anode and cathode
- Powder injection ports in nozzle shaped anode

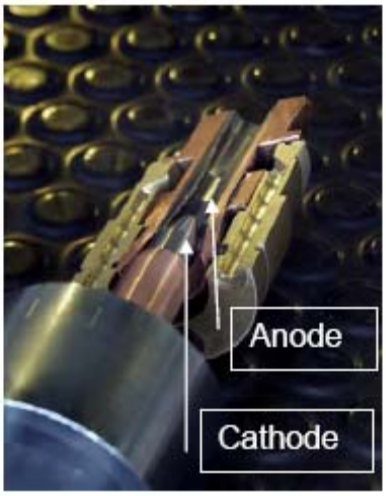

Figure 3.13 Plasma Torch [11]

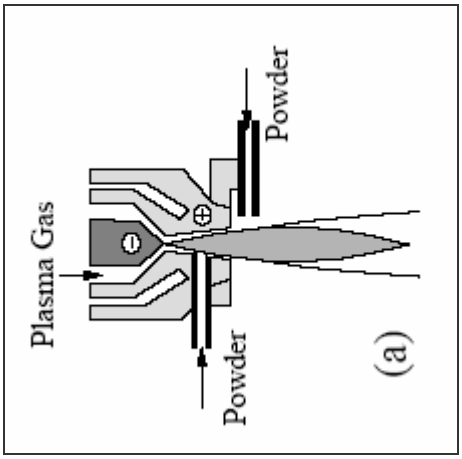

Figure 3.14 Powder Feeding Process [11]

3.6.4 Plasma Torch Operating Principle

The torch operating principle is as follows: A gas flows through the conical gap between the electrodes and is ignited by a voltage of 50 V, with several hundreds of amperes discharge, which causes ionization and a conductive path for a DC arc to form between anode and cathode. The resistance heating from the arc causes the gas to reach extreme temperatures. This high temperature causes the gases to dissociate and ionize to form plasma. The electrons and the positive ions from the ionized gases are accelerated towards anode and cathode respectively, collide with the neutral

atoms or molecules in the gas and ionize them. Through these interactions, the gas within the arc transforms to the collection of ions and energetic electrons, called plasma. In the plasma, the negative and positive charges have to balance each other. This property is known as quasi-neutrality. The energy content of plasma is highest in the core and gets lower towards the edges. Plasma flames can produce temperatures from 7000 K to 20,000 K and can reach supersonic speeds, depending mainly on nozzle geometry, gas flow rate and pressure of the surrounding i.e. the pressure of the chamber enclosing plasma torch and substrate. When used for materials processing and thermal spraying applications, powders ($5\langle d_p \langle 100\ \mu m$) are injected into the plasma jet either internally into the anode nozzle, or externally at the exit of the nozzle. Typical material residence time in the plasma is less than 1 milli second. The electrical energy used for particle heating is approximately 3% of the total supplied.

The choice of the gases for plasma spraying is dictated mostly by the ability to melt the sprayed particles. This ability is higher for molecular gases due to greater thermal conductivity, than for atomic gases. On the other hand, monatomic gases jets, reach higher jet velocities. That is why; the mixtures of monatomic gas with a molecular one have been often used in order to assure melting of the particles as well as their high velocity while spraying. Typically Ar mixed with H_2, He, or N_2. The monatomic He is used as an additive to Ar due to not only the high thermal conductivity, but also the formation of a narrow spray cone [11].

3.6.5 Particle Solidification and Layer Formation

Particles injected into plasma jet are heated to high temperature and gain high speed. The high particle temperature and speed result in significant droplet deformation. The molten particles form a pancake or flower shaped lamellae. Solidified droplets build up rapidly, particle by particle, as a continuous stream of droplets impact to form continuous layers. Upon solidification the long axis of the lamellae are oriented parallel to the substrate surface. Each droplet cools at very high rates ($> 10^6$ K/s).

Figure 3.15 shows a schematic of a generic thermal spray powder consolidation process, illustrating the key features and a typical deposit microstructure. From Figure it is obvious that a plasma sprayed coating presents a lamellar structure. The study into the lamellar interface bonding revealed that the lamellae contact the

substrate (or previously deposited coating) only on a part of the bottom surface because partially melted or un-melted particles do not adapt well to the previously deposited coating. In fact, at contact with such lamellae pores having sizes of a few micrometers are generated. The areas of contact are sometimes called welding points or active zones, and correspond to 20 to 30 % of total area of the lamella. The adhesion of the coating improves if all the particles are properly melted and if the contact areas of the lamellae become greater. These areas are adjacent to oxides (if sprayed metal or alloy oxidizes in flight); air filled pores (due to the irregularities on the substrate surface) and working gas-filled pores (evacuated during particle solidification). Because of this limited bonding of lamellar structures the properties of the deposited material are different from the bulk material. So the microstructure of the coatings determines their properties. Therefore while optimizing the processing parameters, one should bear in mind, what property the coating is expected to achieve and how the coating microstructure is related to this property[37].

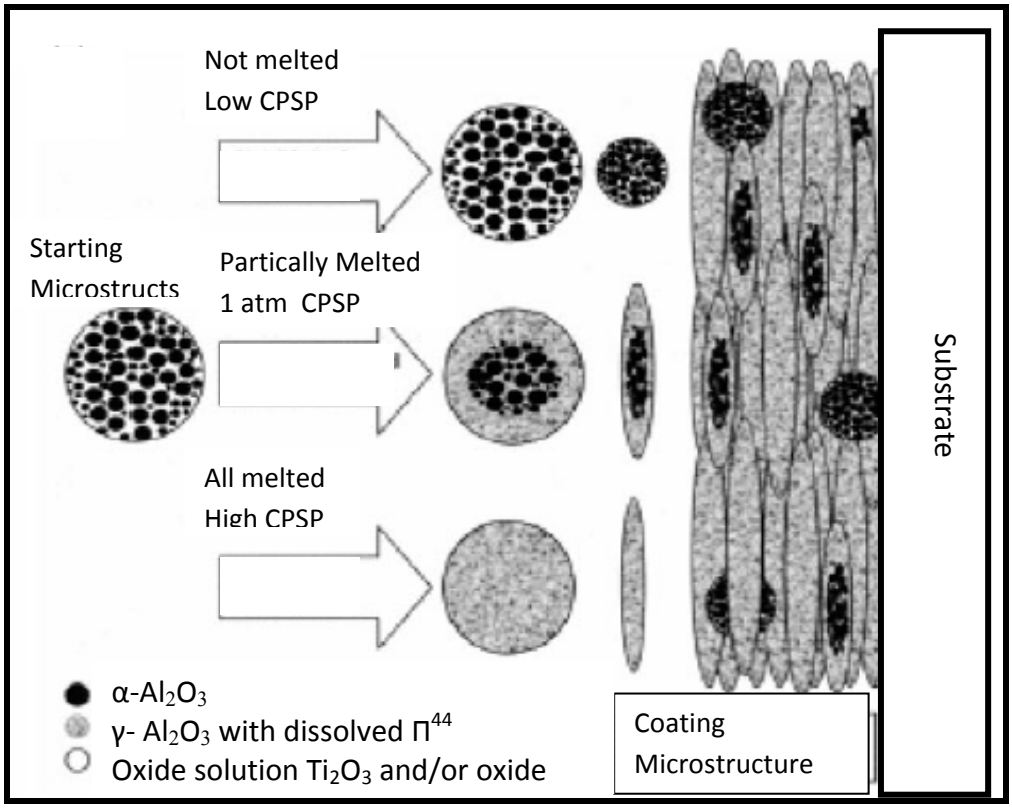

Figure 3.15 Layer deposition [37]

4. THE ANODE OF SOFC

The main function of anode in the SOFC is to provide the sites for the fuel gas to react with the oxide ions which are delivered from cathode by electrolyte. As well as, the anode material structure should have sufficient charge neutralization by its electronic conductivity. Chemical and physical stability is necessary for a wide range of variations such as temperature, from fabrication to operating condition, or redox cycles. The electrochemical reaction takes place at the boundary surface of anode with electrolyte where oxygen ions can be reached from electrolyte. The hydrogen can be accessible through the porous anode as well as, the output of electron can be conveyed through the porous anode to the external circuit. In other words, the boundary of anode and electrolyte and the gas phase is called three phase boundary (TPB). Additionally, ionic conductivity permits the oxygen ions across the three phase boundary [1]. Actually, the anode material should have not only high electronic conductivity, but also electro catalytic active area which could be established for a rapid charge exchange. The mechanistic details of the simple hydrogen oxidation are still not clear; however the reaction can be formulated as [32].

$$H_{2(gas)} + O^{-2}{}_{(YSZ)} \longrightarrow H_2O_{(gas)} + 2e^-_{(Ni)} \qquad (4.1)$$

As a result of all these parameters for the anode, ceramic and a few metallic materials can be used efficiently, while many candidate anode materials are tested in the earliest of twenty century. Obviously, only metallic or only ceramic materials could not fulfil the all required properties of anode. As an alternative the composition of metallic and ceramic, is called cermet, could be used as a material of anode. Between the variety candidates, nickel is the most suitable metallic element for the anode. However, nickel aggregates at high operation temperature inhibiting access of the fuel. Spatil is the first scientist, who recognized the nickel aggregation problem. He had solved this problem by mixing the yttria-stabilized zirconia with nickeloxide.

Furthermore, for the reducing environmental at the anode side only limited number of metals structure is appropriate, besides that; nickel has low cost when compared with the other catalytic metals such as platinum, and palladium [39]. Although Nickel combination with YSZ is the most reliable and successful model, nickel has some incapable properties, as an anode material. Nickel has high thermal expansion coefficient considerably larger than YSZ which is the electrolyte component. Meanwhile, nickel can also caused to decrease the size of the anode porosity because of sintering at high operation conditions. The YSZ molecules are served as a skeleton around the nickel particles; whereby, sintering of the nickel particles is avoided by the YSZ skeleton. Additionally, not only the fuel electrode thermal expansion coefficient is controlled by YZS, but also YSZ is bringing much closer structure with the electrolyte. As well as, YSZ molecules in the anode provide better adhesion to the electrolyte [28].

4.1 The Formation of the Anode Functional Layers

The layers of anode can be produced to the required specification by VPS process. The controlled porous anode layers can be obtained by the appropriate selection of composition, morphology and the grain size fraction of the spray powders and by the adjusting the spraying parameters. Since the particles are impinged at high speed with a fast kinetic energy, the particles form flat lamellae and solidify Figure 4.1. The large and incomplete melted pieces will either incorporate to the lamellae layer where the layer is inhomogeneous or repel due to the fast kinetic energy. The small particles evaporate in the plasma jet [40].

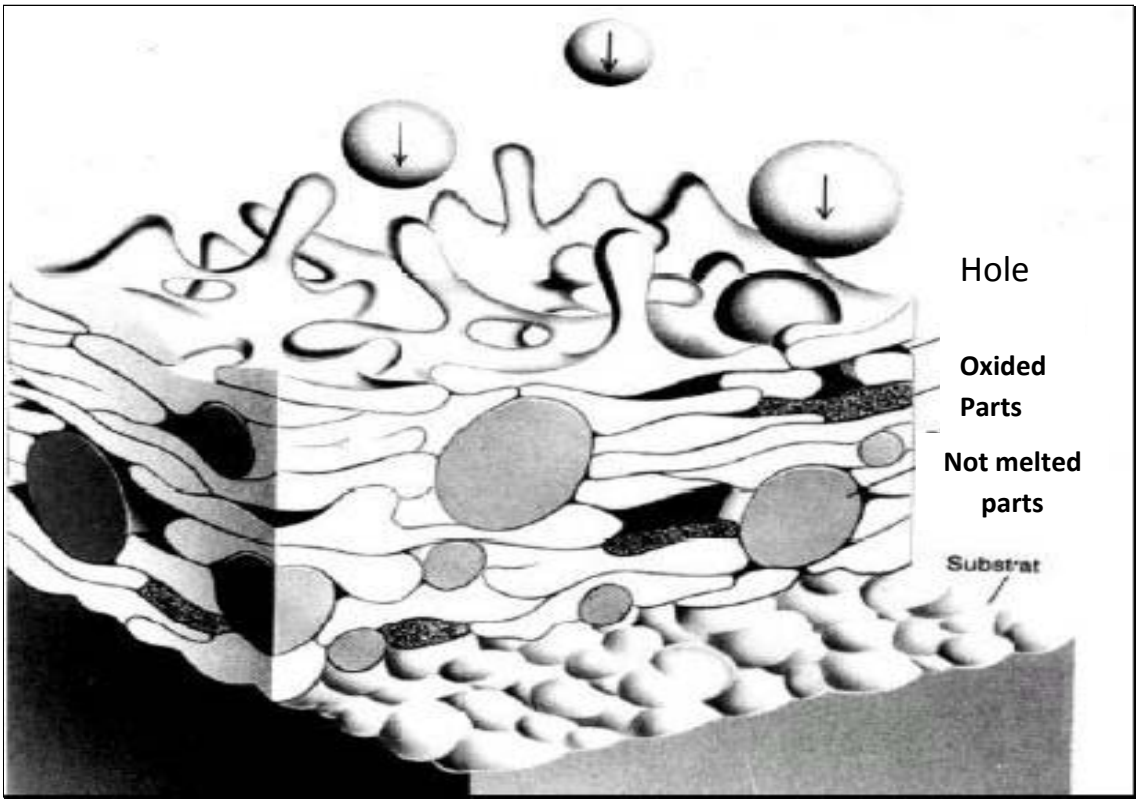

Figure 4.1. Illustration of the VPS sprayed structure from the middle [40]

4.2 Electrical Conductivity of Anode

In the composition of Nickel/YSZ, nickel provides the electrical conductivity of the anode. Minimum metal proportion in the cermet is necessary for continuity of electronic conduction, while the zirconium particles can be non-continuity. The conductivity of the cermet can be predicted by the percolation theory. This theory applies to the electrical conductivity of composites. The percolation threshold for the conductivity is about 30 vol.-% nickel. Below this threshold, the cermet exhibits predominately ionic conducting behaviour. Above 30 vol.% nickel, the conductivity is about three-orders of magnitude higher, corresponding to a change in mechanism to electronic conduction through the nickel phase. In Figure 4.2, the Ni content in vol.-% is shown on the x-axis and the electrical conductivity in S/cm is on the y-axis. This diagram illustrates the percolation theory, at 30 vol.-percent with varying temperature, the electrical conductivity dramatically increases [41].

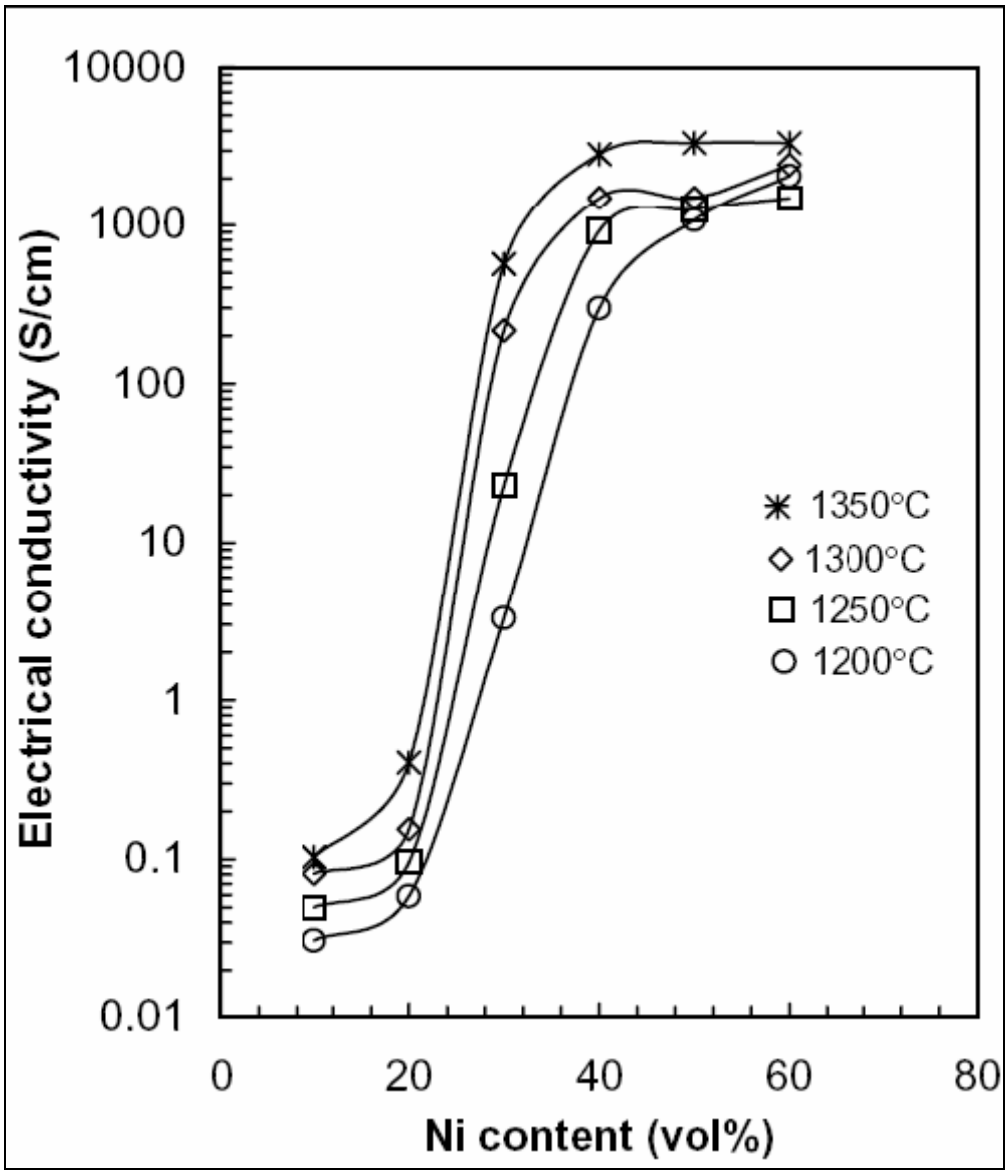

Figure 4.2 Nickel content to electrical Conductivity [42]

Furthermore, above this threshold, the conductivity is also dependent on its microstructure (YSZ microstructure). In general, hydrogen reduction of NiO in the anode is fast at high temperatures. Although most of the reduction occurs in the beginning, it may take longer for the conductivity to reach a steady state due to continuing reduction and rearrangement of nickel particles as the reduction proceeds. During the reduction, the conductivity of the anode usually reaches a maximum very quickly, and then falls off slowly until a steady state is achieved. The maximum occurs when enough NiO is reduced to form a conducting nickel-metal matrix, and the fall-off corresponds to loss of nickel particle contact as the particles shrink due to

further NiO reduction. Therefore, this conductivity fall-off varies depending on the nickel content and grain size in the anode [23].

At DLR, the VPS anodes amount possesses a high electrochemical activity and has excellent conductivity at high temperatures (σ_{el} = 2·104 S/m at 800 °C). Furthermore, the manufacturing of the anode is generally a powder mixture composed of YSZ and Ni-Oxide is applied, whereby the mixture is applied on the substrate with the VPS method. After the reduction of NiO, the volume percent adds up to 50 vol.-% YSZ, 30 vol.-% Ni, and 20 vol.-% Pores in the structure [43].

4.3 Anode Three Phase Boundary and Catalytic Activity

The catalytic activity property of anode is the most important parameter in SOFC system while determining the overall fuel cell efficiency. The electrochemical reactions are occurred at the three phase boundary. In the composition of Ni-YSZ, Nickel has two major roles, catalyst for hydrogen oxidation and electrical current conductor. Besides, the beneficial property of YSZ provides ionic conductivity for the electrochemical reactions [44].

4.3.1 Anode Three Phase Boundary

Three phase boundary is critical subject to optimize the anode performance. The electrochemical reactions can only occur at the three phase boundary, which is defined the collection of sites where the electrolyte, the electron conducting metal phase, and the gas phase all come together. When one of the three phase element is broken down than the electrochemical reaction can not occur at this region. For example, the oxygen ions could not reach the reaction site or gas phase molecules could not reach the site. And if electrons could not transfer from the reaction site to the external connection, the electrical cycle could not be completed.

Actually, the diffusion of ions through the electrolyte partially limits the electrochemical reaction. However, the concentration of the excess ions, which are come into the anode, can be ignored. For the electrochemical oxidation in the TPB, the largest surface area provides the better ionic connectivity between the electrolyte and the active site. Significant electric-field gradients can only occur near the TPB. Far from the TPB, the oxide phase will be completely inert, other than providing

structural support of the anode. The metal phase in the anode far from the TPB provides electronic conductivity [45].

4.3.2 Catalytic Activity

The charge transfer reactions are occurred between surface and adsorbed species, taking place as a line reaction at the TPB. There are two path ways for the charge transfer reaction. First, the oxygen ions spillover from the YSZ to the nickel surface (a); and the second, which is the dominant way, hydrogen spillover from the Ni to the YSZ surface (b), shown in the Figure 4.3.

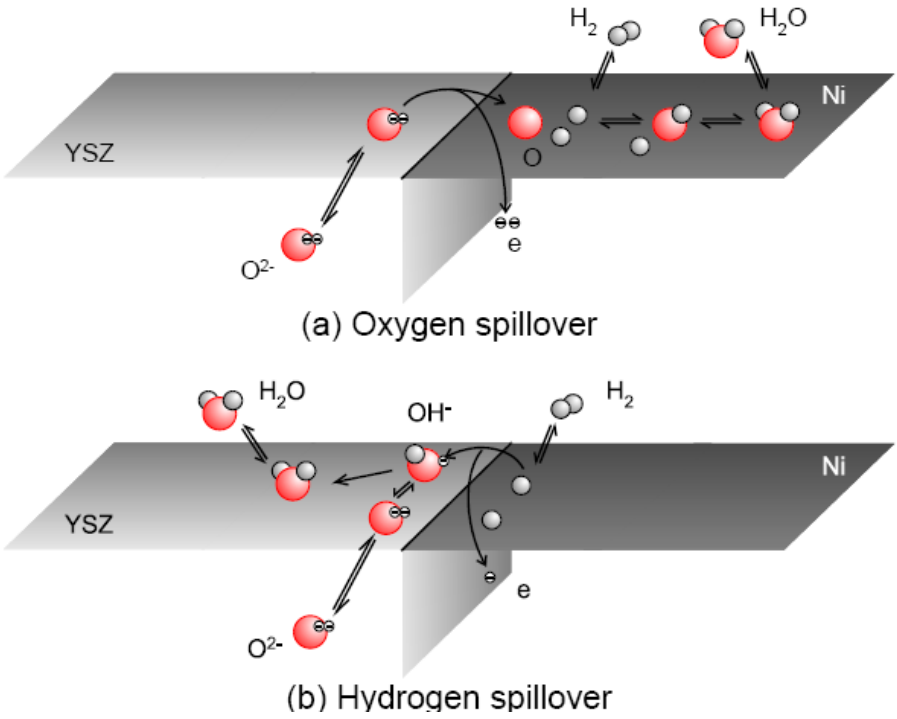

Figure 4.3 The charge transfer reactions [42]

For the charge-transfer step, the forward and reverse reaction rate constants *k*f and *k*r follow from transition state theory and are given in next equations.

$$k_f = k_f^0 \exp\left(\frac{-E_f^{act}}{RT}\right)\exp\left(\alpha\frac{zF}{RT}\Delta\Phi\right) \tag{4.2}$$

$$k_r = k_r^0 \exp\left(\frac{-E_r^{act}}{RT}\right)\exp\left((1-\alpha)\frac{zF}{RT}\Delta\Phi\right) \tag{4.3}$$

Where,

$k^0_{f,r}$ = the preexponential factors [mol/(m s)],

E_r^{act} = the thermal activation energies [J/mol],

α = the symmetry factor,

$\Delta\Phi$ = the electrical potential difference between Ni and YSZ [V].

In relation with charge-transfer reaction, the faradic current is shown as equation 4.4, electrochemical equilibrium is assumed;

$$i_f = zFl_{tpb}\left(k_f \prod_i \theta_{R,i} - k_r \prod_i \theta_{P,j}\right) \quad (4.4)$$

Where,

F = Faraday's constant,

l_{tpb} = the length of the three-phase boundary line per unit electrode area[m/m^2],

θ_R = i and θ_P,j are reactant and product surface coverages, and i and j run over all reactants and products, respectively.

The potential difference depends on reactant and product concentration (Nernst Equation), it leads to a complex a nonlinear dependence of exchange current density on the reactant and product concentration which is called equilibrium potential effect**.**

4.3.3 Surface Chemistry

The charge-transfer reactions are existed by the gas phase reactants and products due to the adsorption, desorption and surface reaction. Langmuir Hinshelwood type of surface reaction mechanism is accepted for Ni an YSZ surfaces, the surface reactions properties as given in Table 4.1 [42].

Table 4.1 The surface Reaction Properties [42]

Charge Transfer React.	Preexp. factor k_f	Act. energy E_f^{act}
$O^{-2}_{YSZ} + []_{Ni} \Leftrightarrow O_{Ni} + []_{YSZ} + 2e^-$	$8.6 \cdot 10^{-4}$ mol/(m s)	41 kJ/mol
$H_{Ni} + OH^-_{YSZ} \Leftrightarrow H_2O_{YSZ} + []_{Ni} + e-$	$4.2 \cdot 10^{1}$ mol/(m s)	153 kJ/mol
Nickel surface reactions:		
$H_{2\,gas} + []_{Ni} + []_{Ni} \Leftrightarrow H_{Ni} + H_{Ni}$	$S = 0.1$ (sticking coeff.)	–
$H_2O_{gas} + []_{Ni} \Leftrightarrow H_2O_{Ni}$	$S = 0.01$ (sticking coeff.)	-
$O_{Ni} + H_{Ni} \Leftrightarrow OH_{Ni} + []_{Ni}$	$5.0 \cdot 10^{22}$ cm^2/(mol s)	98 kJ/mol
$O_{Ni} + H_2O_{Ni} \Leftrightarrow 2\,OH_{Ni}$	$5.4 \cdot 10^{23}$ cm^2/(mol s)	209 kJ/mol
$OH_{Ni} + H_{Ni} \Leftrightarrow H_2O_{Ni} + []_{Ni}$	$3.0 \cdot 10^{20}$ cm^2/(mol s)	43 kJ/mol
YSZ surface reactions:		
$H_2O_{gas} + []_{YSZ} \Leftrightarrow H_2O_{YSZ}$	S = 1 (sticking coeff.)	-
$O^{2-}_{YSZ} + H_2O \Leftrightarrow 2\,OH^-_{YSZ}$	10^{19} cm^2/(mol s)	0 kJ/mol
$O^x_{O\,YSZ} + []_{YSZ} \Leftrightarrow V_0{}^{\cdot\cdot}_{YSZ} + O^{2-}_{YSZ}$	10^{-2} m/s	0 kJ/mol

On the Ni surface, reactions are assumed to take place between adsorbed H, O, OH and H_2O species. On the YSZ surface, reactions take place between adsorbed O^{2-}, OH^-, and H_2O species. For H_2O adsorption on YSZ, a typical maximum sticking coefficient of 1 is assumed. Lacking literature data, the surface H_2O dissociation kinetics and the O^{2-} surface/bulk exchange kinetics is set very fast to ensure continuous equilibrium. The bulk concentrations of $O^x{}_{O\,YSZ}$ and $V_O{}^{\cdot\cdot}{}_{YSZ}$ are set to constant values corresponding to ZrO_2-8 (mole) %Y_2O_3.

4.4 Thermodynamically Effects of Kinetic Parameters

The important point is that, the preexponential factors activation energies are consisted in every forward and reverse reaction which are dependant with each other.

However, they have a relation with the way of thermodynamically. The relations are explained in the equation 4.5 and equation 4.6.

$$E_f^{act} - E_r^{act} = \Delta H_R \tag{4.5}$$

$$k_f^0 - k_r^0 = \exp(\Delta S_R / R) \tag{4.6}$$

Where ΔH_R is the reaction enthalpy, ΔS_R the reaction entropy and

$$\Delta H_R = \Sigma hj - \Sigma hi \tag{4.7}$$

hi and hj are the molar enthalpies of the reactant i and product j. The values of the various species are given in the Table 4.2 at 700 ºC [47]

Note that a simple compilation of kinetic data from various literature sources will most generally violate thermodynamic consistency. Here, the use of an elementary kinetic description of charge transfer will only predict the correct equilibrium potential if all kinetic data are thermodynamically consistent.

Table 4.2 Thermodynamic data for various species [42]

Species	*h* [kJ/mol]	*s* [J/K mol]
H_2	19.9	155.6
H_2O	-216.9	221.8
O_{Ni}	-222	39.0
H_{Ni}	-31.8	40.7
OH_{Ni}	-193	106
H_2O_{Ni}	-273	130
$[]_{Ni}$	0	0
O^{2-}_{YSZ}	-236.4	0
OH^{-}_{YSZ}	-282.5	76
H_2O_{YSZ}	-273	98.1
$[]_{YSZ}$	0	0
$O^{x}_{O\,YSZ}$	-236.4	0
$V_0^{\cdot\cdot}{}_{YSZ}$	0	0

4.5 Porosity

Porosity represents the ratio of pore volume to the total volume. Porous structure is one key parameter to determine the efficiency of fuel cell. The porosity is necessary to gas diffusion through the anode side for providing the fuel oxidation at the interface of electrolyte and anode. The fuel cell produces current as soon as the electrochemical reactions are occurred. Fuel has to be continually transferred to the catalytic area to constitute the three phase boundary. The products from the reactions and the rest of reactants have to be removed from the catalytic active area. As a result, the gas diffusion can be achieved owing to porosity.

4.6 Reduction and Oxidation Cycle Effects to the Anode

As known, solid oxide fuel cell anode material is a composition of nickel and yttria stabilized zirconium cermets [47]. Nickel cermet anode reveals good catalytic activity towards the oxidation of hydrogen. Relatively to developing long term stability of the anode, nickel is typically mixed with yttria stabilized zirconium. Such a composition of the anode prevents delaminating and cracking of the electrolyte layer due to the thermal expansion mismatch as well as keeping the desired anode porosity. This approach improves long term mechanical stability of Ni/YSZ based materials operated under a reducing environment. The cycle reduction and oxidation of nickel will result in large bulk volume changes, which may have a significant effect on the integrity of interfaces within the fuel cell and thus may cause significant degradation on the performance. Exposure of nickel-cermet anode to reoxidation, however, results in change of the physical and mechanical properties that potential leads to failure of the cell. The kinetics of nickel oxidation is depended upon powder processing procedures, especially surface preparation, grain/particle size and impurity levels. Such an expansion could potentially result in an increase of the internal stresses of the nickel crystal structure which could affect the integrity of the cell. Additionally, volumetric changes over the electrode-electrolyte layer are likely to result in delamination of the electrolyte and micro- crack formation. The change in mechanical and microstructure properties of the anode is expected to affect both the mechanical strength and the electrochemical performance of the cell. However, the result of the studies highly depends upon the thermal plasma spraying technology to the substrate supported cell [48].

In order to develop a high performance Ni/YSZ cermet anode with improved long term stability, different NiO/YSZ composites varying in NiO content and NiO/YSZ particle size ratio have been relative to their porosity and the coefficient of thermal expansion (CTE) in the oxidized and reduced state. The CTE is dependent on the particle size of different NiO and YSZ qualities. Besides, high efficiency and high power output, the long term stability of SOFC is an important goal. Ni/YSZ show high degradation during long term operation that can be attributed to the agglomeration of Nickel particles. This leads to a loss of electrochemical active area and therefore an increase of the polarization resistance. It could be shown that the degradation rate strongly depends on the current density and the fuel utilization. It is assumed that either ohmic losses across thin electrical contacts or polarization losses at the three phase boundary locally increase the temperature and originate the agglomeration of the initial small nickel particles. Insufficient removal of water vapour results in Ni oxidation, which can be lead to agglomeration [49].

A porous NiO/YSZ anode will likely not experience such a drastic volume change upon the reduction or reoxidation due to expansion into the pores but any volume change may have a significant effect on the integrity of the interfaces within a fuel cell and thus result in significant performance degradation. Ni oxidation generally allows a parabolic trend at the temperature greater than 1000 ^{o}C with activation energies typically of the outward bulk diffusion of Ni in NiO; however, at temperatures less than 1000 ^{o}C may studies have observed that the kinetics tend to diverge from parabolic kinetics and the activation energy or re-oxidation decreases. This trend indicates that a short-circuiting mechanism, such as transport along grain boundaries and/or dislocations, begins to dominate the kinetics at temperatures less than 1000 ° C. This observation is supported by the fact that Ni oxidation kinetics seem to be very sensitive to the preparation procedures, especially surface preparation, grain/particle size and impurity levels. Different impurity levels and preparation procedures will lead to a different concentration of short-circuit paths and might explain the large spread in literature values of oxidation activation energy [50].

5. EXPERIMENTAL PART

The main task of this master thesis is to investigate the behavior of anode and electrolyte under redox atmosphere. In this work, the effects of redox cycle on the electrochemical performance of full cell are performed and redox cycle effects on the half cell are defined with leak rate and permeability measurement. In addition, microstructural changes are studied by Scanning Electron Microscopy (SEM) analyse. Figure 5-1 gives an overview of the different characterization methods applied to the cell and its components. These are divided into electrochemical and microstructural investigations. This enables iterative improvement of the spray process and ensures the overall quality of the cell component.

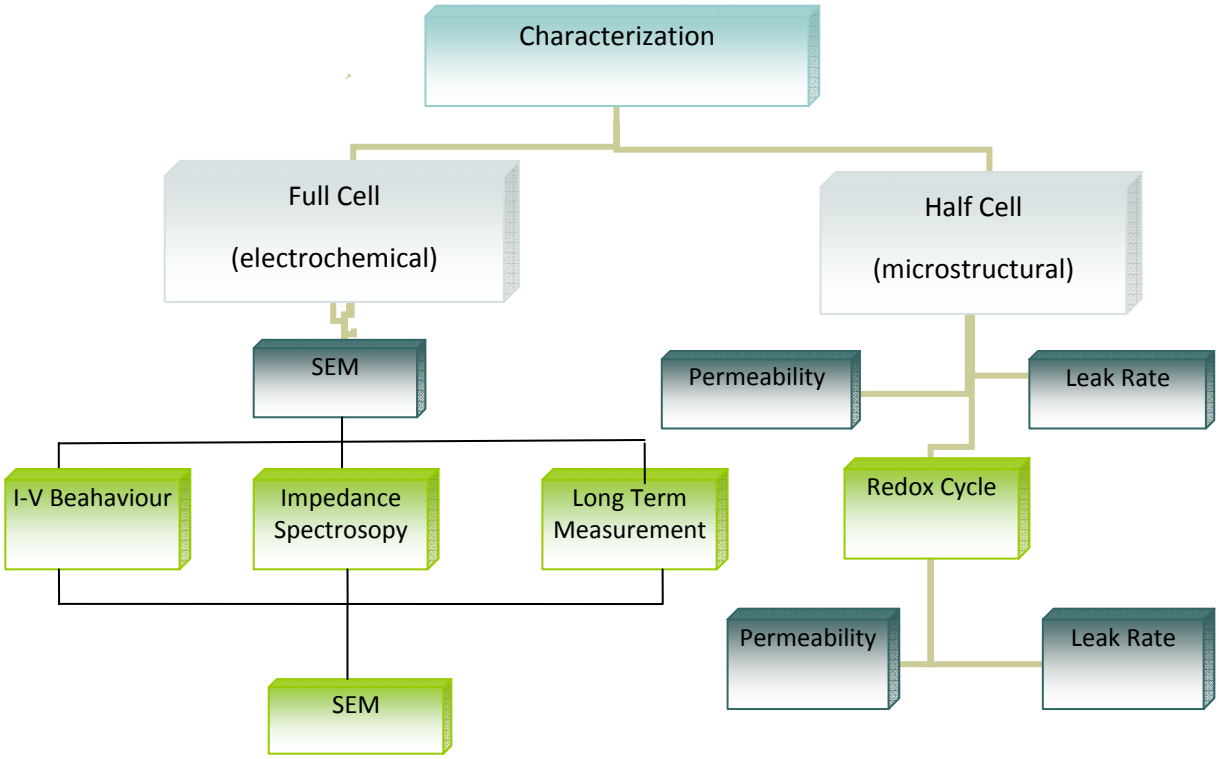

Figure 5.1 The chart of the characterization methods applied to the cell and its components

Three main subjects are represented in experimental part. First of all, the cell production technology, principles and used special parameters are mentioned in detail. Next important point is the procedure of electrochemical analyse. The last one is microstructural investigation which included redox cycle in furnace as well as leak rate and permeability measurement.

5.1 Production of the SOFC Functional Layers

The experiments were performed in two stages; therefore the cells have been divided into two groups. The first group was full cell which contained all the components and the electrochemical experiment has been applied with them. The second group was half cell and the redox cycle effects were measured with them by leak rate and permeability measurements. Leak rate measurement was applied to the half cell which had substrate, anode and electrolyte. Permeability measurement was applied to the half cell which had substrate and anode.

The cathode, anode, and electrolyte of the substrate supported SOFCs were produced by Thermal Plasma Spray process at DLR in the facility “DC 1.” This system is composed of a vacuum chamber where VPS parameters are controlled by a Plasma Technique (A 2000) control unit.

A contact layer to provide electrical conductivity is necessary on the cathode layer for the full cells which were used in electrochemical analyse. For this purpose, LSCF was screen printed on the cathode layer with a fine platinum layer, and then LSCF was left to dry in the room temperature for 12 hours. The contact paste, which improved to contact between platinum mesh and cathode, behaves as a current/voltage collector. By this way, overpotential of cathode side was decreased.

The Electrolyte, anode and cathode layers were deposited using vacuum plasma spraying while the contact layer was later on pasted onto the cathode, before electrochemical characterization. The properties of the used powders are detailed in the Table 5.1.

Table 5.1 Properties of the powders used

Application	Anode	Electrolyte	Cathode
Material	Nickel +YSZ Agglomerated	Yittriastabilized zirconia (ZrO_2-8 (mole)%Y_2O_3)	$LaSrFeCoO_3$
Chemical Composition	30 Vol % Ni 50 Vol% YSZ	ZrO_2-9,5(mole)% Y_2O_3	$La_{0,6}\ Sr_{0,4}\ Co_{0,4}\ Fe_{0,6}\ O_3$
Size mm	< 55	<50	~40
Supplier	Bacon/HC Starck	HC Starck	HC Starck

Here are given the actual parameters used for depositing the cell layers (Table 5.2). These parameters have been selected as a result of the DLR experience in SOFC processing. As mentioned previously, for SOFC application dense electrolyte layers are required to be deposited. This can be achieved by striking the completely melted high velocity particles on the substrate. The maximum melting of the particles is ensured by using high power input i.e. 43 KW. The high velocity of the particles is achieved by reducing the chamber pressure to 80 mbar.

Unlike electrolyte anode is required to be porous. Therefore power input is lowered to 43 KW while the chamber pressure is increased to atmospheric [11].

Table 5.2 Plasma parameters for spraying

Properties	Anode	Electrolyte	Katode
Powder	NiO/YSZ	YSZ	LSCF
Plasma Nozzle	Mach 3 Laval, di=7 mm	Mach 3 Laval	F4V/02, di=7 mm
Powder Injection	NiO: Intern, from below, $+15^0$	intern from above, $+15^0$	intern from above, -15^0(Aganist Jet direction)
Injection diameter[mm]	3	3	3
Power[kW]	23	43	22
Plasma Gas[slpm]	Argon:22	Argon:54	Argon:30
Plasma Gas[slpm]	Helyum:8	Helyum:24	Helyum:20
Plasma Gas[slpm]	Hydrogen:0,8	Hydrogen:2	Hydrogen:0
Torch-Substrate Gap[mm]	110	260	90
Course Gap [mm]	10	5	10
Feed Rate [mm/s]	400	20	300
Number of Layers	9	6	1
Chamber Pressure[mbar]	Atm	80	Atm
Enthalpy(kJ/kg)	15890,14	16353,98	12180

5.2 SOFC Electrochemistry Test Bench

In this work, the SOFC electrochemistry test bench called DLR 11, was used in order to accomplish the electrochemical characterization of the SOFCs. It is designed to characterize one planar cell with a diameter of 48 mm and an active area of 12.57 cm^2. Four different cells were operated in the same test bench with the same measurement parameters in order to make the results comparable one to another. This section will discuss the electrochemical characterization of the SOFCs in regards to obtaining a I-V performance curves as well as EIS. The test bench is composed of two main parts the furnace and the control system, could be seen in Figure 5.2.

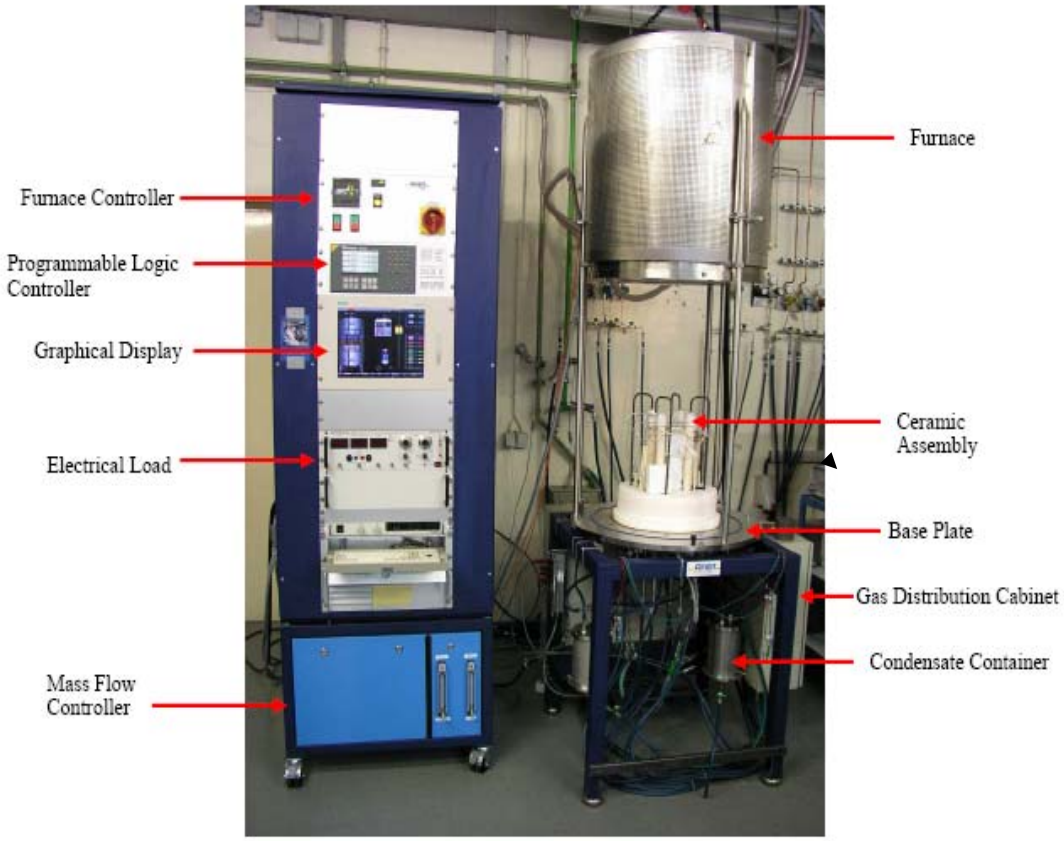

Figure 5.2 SOFC Test Bench, "DLR 11" [DLR, Stuttgart]

5.2.1 Furnace

The cell, ceramic gas tubes, thermocouples and current/voltage measurement connections are mounted on the stainless steel plate which is situated below the furnace. The furnace is used to provide the necessary operating temperature for the whole system (maximum temperature 1100 °C). The control of the furnace is accomplished by a Eurotherm™ controller which allows programmed heating up/cooling down procedures with a number of ramps running automatically. The signals of the thermocouples placed at different measurement points are displayed on the screen.

5.2.2 Control system

The control system of the test bench consists of a programmable logic controller (PLC) system (Appendix 1). Under the base plate there are two condensers, one for the anode and the other for the cathode exhaust gas dehumidification. The electrical components like PLC module and transducers are placed at the back side. The gas

supply to the cell is accomplished by the mass flow controllers. A computer is connected to the system to record and/or change the data of the measurement parameters, like gas flow rate, gas pressure, cell voltage, temperature etc. An electronic load with a maximum current of 50 A is connected to the cell in order to draw current out from the cell.

5.2.3 Installation of the Cell in the Test Stand

A cross sectional view of a SOFC, which is mounted into the test bench for electrochemical characterization, is shown in Figure 5.3. The cell is placed between the ceramic bases for the anode and the cathode in Figure 5.4. The current collection from the cell is accomplished by two coarse platinum meshes; one under the substrate and the other over the cathode. Platinum wires are welded to those meshes, thereby completing the external circuit of the system [51].

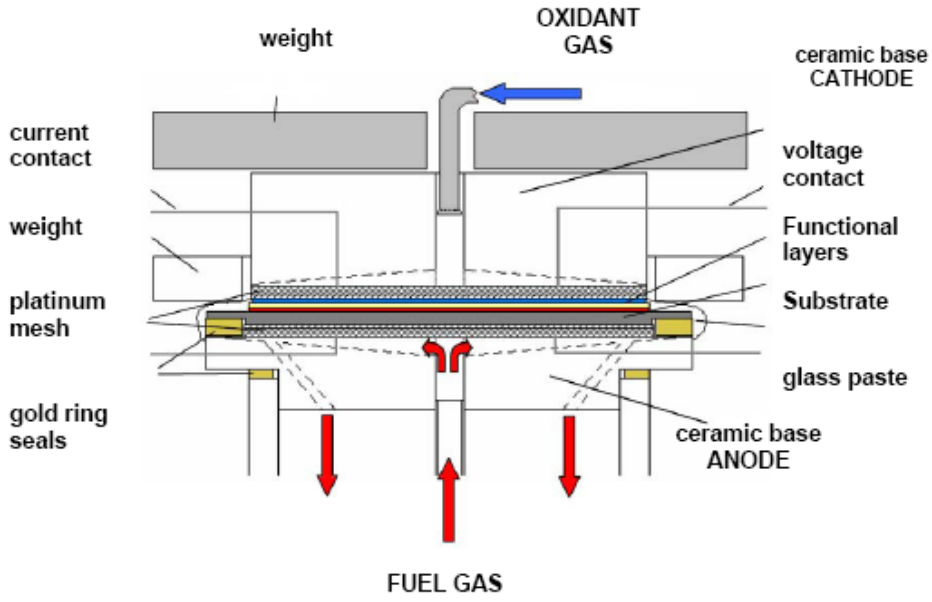

Figure 5.3 Cross sectional view of a SOFC integrated into test Bench [61]

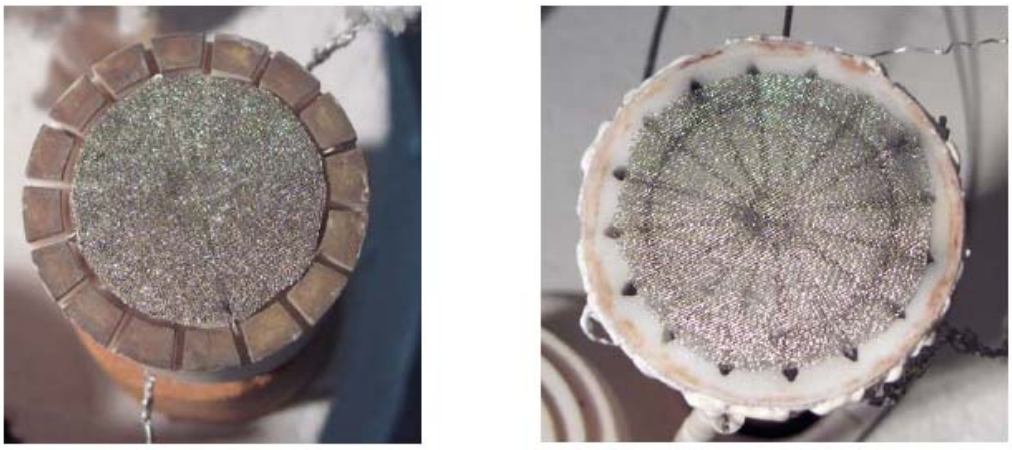

Figure 5.4 Gas distributor of the cathode side (left) and the anode side (right) with a coarse platinum mesh [DLR, Stuttgart].

The fuel gas feed and exhaust is achieved by two ceramic tubes. The fuel gas feed is supplied upwards through the thin tube and the exhaust gas is directed downwards through the channel between the two tubes. The anode gas chamber is isolated by sealing two gold rings (see Figure 5.3). In addition to that, 2-3 layers of glass sealant paste is used to seal the substrate and the gold ring. The gas sealant is heated to 80°C for drying. The glass sealant consists of alkaline earth borosilicate [17].

5.2.4 Start up Procedure

Before the cell testing starts, several steps are required in order to improve its performance.

The first step carried out on a cell is the heating-up. The temperature is just modified based on the variation given in Figure 5.5. No load is applied during this step. 0,25 slpm gas mixture of 5% H_2 in Ar is supplied to the anode and 0,25 slpm air to the cathode. The temperature is gradually increased from ambient temperature to 880°C at a rate of 3 ºC/min. After reaching 880°C the temperature is maintained constant for about 5 hours in order to allow the crystallization of the glass sealant. The cooling-down to 770°C is carried out at the same rate as the heating-up.

5.2.4.1 Reduction steps

At 770°C the cells will successively be supplied with a mixture of hydrogen and nitrogen on the anode side, until the amount of hydrogen is about 50%. At the same time the volume flow of the fuel gas of the anode side and the volume flow air of the

cathode side is increased to 1 slpm and 2 slpm, respectively. Thus NiO is reduced to Ni, which resulted in an increase of the porosity of the anode. The two previous steps are resumed on the Figure 5.5.

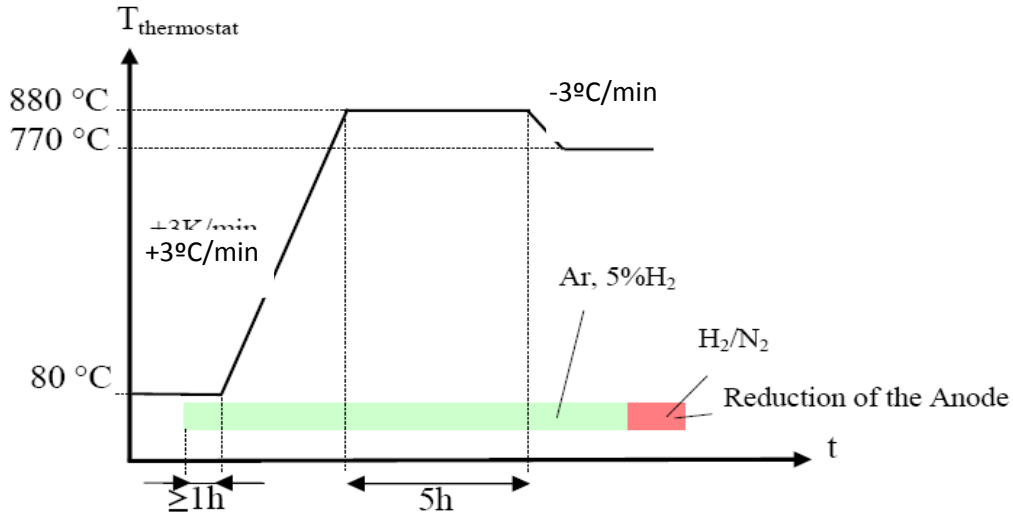

Figure 5.5 Temperature cycle during heating up and reduction steps of a cell cycle

5.2.4.2 Activation

The first I-V curve of the cell is carried out after the reduction phase at 800°C with a gas supply composed of 0.5 slpm H_2 and 0.5 slpm N_2 at the anode as well as 2 slpm air at the cathode. Then a long-term electrical load of 200 mA/cm^2 is applied to the cell during 15 hours with the same temperature and gas parameters.

5.2.4.3 Experiment

After the first steps the parameters of the cell can be varied in order to study its performance. The performances at standard conditions as well as during a temperature variation and a gas variation were studied. The current - voltage curve between the OCV and 500 mV was plotted for each characterization. As well as two spectra of EIS at a zero current and with a 200 mA/cm^2 loading were recorded. This type of characterization is a good way to be aware of the performance of a cell for precisely each layer during its work. Between specific measurements the cell is loaded at 200 mA/cm^2 in order to simulate a long term loading. The life cycle is plotted all long the operating time which allow to summarize all the steps and to evaluate the behaviour at long term loading.

All the measurements are performed at 0.5 slpm of N_2 with 0.5 slpm of H_2 at the anode side and 2 slpm of air at the cathode side except during the fuel gas variation. In fact, two different gas variation experiments were also carried out in order to evidence the influence of the gases. The first gas variation experiment was to investigate the effects of fuel gas and oxidant gas amounts to the anode and cathode (seen in Table 5.3). The second gas variation experiments were also performed in only fuel gas amounts (between 0,5 slpm and 0,0625 slpm H_2 to the anode side) while the oxidant gas was constant (2 slpm Air).

Table 5.3 Fuel gas and oxidant gas amounts to the anode and cathode

Gas at the anode [slpm]	Gas at the kathode [slpm]
0,5 H_2 0,5 N_2	2,0 Air
0,5 H_2 0,5 N_2	2,0 O_2
1,0 H_2	2,0 O_2
1,0 H_2	2,0 Air

The major electrochemical characterizations were carried out at 800°C. Temperature variation simulates the temperature fluctuations of the system. The heating-up of the cell is carried out by the furnace, while the cooling-down is not due to a freezing system. During temperature variation, measurements were applied at 850°C, 800°C, 750°C and 700°C successively with a supply of standard gas (0.5 slpm H_2 + 0.5 slpm N_2 at the anode and 2 slpm air at the cathode).

5.2.4.4 Current Voltage (I-V) Characteristic Curve

One of the most commonly used performance evaluation techniques for fuel cells is the "current-voltage curve". The current and voltage values are taken and recorded via the four-point measurement method. During the measurement it is crucial to have a constant temperature in order to avoid the influence of temperature. In order to be able to compare the plot of different cells, current density is used rather than current itself. Current density is the measured current divided by the active area of the cell and usually has the unit of "mA/cm²". The plot is named as "I-V curve." Generally, the slope of the curve is the internal resistance of the cell. The over potential is not

constant but it changes with the current flowing through the system. In this measurement the current and voltage of the cell are recorded as the cell is gradually loaded starting from the OCV down to a defined cell voltage and plot as seen in Figure 3.2 is produced. Furthermore, this plot allows one to analyze the power performance of the cell. In order to determine the power, the comparison among the cells is made such that the data points are extracted at the operating point of 700 mV. Furthermore, the total resistance of the cell can be determined by the slope of the I-V characteristic curve at this respective operating point. The I-V curve is recorded over a gradual, controlled load of the SOFC cells through the electrical load of the SOFC test bench. Moreover, load characteristic curve until a specified, minimum voltage value is reached. After the minimum voltage values are reached, the cell current is gradually brought back to zero. With the comparison of the upward and downward curve of the load curve, one may determine which electrode the activation process takes place.

5.2.4.5 Impedance Spectroscopy Measurement

When beginning an electrochemical investigation, very often one may know little or nothing about the process or mechanisms being studied. The determination of the Electrochemical Impedance Spectroscopy (EIS) can be a very useful tool to help formulate a hypothesis. EIS data and equivalent circuit model provide a useful tool to illustrate the electrochemical problem. As can be seen from Figure 3.2, there are many losses which occur in the SOFC. Although these losses may not be eliminated, they can be minimized. EIS is performed to determine the loss mechanisms in the cells during operation.

5.2.4.6 Measurement Principle

Methods employing excitation with a sinusoidal signal and analysis of the currents produced of an electrochemical cell were the first employed way of measuring the rate constants of fast electron transfer reactions. The voltage drop over the test sample is measured over the reference and sense electrodes. With impedance spectroscopy, an AC voltage is applied by a frequency analyzer/generator with small amplitude on the phase interface where the resulting current is measured. The frequency is varied between 100 mHz and 1 KHz and with an amplitude of 10 mV. The generated current has a phase shift compared to the voltage. This is to be

understood in the way that the real part of the equation describes the actual physical process.

$$Z = \frac{V(f)}{I(f)} = (\frac{\hat{V}}{\hat{I}}).\exp(j.\Theta) = \mathrm{Re}|Z| + i \times \mathrm{Im}|Z| \quad (5.1)$$

Where,

V = Voltage

I = Current amplitude,

Re Z = the real part of the impedance,

Im Z = the imaginary part of the impedance,

j = the complex number

(j^2 =-1), and (-Θ) is the phase shift. The impedance is a complex resistance encountered when current flows through a circuit made of resistors, capacitors, or inductors. Impedance is an important parameter used to characterize electronic circuits, components, and the materials used in production of components. A fuel cell system can be considered as an electrical circuit with various components. The partial impedance of every component in the circuit contributes to the overall impedance of the device. In fuel cells, the main contribution results from the porous layers of anode and cathode which are responsible for the reduction and oxidation reactions. In addition, the resistance of the electrolyte, contacts, connectors and the inductance of the body and connectors are also part of the overall resistance measured [52].

5.2.4.7 Impedance Measurement Device

In this work, the impedance measurement and data acquisition, called the IM6, is performed using a measuring system from Zahner Elektrik based in Kronach, Germany. The IM6 is equipped with a programmable potentiometer/ galvanometer and a frequency analyser/generator. Figure 5.6 shows a schematic of the system implemented at DLR for the impedance measurement of SOFCs.

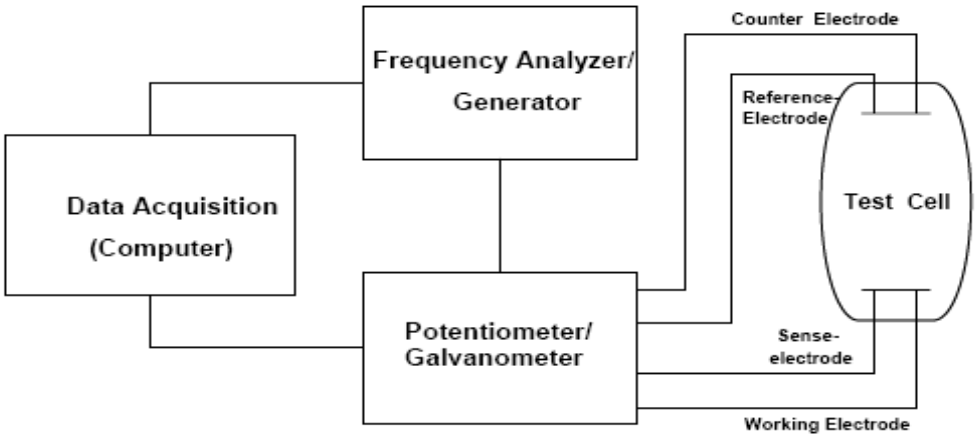

Figure 5.6 Schematic of Impedance Measurement Device at DLR

5.2.4.8 Nyquist and Bode Diagrams

Using the measured and calculated data points two different types of diagrams can be plotted. The Nyquist diagram displays real versus imaginary part of the measured impedance. In the Nyquist diagram semi circles representing different processes are observed. However, in most of the cases they overlap and it becomes difficult to define the impedance value corresponding to each process. In an SOFC, the first intersection point of the real axis is the ohmic resistance and the last intersection is the overall impedance of the system. The semi circles observed in between are the polarization resistances. The Bode diagram displays the impedance and phase angle versus the frequency range of the measurement. In Bode diagram it is possible to observe different processes analyzing the shape of the phase-angle curve. A turning point or a local minimum indicates the border between two processes [53]. In a SOFC the frequency where the phase angle shows zero, is the frequency at which the ohmic resistance is measured. The overall cell resistance is observed at low frequencies. The polarization resistance can also be determined by the overall cell resistance which occurs at the maximum at low frequencies subtracted by the Ohmic losses which occurs at the minimum (where the phase angle is zero).

5.2.4.9 Equivalent Circuit

Applying the EIS at various experimental conditions; such as different gas compositions, temperatures and electrical loads, the measured cell impedance, in the case that they are loaded, can be split up into anode impedance, cathode impedance and electrolyte resistance [34]. An equivalent circuit can be applied for the

simulation of the measured impedance spectra of the SOFC in order to define the specific processes contributing to the measured impedance. This circuit is composed of resistance, capacitance and inductance elements connected in series and parallel, each representing an electrochemical process. In the equivalent circuit diagram is represented in Figure 3.3. The process on the electrochemical boundary layer is represented in the equivalent circuit connected in series as Resistance and Capacitance (RC) elements. The number of RC elements is dependent on the number of independent, differentiable single processes in the impedance spectrum[34].

5.3 Redox Cycle with Furnace

The furnace is made by the company of GERO, could be seen in Figure 5.7. It consists of a framework with integrated trafo cabinet and a tube furnace. Four controlling elements (Eurotherm 818) are installed into the trafo cabinet. The removal of storage part is built in a tube furnace which integrated with Pythagoras Ceramic tube. It is surrounded by a continuous heating spiral from Kantahl A1 wire. The tube ends are closed by medium flange to prevent accessing of the athmosphere air. A vacuum pump is placed next to the trafo cabinet. This is connected by a hose with Pythagoras ceramic flange. At the other side of tube end, a hose is attached to the flange which has a connection with the pipe. The argon-hydrogen mixture, nitrogen and air was supplied by this pipe.

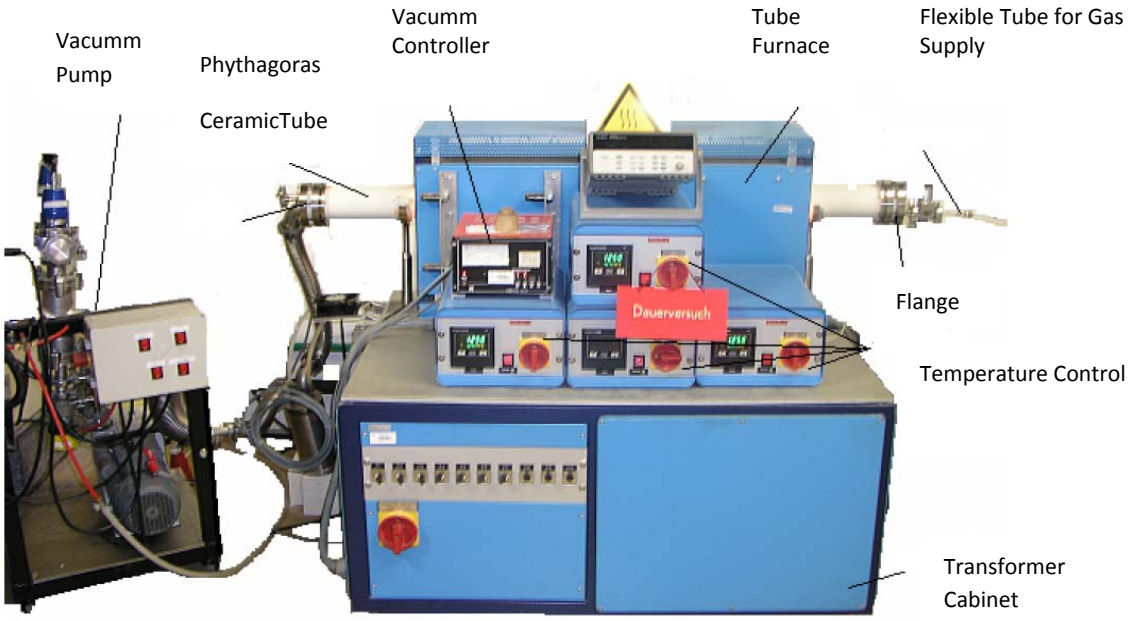

Figure 5.7 Tube Furnace for Redox Cycle

At the beginning of the experiments, four cylindrical cells (two substrate+sprayed anode and two substrate+sprayed anode+sprayed electrolyte) were embedded onto the rectangular ceramic plates and placed in the centre of the pipe hole. The isolated flange (to cover from high temperature) was used for blocking the air and also evacuating the gas outlet from the open tube side. In this tube side, vacuum was arranged to 3-10 mbar. Next step was arranging the gas flow rate which could be seen in Table 5.4. Control elements were regulated through the procedure of the experiments. A homogeneous temperature field was adjusted by the use of several automatic controllers in the pipe.

Table 5.4 Gas variation and rate for the redox cycle in the furnace

Gas Variation	Rate(l/h)
Ar+5%H2	15
Nitrogen	54
Air	10

Half cell samples (substrate+sprayed anode and substrate+sprayed anode+sprayed electrolyte) were reduced and re-oxidized in the furnace at 800°C. The heating ramps and overall typical thermal cycle was shown in Figure 5.8 and Figure 5.9. The reduction of samples was performed in 15 l/h at Ar+5%H_2 atmosphere. Reducing atmosphere is maintained in the furnace during heating and cooling of the samples (by sending Ar+5%H_2).

Re-oxidation was done in 10 l/h flow of air for 2 hours. Furnace was flushed with N_2 after each oxidation cycle for 30 minutes before reducing cycle for 2 hours. There were 5 runs of redox cycle; first run was only reduction, second run was 1 reduction and 1 redox, third run was 1 reduction and 5 redox, forth run was 1 reduction and 10 redox, fifth run was 1 reduction and 15 redox. In this furnace, two heating ramps were applied to reach the operation temperature. The first heating ramp was 600°C/h from ambient temperature to 700°C, and then the second heating ramp to reach the operation temperature was 300°C/h. The samples were reduced 2 hours in the furnace after reaching the operation condition. Afterwards the cooling ramps were the same with the heating ramps.

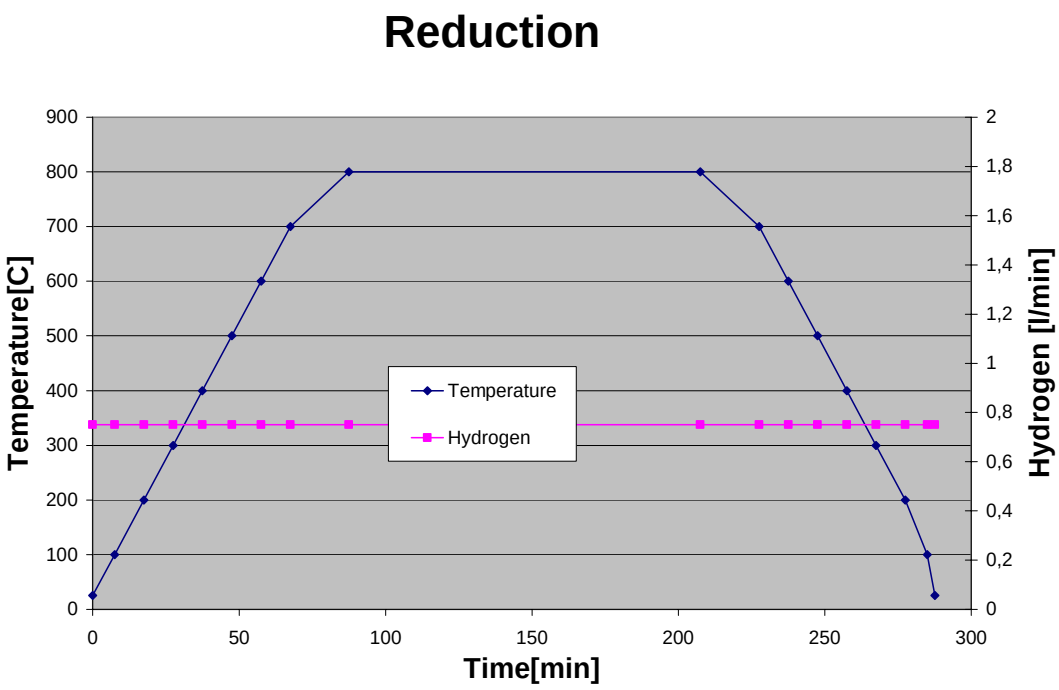

Figure 5.8: Variation of operating parameters for the reduction

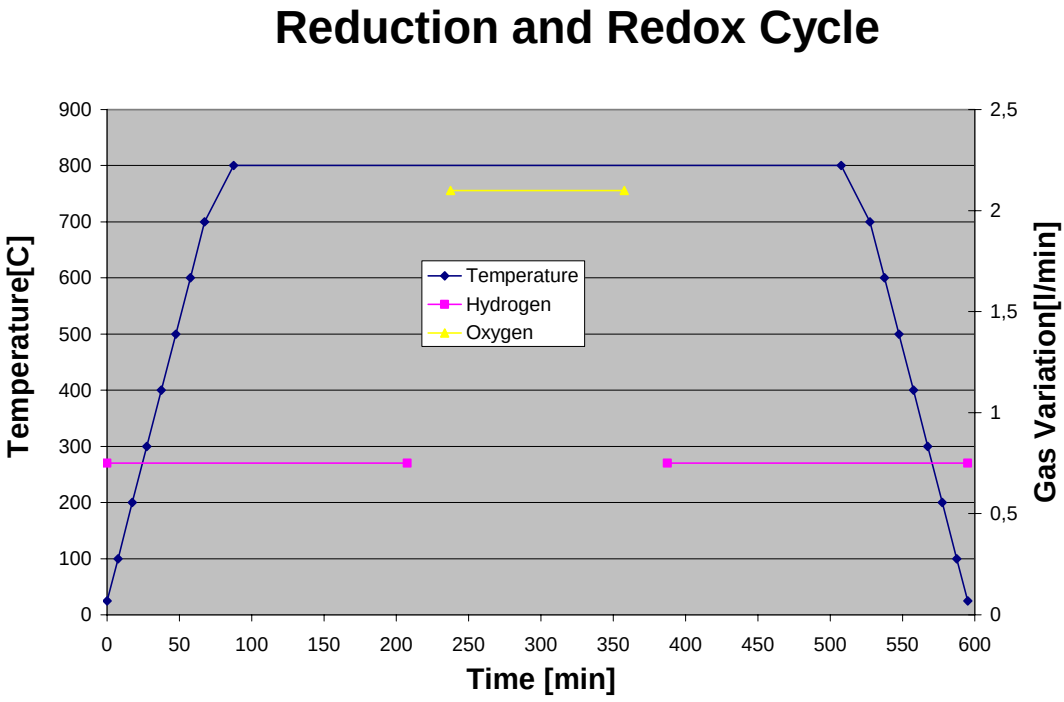

Figure 5.9 Variation of operating parameters for the 1 reduction and 1 redox cycle

5.4 Pre-Post Test Examinations

Pre and post investigation for the full cell (substrate+anode+electrolyte+cathode) which are used in the electrochemical analyse, were applied by using the scanning electron microscopy (SEM). SEM was performed after production (by Thermal Plasma Spray) of the cell to see oxide layer formations and element point analysis as well as observe roughly the porosity. Same procedure was applied after the electrochemical experiment to observe any changes i.e. structure changes, material diffusion processes and phase changes/formation occurring during the experiment

Pre and post investigations for the redox cycle groups which were half cells (substrate+sprayed anode and substrate+anode+electrolyte+cathode), were divided into two parts; leak rate and permeability measurements. The leak rate of electrolyte was performed with the leakage ratio while feeding the gas through the electrolyte layer. As well as the permeability of anode was measured with pressure drop methode.

Finally, mapping was done to check cracking and delamination effect to the performance of the nanostructured anode under the reduced atmosphere.

5.4.1 Scanning Electron Microscopy

Scanning electron microscope (ZEISS Leo 982) was used for taking the micrographs of the full fuel cell samples. The scanning electron microscope uses electrons rather than light to form an image. It uses a highly focused electron beam to strike and interact with a sample which is contained in a high vacuum environment to form a high resolution image. The images formed by the SEM are from secondary electrons, backscattered electrons, characteristic x-rays, Auger electrons, and others that are emitted by the sample. Therefore the sample to be examined has to be conductive.

At the lowest magnifications, SEM resolution is limited by the pixel size. The finest detail cannot be smaller than the size of an individual pixel. The resolution, therefore, is fractions of a micrometer. The magnifications higher than 100,000x, is possible to be reached by this equipment.

5.4.2 Leak Rate Measurement

Although electrolyte layers produced through thermal plasma spray, still there is left some porosity and micro cracks, causing leakage of fuel gas. This leakage of fuel through electrolyte causes a decrease in open circuit voltage, thus a loss of fuel. Therefore it is very important to know the gas tightness of the electrolyte layer. In the following section basic operating principle and the construction of the stand is being described.

5.4.2.1 Leak Rate

The gases like Helium, oxygen, and air follow the ideal gas law at low pressure (0-1 bar). Ideal gas law can be written in terms of molar mass M of a gas and its mass m as

$$pV = m\frac{RT}{M} \tag{5.2}$$

Where;

M = Molar mass
m = Mass
V = Volume
R = Gas Constant
T = Temperature

Volumetric flow rate is defined as

$$q_v = \frac{\partial v}{\partial t} = \dot{V}\left[\frac{cm^3}{s}\right] \tag{5.3}$$

Differentiating (5.3) with time gives the volumetric flow of the gas

$$\frac{\partial v}{\partial t} = \frac{1}{p}\frac{\partial m}{\partial t}\frac{RT}{M} \tag{5.4}$$

Or using (5.4)

$$q_v = \dot{V} = \frac{1}{p}\dot{m}\frac{RT}{M} \tag{5.5}$$

Rearrangement gives

$$q_{pv} = p \times \dot{V} = \dot{m}\frac{RT}{M} \tag{5.6}$$

$$q_{pv} = q_l$$

So,

$$q_l = p \times \dot{V} = \dot{m}\frac{RT}{M}\left[\frac{mbar \times l}{s}\right] \tag{5.7}$$

This $p \times \dot{V}$ according to DIN 28402 is defined as leak rate (q_l). P is basically the pressure difference (P_{higher}-P_{lower}) that is causing the flow of gas. The temperature must be specified [55].

5.4.2.2 Pressure Rise method for Leak Rate Measurement

Figure 5.10 shows a schematic arrangement for leak rate measurement by pressure rise method. There lies P_a high pressure on the exterior side of the sample while low pressure on the P_i inner side. Therefore due to pressure difference (P_a - P_i) gas flows from the outer to the inner side. This gas flow is described as the leak rate.

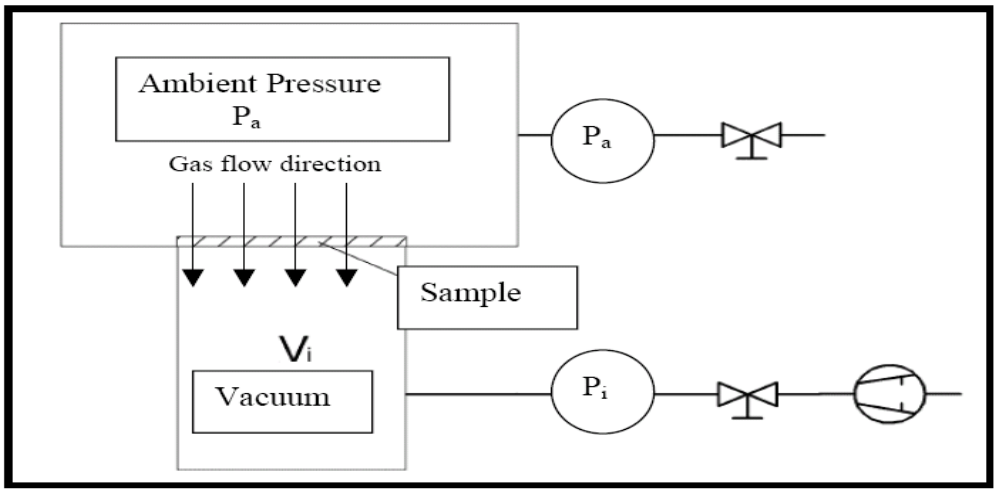

Figure 5.10 Pressure rise method for leak rate measurement

For measurement of leak rate the sample is sealed and clamped between two chambers (having different pressures). One chamber is flushed with a gas air/Ar to maintain ambient/higher pressure P_a. The other chamber with volume V_i is evacuated and closed tightly. By a pressure sensor (P_i) the pressure rise ΔP_i in the evacuated chamber, during time Δt is measured. So the total amount of gas that has flown into the evacuated chamber is

$$\Delta(P_i \times V) = q_l \times \Delta t \tag{5.8}$$

As the evacuated volume is constant so above equation becomes

$$q_l = V \frac{\Delta(P_i)}{\Delta t} \tag{5.9}$$

If $P_{i,0}$ is the initial pressure and $P_{i,t}$ is the pressure after Δt time interval then above equation becomes

$$q_l = V \frac{(P_{i,t} - P_{i,0})}{\Delta t} \left[\frac{mbar \times l}{s} \right] \tag{5.10}$$

$$q_{pv} = q_l$$

In order to have uniform and comparable leak rate for a variety of test samples, the leak rate based on surface area A_s of sample is defined.

$$q_l = V \frac{(P_{i,t} - P_{i,0})}{A_s \times \Delta t} \left[\frac{mbar \times l}{cm^2 s} \right] \tag{5.11}$$

5.4.2.3 Leak rate measurement Apparatus

The test stand measures the leak rate at room temperature, and is based upon the pressure rise method. A three-way valve (Whitey, Swagelok (SS43×S6MM) in extension line connects the stand to these samples. The schematic description of the apparatus is shown in Figure 5.11-5.12.

The major parts of the stand are

- Vacuum Pump (Two-Stage High Vacuum Pump with a single phase motor, Edwards E2M5)
- Pressure sensors [Range 0 to 1 bar (abs)]

- ❖ Flow Controller (EL-Flow Mass flow controller from Bronkhost)
- ❖ Computer (for control and data processing)

Figure 5.11 Leak rate measurement apparatus

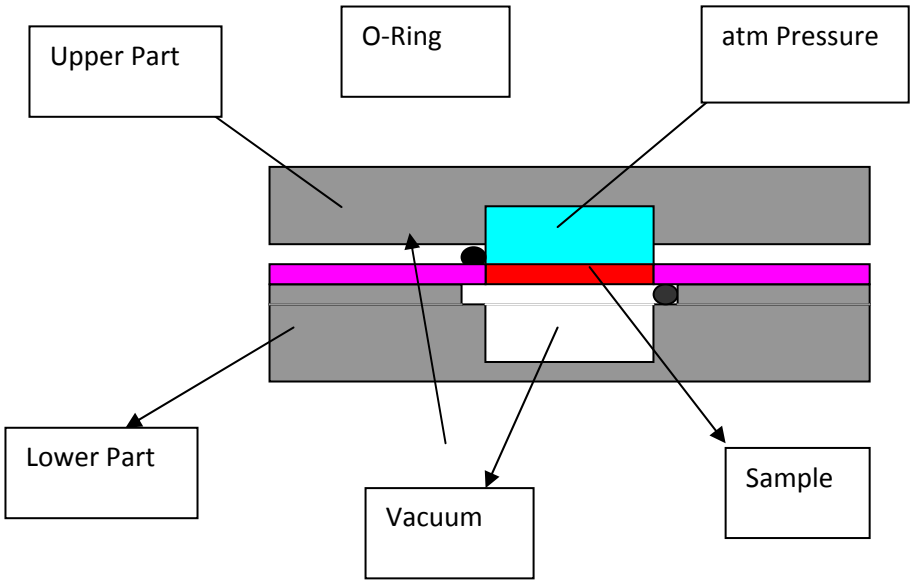

Figure 5.12 Schematic of Test Stand for Leak Rate

Two pressure sensors are used for measurement of pressure. One measures the upper part pressure [Atmospheric pressure is maintained in the upper part by flushing it with a very small flow of gases like Ar/He] and the other measures the pressure in the evacuated volume (lower part). Both of the pressure sensors work on the principle of piezzoelectric effect, in which the pressure exerted on a dielectric crystal generates voltage. In order to avoid sudden pressure rises and flow irregularities a flow controller is used. The flow controller ensures a constant flow rate. A flow rate of maximum 0.5 l/min is recommended to avoid any cracking of the layer by stresses. If the sample is sufficiently porous, the pressure inside the evacuated volume V_i will rise rapidly. For such cases the volume of the evacuated chamber must be increased, in order to ensure a slow rise in pressure. This is accomplished through a header/buffer flask attached to the test stand. For less porous/leak tight samples this header/flask can be separated from the test system through an on/off valve. Another on/off valve separates the vacuum pump from the test system

5.4.2.4 Data Acquisition and Processing

For recording and saving the data from test stand, a computer program is developed using Pro-VEE (Visual Engineering Environment). VEE is a graphical package from Agilent Technologies USA for developing; measurement, control, test, and data-acquisition applications. The data taken from the pressure sensors (Time Versus to pressure) is recorded and displayed continuously on a screen during the test (Figure 5.13). At the end of the test(when $P_i \approx P_a$) all the received data is saved in the form of a file in the specified directory. This data file can be opened and evaluated by using the Microsoft Excel spread sheet. In order to compare all the cells, leak rate is specified at vacuum chamber pressure for which the difference between vacuum chamber and upper part pressure is 860 mbar. The reason is that in actual operation of the SOFC there has been observed a vacuum pressure 100 mbar maximum between cathode side and anode side. The schematic operation sequence for the measurement is given in the Figure 5.14.

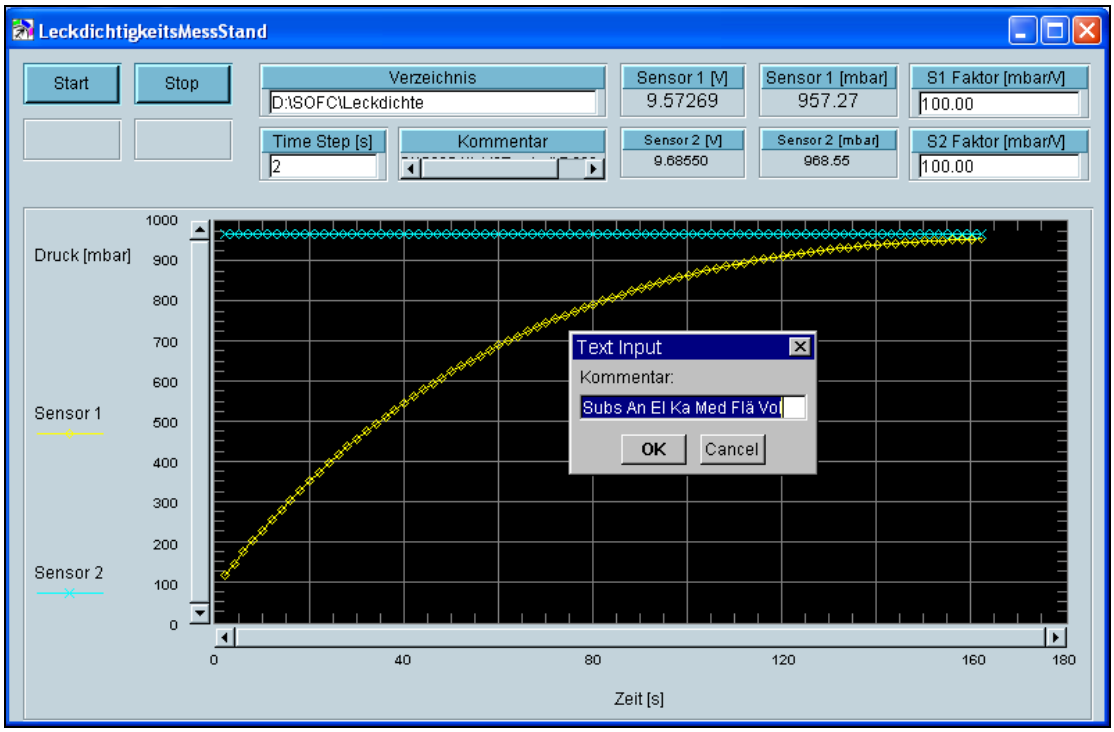

Figure 5.13 Data Display during the Test

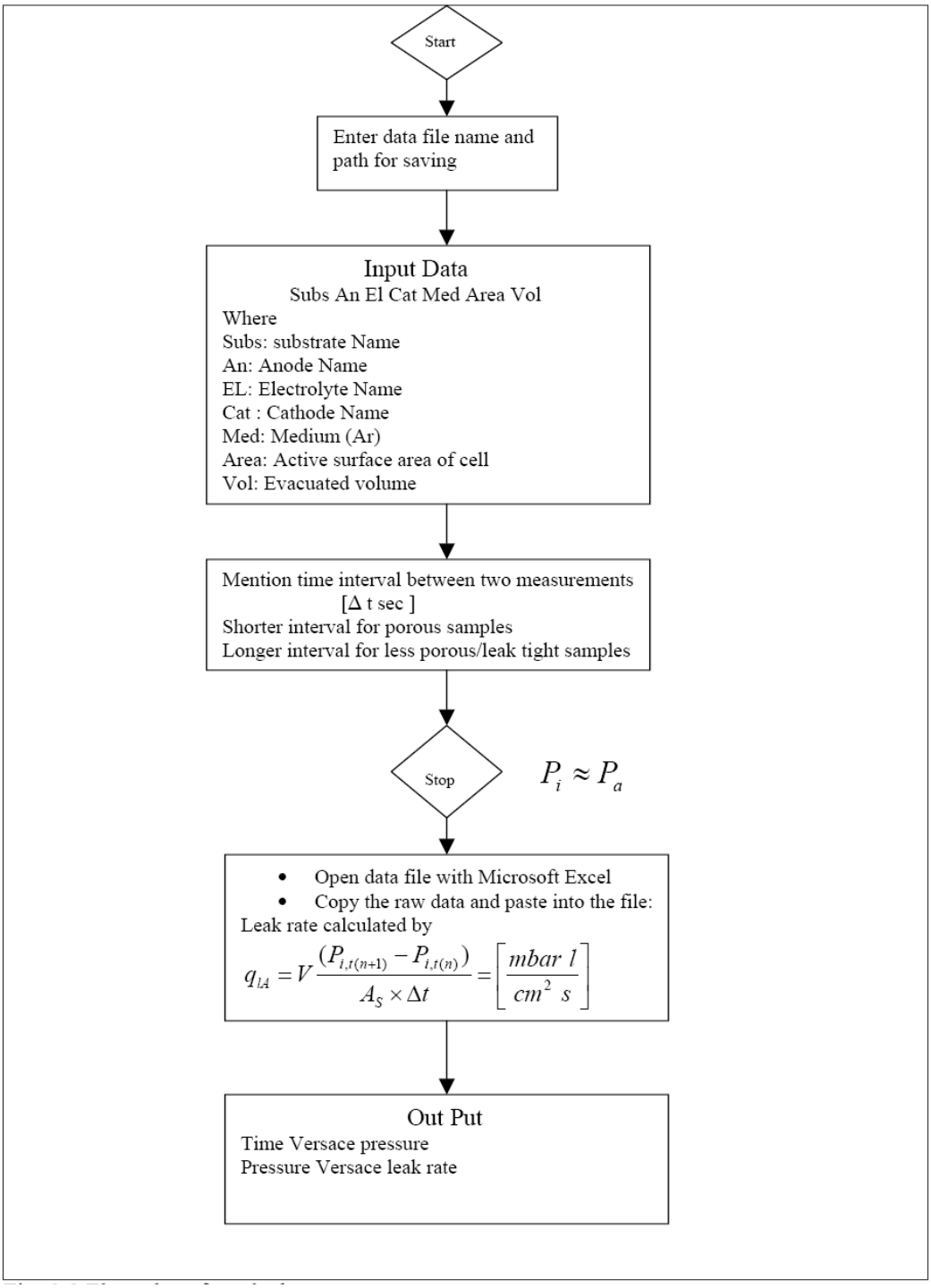

Figure 5.14 Flow chart for a leak rate

5.4.3 Permeability

The principle of permeability measurement at DLR is based on the measurement of the flow of a test fluid (known viscosity and density) through the sample and the pressure drop across the sample as well as volumetric flow rate. The sketch of permeability test is shown in the Figure 5.15.

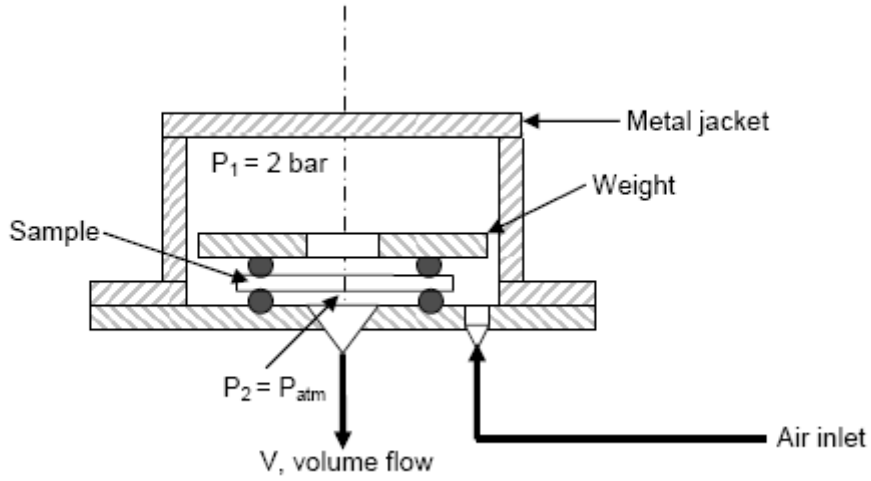

Figure 5.15 The Sketch of Permeability Test

The anode layer sprayed over the substrate should face downwards when integrated into the apparatus to let the air flow through the substrate first and then through the diffusion barrier layer. A metal jacket is mounted over the sample and over- pressure of about 2 bars is generated inside it. There is atmospheric pressure of approximately 1 bar under the sample . Now a constant volume flow would be discharged under the sample because of the pressure difference. A computer programme records the pressure drop and volume flow. This is automatically repeated for different given volume flows with the help of software. Denser the layer is larger the pressure drop measured across the sample. With the recorded data, the permeability coefficient for the sample can be determined by means of linear regression according to DIN ISO 4022. Permeability itself is given by Darcy's law:

$$\alpha = \frac{e \times Q \times \eta}{\Delta p \times A} \tag{5.12}$$

Where,

e= the flow-through thickness of the sample [m],

Q= is volume flow under the sample [m^3/s],

η= dynamic viscosity of the test fluid [mbar s],

Δp= pressure difference across the sample [mbar]

A= the flow-through area of sample [m^2].

6. RESULT AND DISCUSSION

The objective of this work was to investigate the redox cycle effects on the anode and electrolyte of the solid oxide fuel cells. The leak rate and the permeability behaviours of SOFC nodes and electrolytes, which were performed under the redox cycle atmosphere in the furnace at high temperature, would help understanding the electrochemical performance of the cells. This section focused on the obtained results which were categorized in two parts; results obtained from electrochemical test bench and results obtained from the leak rate and permeability measurements.

6.1 Electrochemical Results from Test Bench

The evaluation of the electrochemical tests was performed by Electrochemical Impedance Spectroscopy (EIS). EIS is instrument in order to understand the behaviour of not just one component, rather the interaction of all the components with one to another. The investigation gives an insight into phenomena such as the Triple Phase Boundary (TPB) and diffusion which occur between the porous layers of the SOFC. It is often that a single component, such as a single anode layer, might served well alone in an electrical characterization test; however, the same anode could behave exactly opposite when it interacts with the other components. The advantage of EIS is that a complete electrochemical system can be made from the impedance data. In this part of thesis, the anode and electrolyte materials were evaluated to determine their performance by applied EIS. One of the aims of this work was to measure the cell polarization resistances under the redox cycle. The total polarization is a collection of the activation polarization, diffusion polarization, and the ohmic polarization. For this reason, EIS determines identification of the loss mechanisms during operation. The polarization depends on the electrodes and electrolyte materials as well as microstructures and the operating temperature.

6.1.1 Electrochemical Results at Standard Conditions

In this work, in order to evaluate the performance of the SOFC cell, I-V curves were recorded at the activation phase (13 h) and 81 h, 112 h, 134 h operating hours for the standard conditions. The measurements were performed at standard conditions; 0.5 slpm H_2 and 0.5 slpm N_2 was feed to the anode and 2 slpm airs was feed to the cathode at a constant temperature of 800°C. The details about standard condition were displayed on the Figure 6.1. As well as, the overview of the long term period was given in the appendix 2.

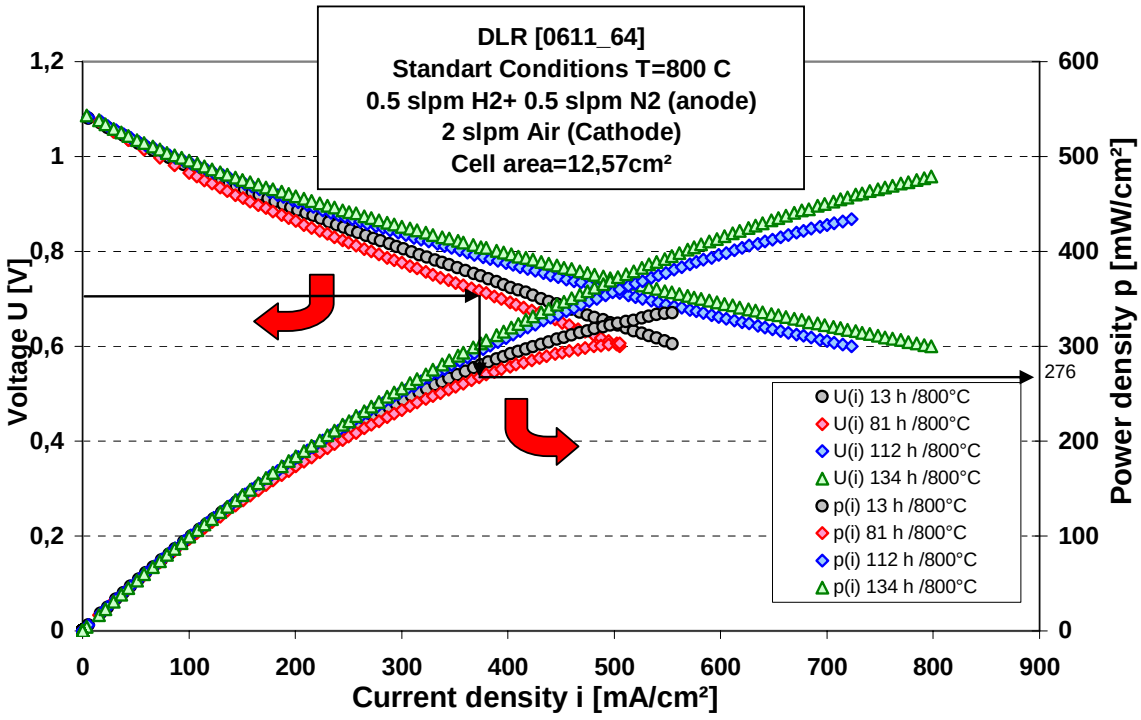

Figure 6.1 Cell voltage and power density vs. current density at standard conditions.

The decreasing curve symbolized the voltage which was against to the current density and the increasing curves symbolized the power density which was against to the current density. After activation period, the power density dropped suddenly; that was caused by the polarization of the cell. On the other hand, after some hours (nearly 100 h), the contact between platinum mesh and nickel metals were stronger by the effect of heat. This powerful contact was leaded by more conductive electrical path ways between the anode and platinum mesh. That was the reason of more efficient electron transportation. Indeed, the higher operating time provided higher

power density which could be explained by high quality of the connection between one component to another component and also the wires.

By comparing the power density between the cells, one fixed point was chosen and than the power density which was marked according to the value of this point, in this measurement the best point was at 0.7 V. In the Table 6.1, the power density values for the each measurement at the standard conditions were reported. As can be seen from Table 6.1, the decrement of the power density between the activation phase and 81 h was about 8,6 % due to the low polarization resistance of the cells. After 81 h, the measured power density at 0.7 V has shown an increment nearly 34% until 112 h and 47% until 134 h from 81 h. Although the activation phase let to decrease in the electrochemical properties of the cell at the earlier operation time, than later the electrical conductivity with platinum mesh and nickel element was improved under the high temperature. High degradation in the cell performance was prevented by the stronger electrical conductivity. Thus, the cell phenomenon was suddenly decreased and than increased in the cell performance during the operation. The Nyquist diagram was plotted at OCV on the Figure 6.2 and at a 200 mV/cm^2 loading on the Figure 6.3 after recording EIS data.

In the previous experiments, which were done in the DLR for the same project, the power densities gradually decreased from the beginning to the end of the cell life. Therefore, the highest power densities were revealed at the activation phase. However, the power densities in this study began to increase time to time after drastically drop. That was an unexpected situation before the experiment. The reason of this interesting increment was the difference of the substrate materials as well as, the formulation of the component materials and the size of the component materials.

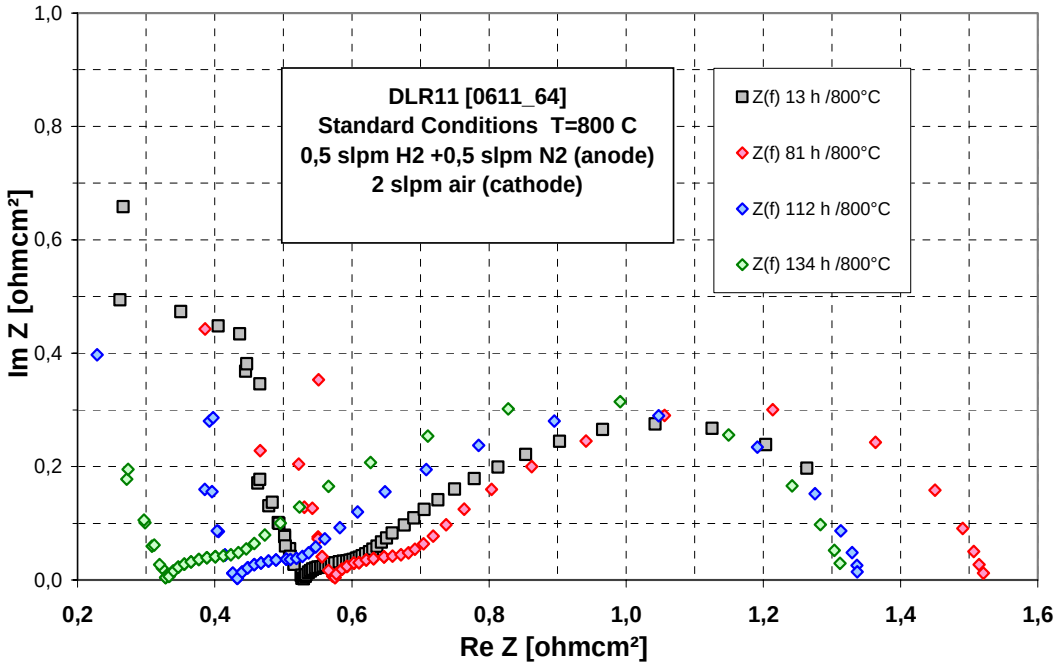

Figure 6.2 Nyquist diagram at OCV at standard conditions

The total resistance was the sum of the polarization (activation and diffusion) resistance and the ohmic resistance. Indeed the first semi-circle from the left symbolizes the activation polarization process while the second one at right symbolizes the diffusion process. It could be seen in the Figure 6.2, total polarization at 81 h has the biggest value; 1,52 ohmcm^2. Additionally, the lowest polarization has been occurred at the 134 h; 1,31 ohmcm^2. The ohmic and total polarization values are given in the Table 6.1. By this way, the total polarization and the ohmic resistance could be compared for the each measurement at standard conditions.

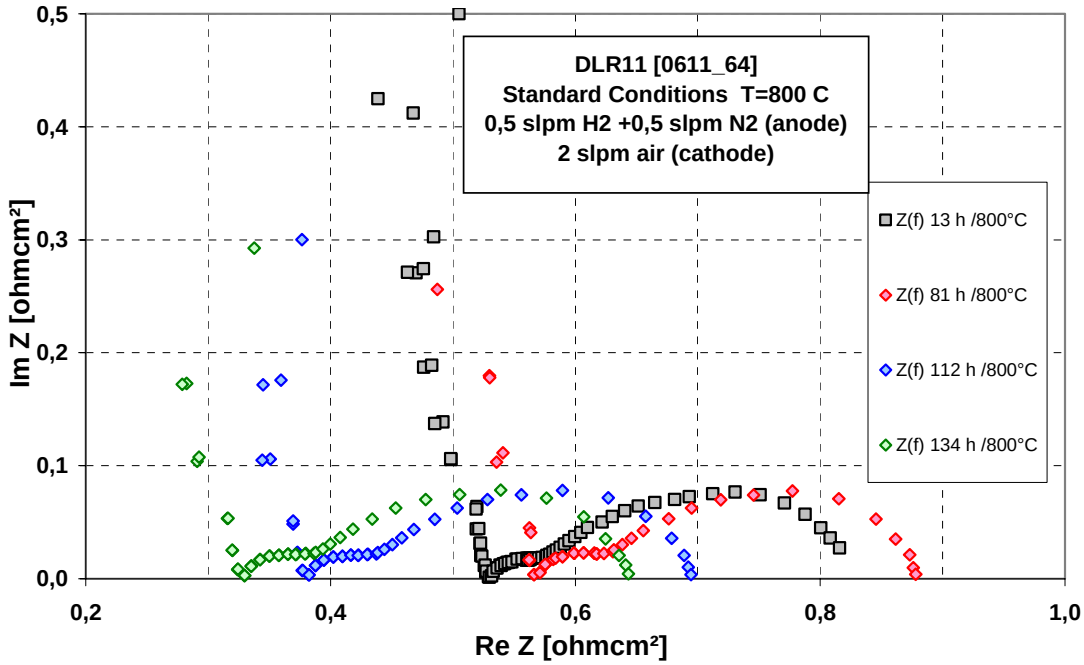

Figure 6.3 Nyquist diagram at 200 mV/cm^2 loaded

At 200 mV/cm^2 loaded conditions, the total resistance in the activation phase was 0,82 ohmcm^2. After early activation phase (until 81 h), higher losses were caused by the smaller TPB and the low surface ion exchange kinetics. The degradation of the cell performance was influenced from the change in microstructure and porosity of the cell. Afterwards, it was begun to increase due to the electrical conductive paths formation at high operation temperature. Therefore, ohmic and polarization resistance drastically turned to decrease, as can be seen in Figure 6.3 and Table 6.1.

When the unloaded measurement is compared with the loaded (200 mV/cm^2) measurement, ohmic polarizations were very closed in both diagrams. On the other hand, the total polarization in the unloaded measurement was higher than loaded measurement. A more precise way to verify this supposition was to make a simulation with the software Thales TM available at DLR, by fitting the impedance measurements recorded during experiments and the electrical equivalent circuit of a SOFC.

Table 6.1 The data at the Standard Conditions

Operation time[h]	Gas at the anode [slpm]	Gas at the kathode [slpm]	OCV [mV]	Power density at 0. 7 V [mW/cm²]	Rtotal OCV [mOhm.cm²]	Rohmic OCV [mOhm.cm²]	Rtotal 200 mA/cm² [mOhm.cm²]	Rohmic 200 mA/cm² [mOhm.cm²]
13.	0,5 H_2 + 0,5 N_2	2,0 Air	1091	302	1,37	0,53	0,83	0,53
81.	0,5 H_2 + 0,5 N_2	2,0 Air	1092	276	1,52	0,58	0,88	0,57
112.	0,5 H_2 + 0,5 N_2	2,0 Air	1093	369	1,36	0,41	0,69	0,38
134.	0,5 H_2 + 0,5 N_2	2,0 Air	1093	407	1,31	0,33	0,64	0,33

6.1.2 Electrochemical Results during the Gas Variation

Between 81 h and 93 h, the gas variation experiments were carried out under the different amount of H_2 and O_2 to the electrodes. The experiment conditions were given on the Table 6.2. The temperature had to be stabilized at 800°C in order to evaluate only the effects of fuel gas and the oxide gas. The results were displayed on the Figure 6.4.

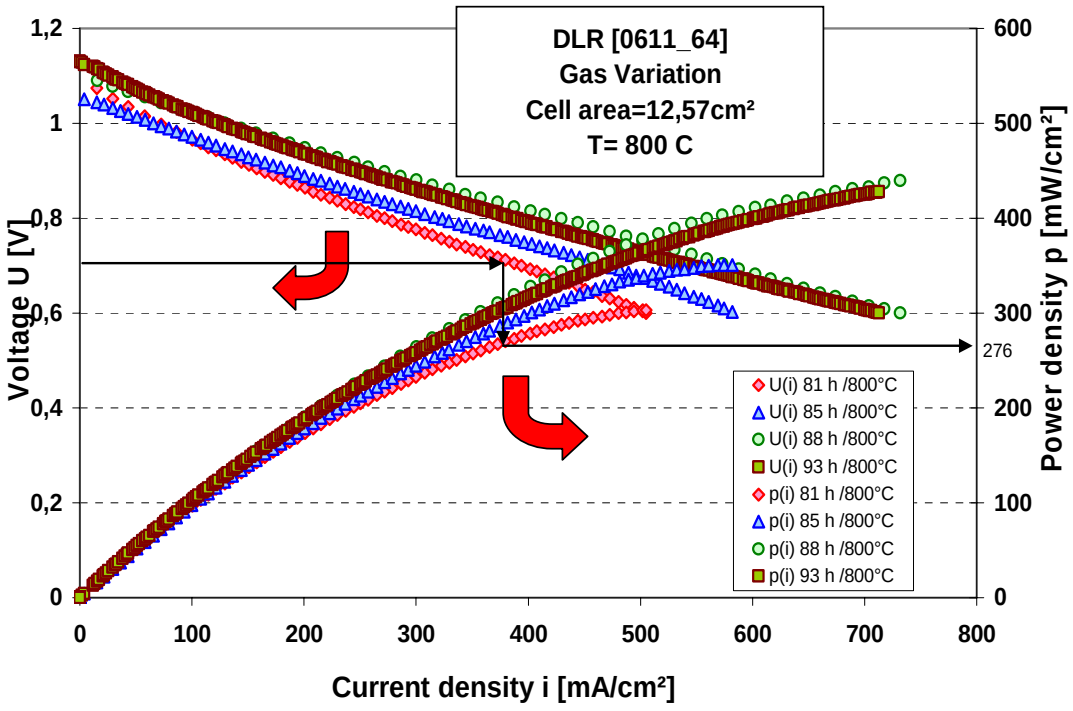

Figure 6.4 Cell voltage and power density vs. current density under different gas composition

As can be seen from Figure 6.4, the power density was minimum at the standard conditions. The cell performance changed due to variation of the gas. When higher amount of oxygen and hydrogen were supplied to the cathode, higher power density was recorded. At 88 h, the highest amounts of the hydrogen and oxygen gas were feed to the electrode and then the cell had the best performance. The ohmic and total resistances were shown on the Nyquist diagrams (Figure 6.5 and Figure 6.6). The power density at 0.7 V, OCV, ohmic and total resistance as well as the gas variation for the each measurement could be seen in the Table 6.2. This Table is a good way to show all the parameters and results together, so it makes clear not only comparing,

but also explaining the results. On the Nyquist diagram only such curves were plotted in order to display the polarization and ohmic resistance values apparently. In addition, the gas variation experiments for different O_2 and H_2 amounts were performed between 169 h and 191 h; the details were exhibited in the appendix 2.

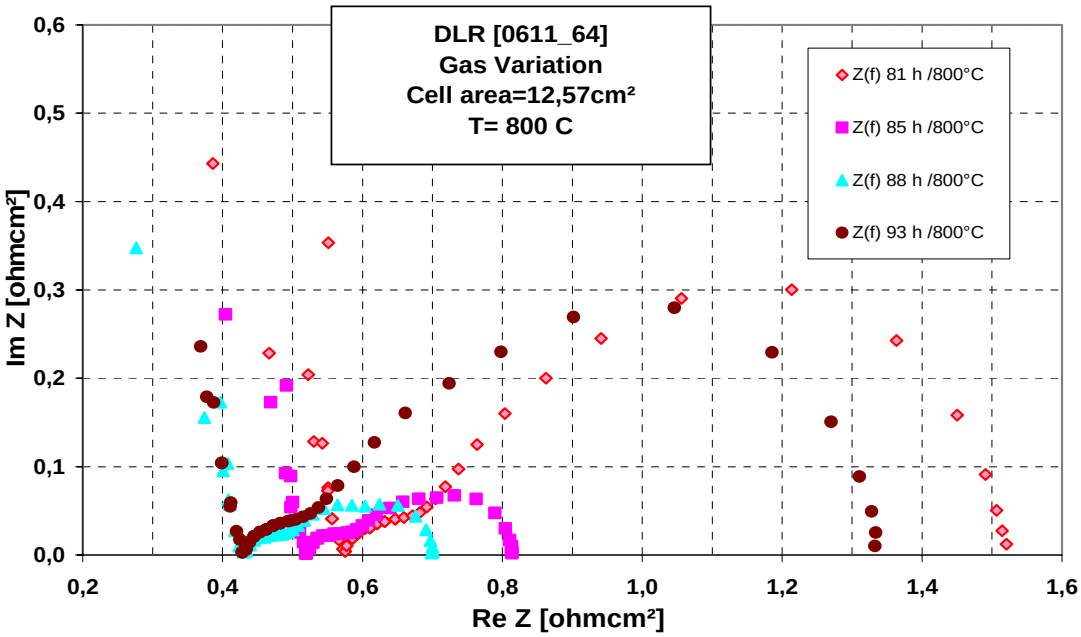

Figure 6.5 Nyquist diagram plotted during the gas variation without any loading

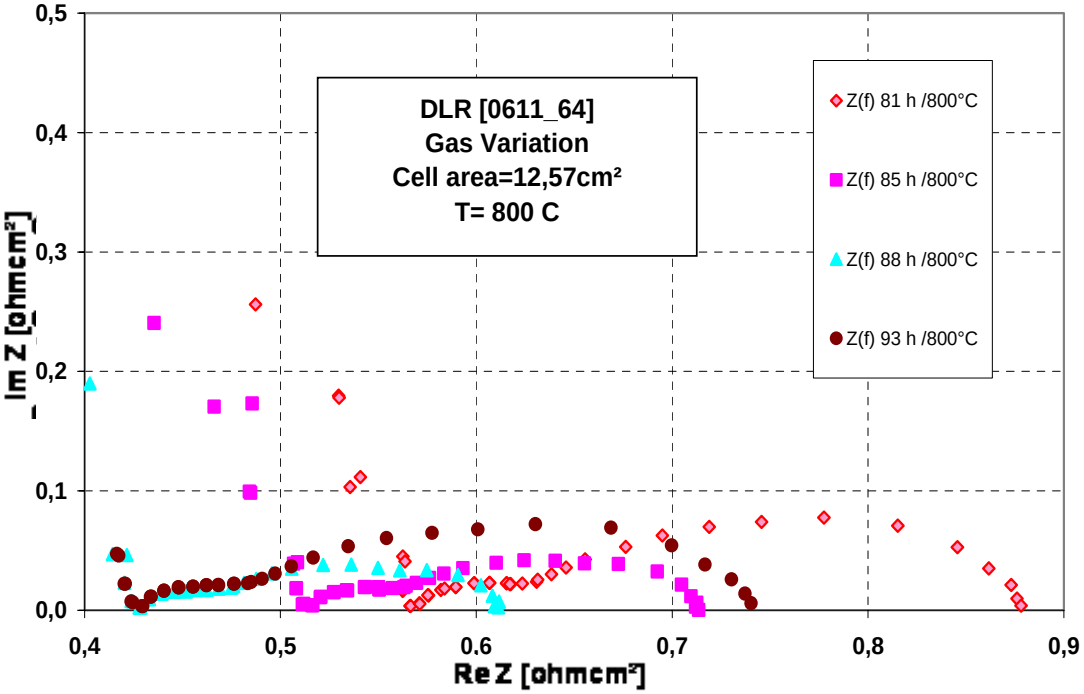

Figure 6.6 Nyquist diagram plotted during the gas variation at 200 mV/cm² loaded

The ohmic resistance which was measured at the first intersection with the X-axis at 88 and 93 hours, was almost the same on the both Nyquist diagrams with and without loading. The diffusion polarization was different for each curve in the loss mechanism. The main reason of this change should be gas variation effects to the anode and cathode. For instance, resistance of electrodes for the gas transportation and diffusion were decreased during the replacement of ions through the electrolyte while supplying the highest amount of the fuel and oxidant at the 88 h. For this reason, higher concentration provided to sufficient reactants transportation to the TPB. The high concentration was caused an increment in partial pressure of reactants at the TPB, as well as this increment directly affected the current which was taken from the TPB. Additionally, hydrogen at the anode side had a high diffusivity than the oxygen at the cathode side because of its lower molecular weight. For this case, the diffusion polarization at the anode side was lower than the cathode side. If the partial pressure of the oxygen was reduced during the constant partial pressure of the hydrogen, the OCV value increased due to high voltage difference between hydrogen and oxygen. Therefore, the change in partial pressure of the oxygen resulted in the differences of OCV (Table 6.2).

Table 6.2 The Data about the measurement of Gas Variation

Operation time[h]	Gas at the anode [slpm]	Gas at the kathode [slpm]	OCV [mV]	Power density at 0. 7 V [mW/cm²]	Rtotal OCV [mOhm.cm²]	Rohmic OCV [mOhm.cm²]	Rtotal 200 mA/cm² [mOhm.cm²]	Rohmic 200 mA/cm² [mOhm.cm²]
81.	0,5 H_2 + 0,5 N_2	2,0 Air	1092	276	1,52	0,58	0,88	0,57
85.	0,5 H_2 + 0,5 N_2	2,0 O_2	1056	329	0,81	0,52	0,71	0,51
88.	***1,0 H_2***	***2,0 O_2***	***1096***	***404***	***0,69***	***0,43***	***0,62***	***0,43***
93.	1,0 H_2	2,0 Air	1137	380	1,33	0,43	0,74	0,43

Otherwise, it could be possible to measure the effect of the change in the amount of the fuel gas. The gas variation was exposed to only anode side by decreasing the amount of hydrogen to half in the each measurement. At the beginning of the operation, the ratio of the hydrogen was 50% in N_2 and then decreased until 0,0625% (Table 6.3). The temperature was constant at 800°C in order to evaluate only the effect of fuel gas at the anode side. The data obtained from gas variation experiments were displayed on the Figure 6.7.

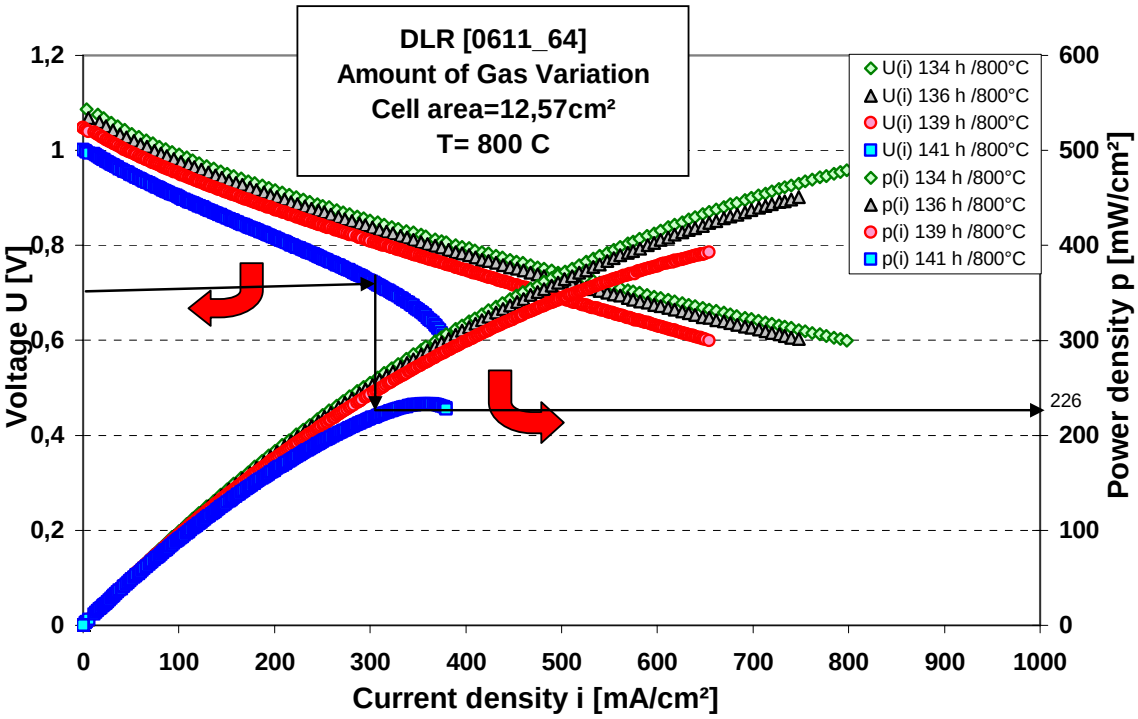

Figure 6.7 Cell voltage and Power density vs. current density with amount of gas variation

As can be seen in Figure 6.7, the power density did not show a dramatically change between 134, 136 and 139 hours due to the fuel gas variation to the anode side. However, at 141 h, the cell performance has decreased immediately due to the lower amount of the hydrogen. All the power density values at 0.7 V were revealed at the Table 6.3

Additionally, the OCV values at 134 h and at 141 h were recorded as 1093 V and 1002 V, respectively. The drop in OCV was nearly 8.3%. This result proved that; the degradation in the hydrogen supply obviously affected the cell performance, because the sufficient fuel gas could not be reached to the TPB. Both Nyquist diagrams were displayed in the Figure 6.8 and Figure 6.9.

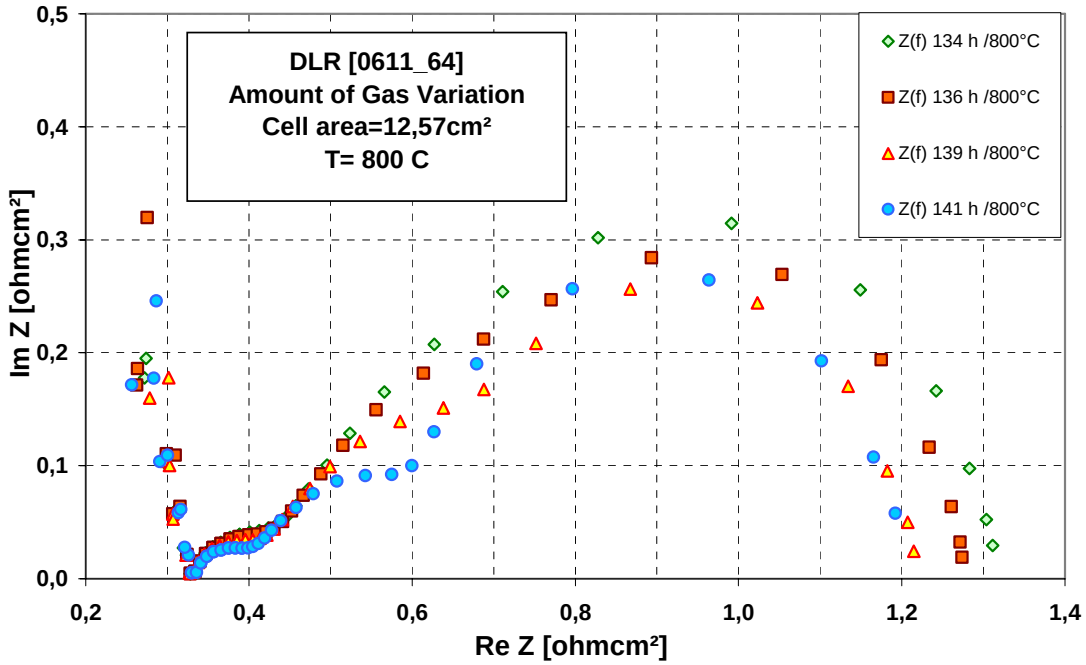

Figure 6.8 Nyquist diagram plotted during the gas variation without any loading

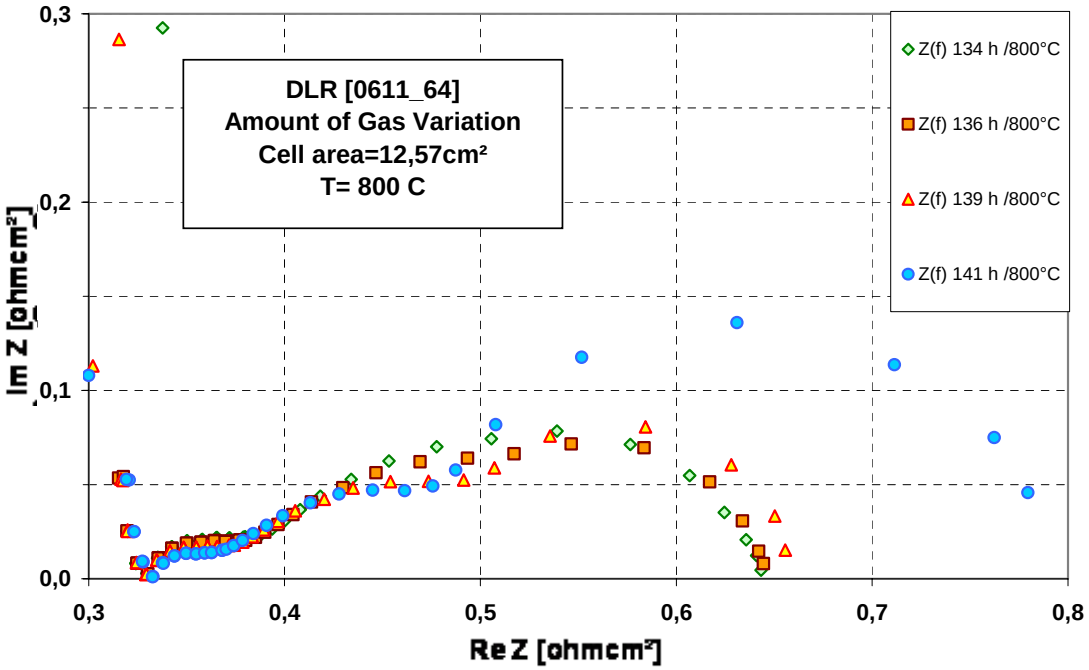

Figure 6.9 Nyquist diagram plotted during the gas variation at 200 mV/cm² loaded

The ohmic resistances for all cycles were nearly same in both diagrams. Although the total resistances were stabilized at different points, there was no significant change in the ohmic resistances. Actually, the total resistance was the sum of the polarization (activation, diffusion) resistance as well as the ohmic resistance. From

the view of this point, the polarization resistance was responsible from the degradation in the cell performance.

On the other side, the considerable change in the furnace temperature was existed; it depended on the amount of hydrogen flow. The inside furnace temperature was decreased during the degradation of the hydrogen partial pressure independently from the furnace temperature control. Therefore, the furnace temperature from the control system was increased to assure a sTable cell temperature at 800 ºC. Thus, it could be suspected that a direct exothermal combustion of H_2 occurred in the furnace due to cell leakages increasing the measured cell temperature. Indeed, the H_2 concentration is smaller at the cathode side than at the anode side, which can induce H_2 diffusion process between these both functional layers in spite of the fact that the electrolyte has relatively good gas tightness. Another better explanation for these leakages could be the instability of the glass paste during operation. As well as, the details about the operation were revealed at Table 6.3 for the discussion of the cell behaviour due to the fuel gas variation.

Table 6.3 The data about the measurement of amount of gas variation

Operation time	Gas at the anode [slpm]	Gas at the kathode [slpm]	OCV [mV]	Furnace Temp. [ºC]	Cell Temp. [ºC]	Power density at 0. 7 V [mW/cm²]	Rtotal OCV [mOhm.cm²]	Rohmic OCV [mOhm.cm²]	Rtotal 200 mA/cm² [mOhm.cm²]	Rohmic 200 mA/cm² [mOhm.cm²]
134h	$0{,}5H_2$ +$0{,}5N_2$	2,0 Air	1093	782	800.8	407	1,31	0,33	0,64	0,33
136h	$0{,}25H_2$+$0{,}25N_2$	2,0 Air	1077	784	801.0	383	1,27	0,33	0,65	0,33
139h	$0{,}125H_2$+$0{,}125N_2$	2,0 Air	1048	785	801.1	336	1,22	0,33	0,66	0,33
141h	$0{,}0625H_2$+$0{,}0625N_2$	2,0 Air	1002	786	801.2	226	1,18	0,33	0,78	0,33

6.1.3 Electrochemical Results during the Temperature Variation

The experiments of the temperature variation were carried out successively between 850°C and 700°C with a standard gas supply of 0.5 slpm H_2 + 0.5 slpm N_2 at the anode and 2 slpm air at the cathode. It has taken many hours to reach and stabilize the selected cell temperature in the experiment. The I-V recordings (Figure 6.10) were performed at 112, 116, 121 and 123 h. when the temperature were stabilized at 800°C 850°C 700°C and 750°C, respectively. Furthermore, the temperature variations allow calculating the activation energy of the electrode reactions and the ionic conduction in the electrolyte layer.

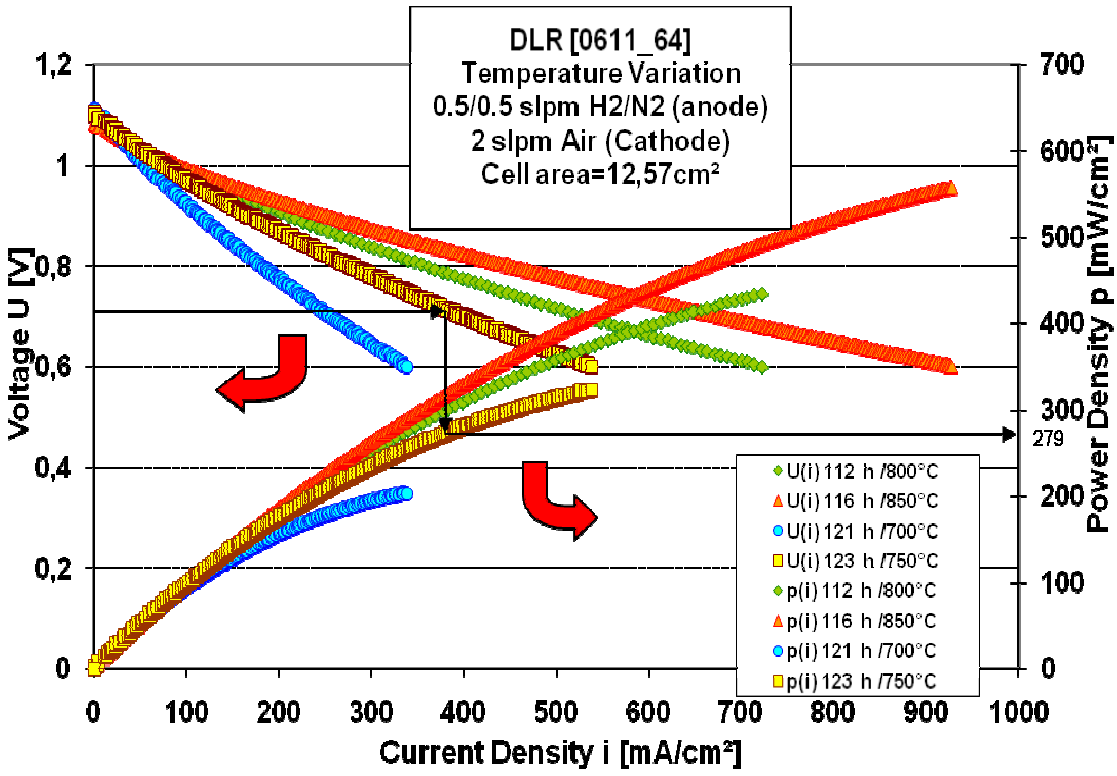

Figure 6.10 Cell voltage and power density vs. current density with temperature variation

First of all, the cell performance was better at higher temperatures. During the temperature variation between 700°C and 850°C at 0.7 V loading, the power density increased by 163 % from 179 mW/cm^2 to 472 mW/cm^2. Some of the detailed data about the temperature variation measurement was given in the Table 6.4.

Table 6.4 The data about the measurement of temperature variation

Operation time	Gas at the anode [slpm]	Gas at the kathode [slpm]	Cell Temp. [°C]	OCV [mV]	Power density at 0. 7 V [mW/cm²]	Rtotal OCV [mΩ.cm²]	Rohmic OCV [mΩ.cm²]	Rtotal 200 mA/cm² [mΩ.cm²]	Rohmic 200 mA/cm² [mΩ.cm²]
112h	0,5 H_2 + 0,5 N_2	2,0 Air	800	1093	369	1,34	0,43	0,70	0,38
116h	0,5 H_2 + 0,5 N_2	2,0 Air	850	1083	472	1,18	0,31	0,59	0,31
121h	0,5 H_2 + 0,5 N_2	2,0 Air	700	1109	179	2,16	0,78	1,32	0,79
123h	0,5 H_2 + 0,5 N_2	2,0 Air	750	1101	279	1,59	0,52	0,90	0,51

The open cell voltage had the highest value (1109 mV) in the 121 h at 700 ºC and the lowest OCV value (1083 mV) was in the 116 h at 850 ºC. That's the reason of the change in OCV is that increment in the temperature caused to decrease in Gibbs free energy (ΔG). The Gibbs free energy relation with the Nernst equation could explain the degradation of the OCV by increasing the temperature. In this respect, polarization and ohmic resistances were lower at high temperature and the power density was higher. In order to define the relation between the cell behaviour with the temperature, it was necessary to observe the Nyquist diagrams. These diagrams were displayed on the Figure 6.11 and Figure 6.12.

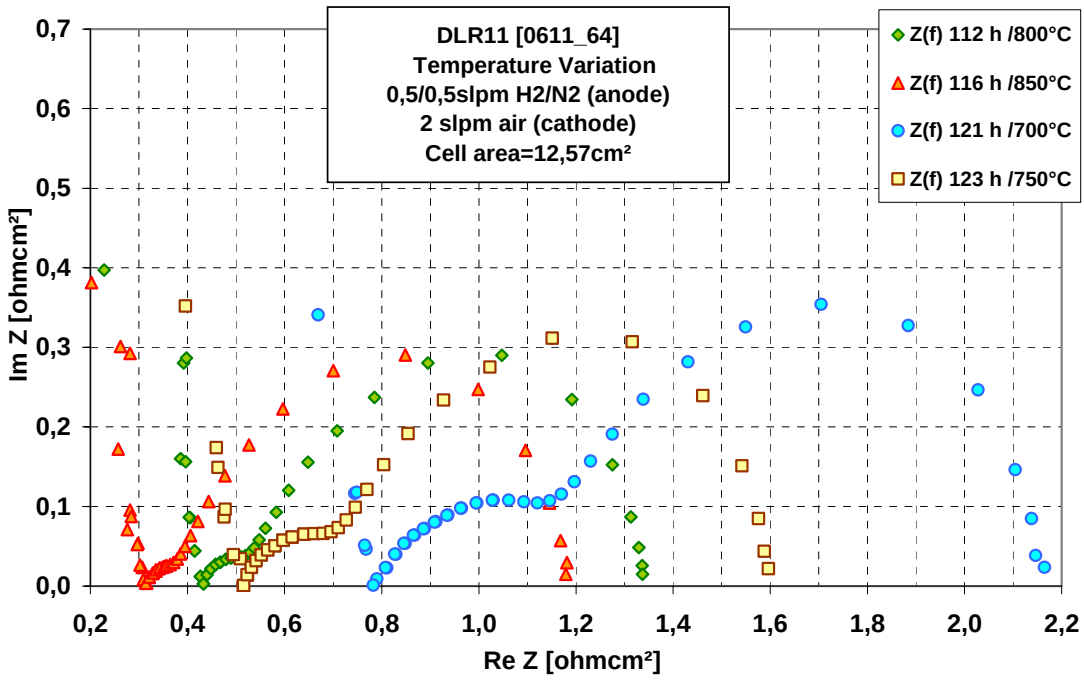

Figure 6.11 Nyquist diagram plotted during the temperature variation without any loading

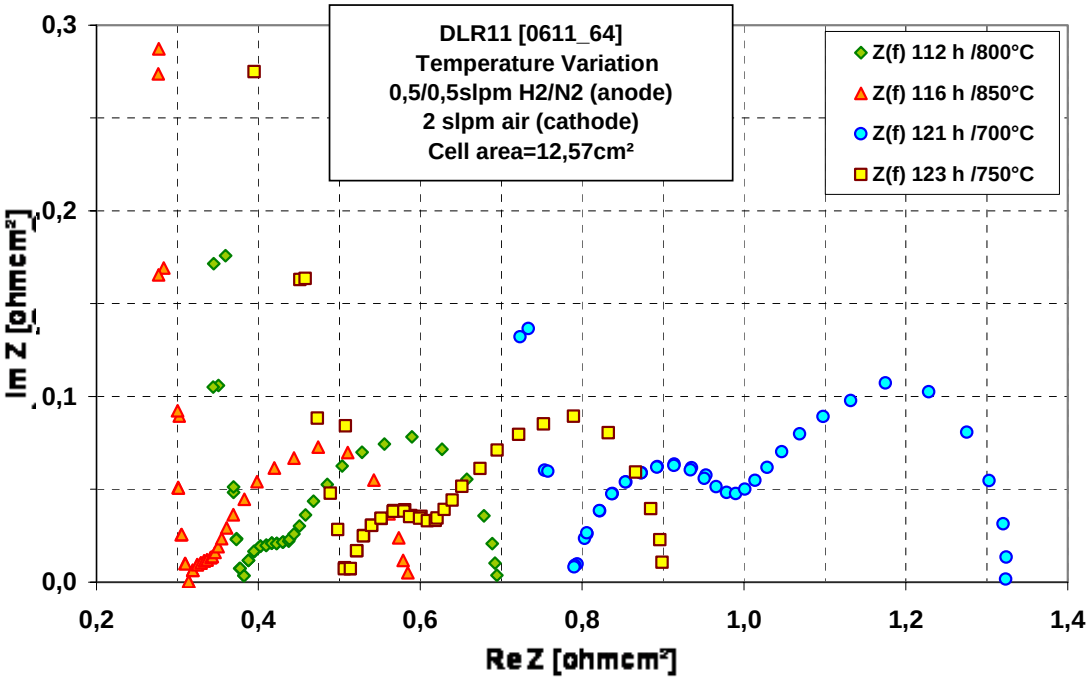

Figure 6.12 Nyquist diagram plotted during the temperature variation at 200 mV/cm² loaded

As can be seen in both graphs, at 700 ºC had the biggest value of the ohmic and total resistance, as well as, the values of the ohmic and total polarization at 850 ºC were the lowest value. Additionally, the temperature variation experiments were performed again at 300-327 operation hours. The power density, OCV value from the I-V curve, voltage losses value from the Nyquist diagram for loaded and unloaded were given in the appendix 2. As can be observed, the results and comments were nearly same with the measurement between 112 h and 123 h. However, these two measurements' values were useful to investigate the activation energy change due to the long operation time. That was calculated by the Arrhenius equation. Thus, it makes possible to define the activation energy which was required to start the reactions.

The temperature dependency of resistance could be described in terms of the activation energy for resistivity, *Ea*, using the Arrhenius equation:

$$Rpol = Ro \exp(\frac{Ea}{Rm}.\frac{1}{T}) \qquad (6.1)$$

Where;

R_{pol} = Total polarization resistanance (mΩcm^2)

R_0 = Resistance pre-exponential factor,

Ea = Activation energy (J/mol),

Rm = Universal gas constant (8,314 J/mol·K),

T = Temperature (K)

Taking the logarithm of equation 6.1, the following linear equation (6.2) can be obtained.

$$\ln(Rpol) = \frac{Ea}{Rm}.\frac{1}{T} + \ln(Ro) \tag{6.2}$$

The Arrhenius plot was used to determine the activation energy, (Ea). It showed that the polarization resistance of the cells was linear function and temperature dependent. The activation polarization could avoid reducing the energy barrier of the rate-determining step of the reaction to a value such that the electrode reaction proceeds at a desired rate. The electrode reaction rate is a function of the temperature, pressure, and the electrode material. Such as, the reaction rate is faster at high temperatures, thus the activation energy is usually smaller [23].

Figure 6.13 was plotted to acquire the activation energy of the cell at two different operation periods. The y-axis was the logarithm of the polarization resistance at OCV in ($m\Omega cm^2$) and the x-axis was the reciprocal of the temperature in 1/K.

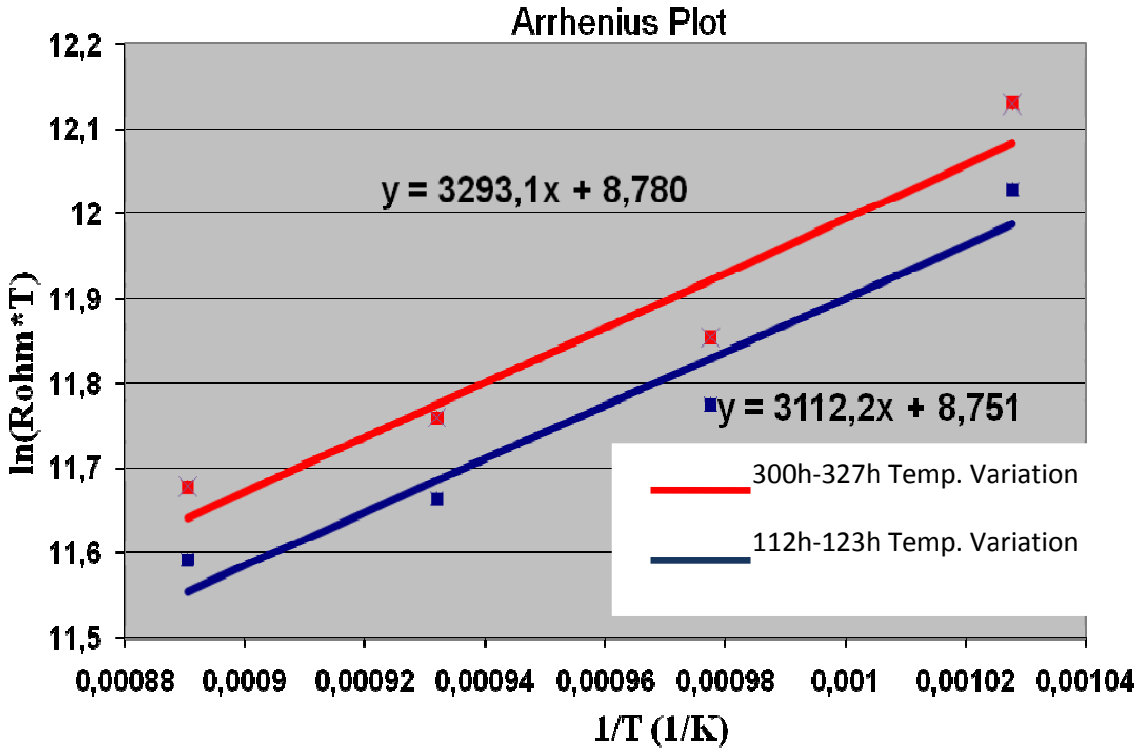

Figure 6.13 The activation energy of the two different operation periods of the cell

This curve was plotted to define the activation energy of the cells for two operation period. At the short term period (between 112-123 operating hours), the absolute value of the slope was 3112,2, thus the value of the activation energy was 25.874 $kJ.mol^{-1}$. For the long term period (between 300-327 operating hours), the absolute value of the slope was 3293,1, thus the value of the activation energy was nearly 27.380 $kJ.mol^{-1}$. The activation energy of the short term was 6 % lower than the long term period. This means the cell required less energy to occur electrochemical reactions during the short-term period than the long term period. In conclusion, the three phase boundary had an unextensive surface behaviour due to the sintering of NiO particles and high porosity in the combination with the YSZ molecules, while running the long term. However, the amount of change in the activation energy in the long term period could not make any sense when compared with the activation change which was done in previous master thesis in this project. The reason of this less change is that nanostructured particles were used in this experiment [12, 54].

6.1.4 Scanning Electron Microscopy

The cell was fractured by hand-craftig after and before electrochemical operation in order to conserve the precise form of the materials and the microstructure of the cell. Figure 6.14 and 6.15 showed the three functional layers of the cell and the substrate. It could be observed with a magnification of 200. First micrograph was taken after thermal spray process and the second micrograph was taken after the electrochemical tests.

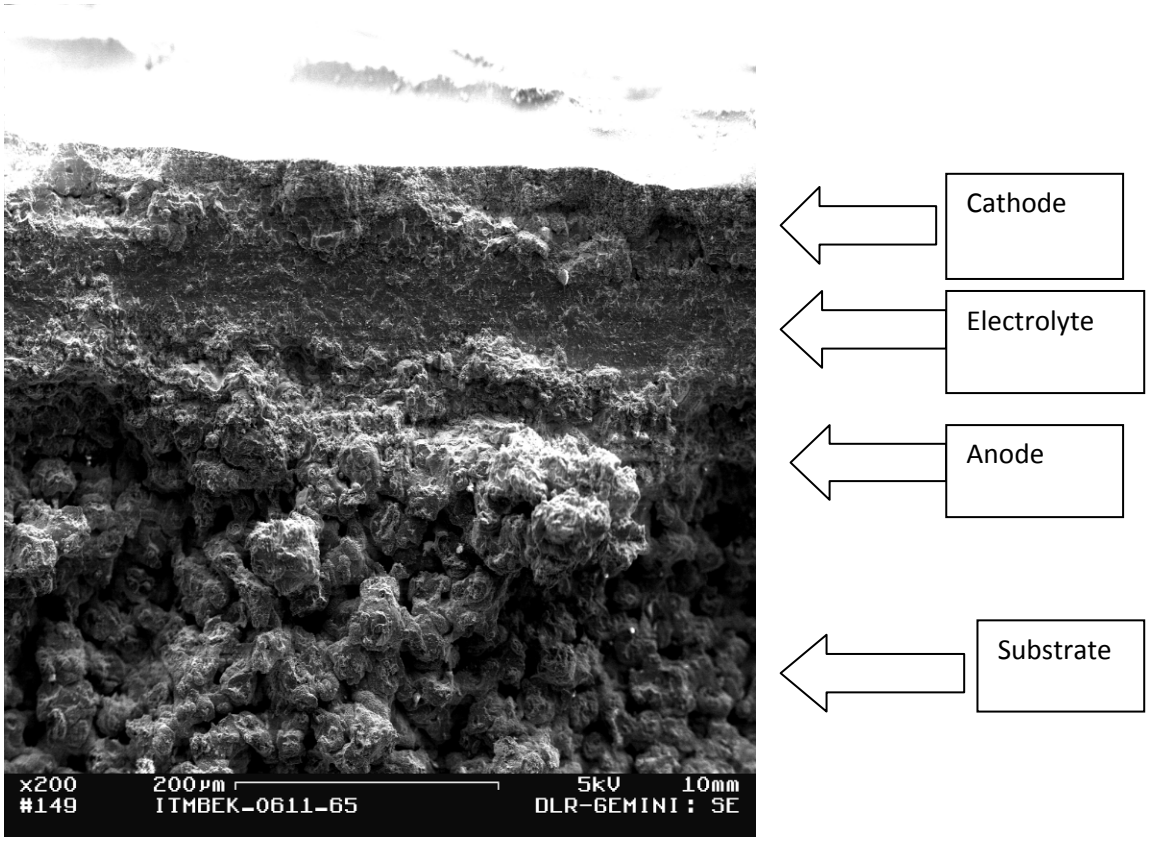

Figure 6.14 The SEM micrograph of the cell after plasma sprayed

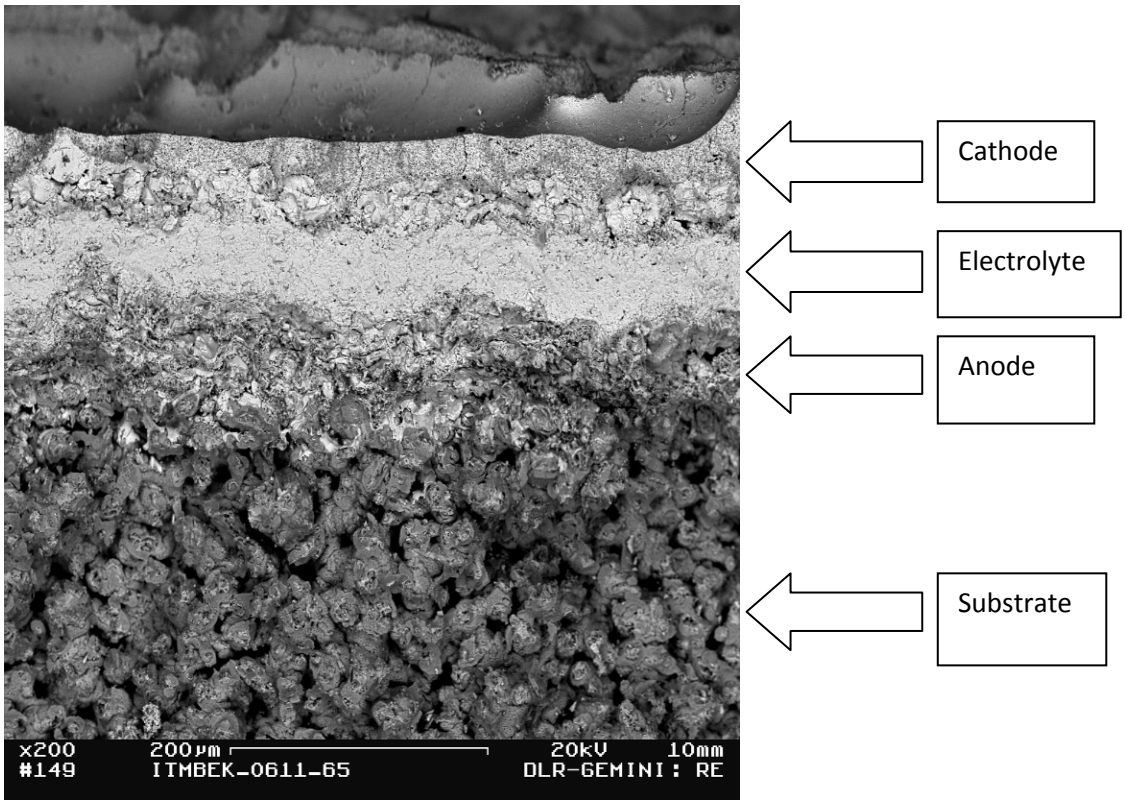

Figure 6.15 The SEM micrograph after electrochemical analyze

The electrochemical effects on the cell could be seen in the Figure 6.14 and Figure 6.15 obviously. The significant difference was the pore size. The pore size of the cell after electrochemical analyse was bigger than sprayed cell pores. The porous structure was extended by the effect of the redox cycle at the beginning of the electrochemical analyse which was explained at the section 4 in this thesis. As well as, the substrate had a very high porosity due to big ferritic particles. Actually, substrate materials and anode base material (Nickel) had similar behaviour under redox atmosphere, that's the reason of the expansion in the porous structure. On the other hand, the thicknesses of the layers were exhibited in the Figure 6.16.

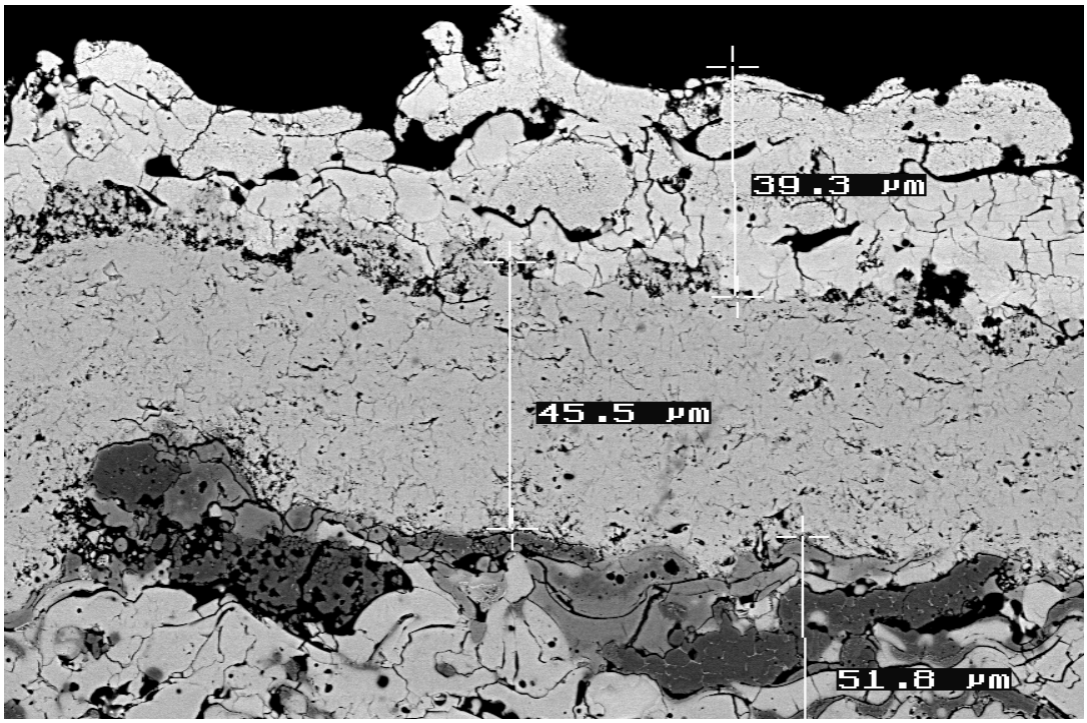

Figure 6.16 SEM micrograph of the cell cross section after the thermal spray process

The thicknesses of each components of the cell were measured after the thermal spray process. The anode thickness was measured as 51,8 µm, which was estimated to be <55 µm, and the electrolyte thickness was measured as 45,5 µm, which was estimated to be <50 µm as well as, the cathode size, was 39,3 µm, which was estimated to be ~40 µm. All the estimations were exhibited in the section of 5.1. SEM provided to observe the functional layers with magnification evidently. Therefore, the components of the cell respectively 1500 times magnified in the next Figures.

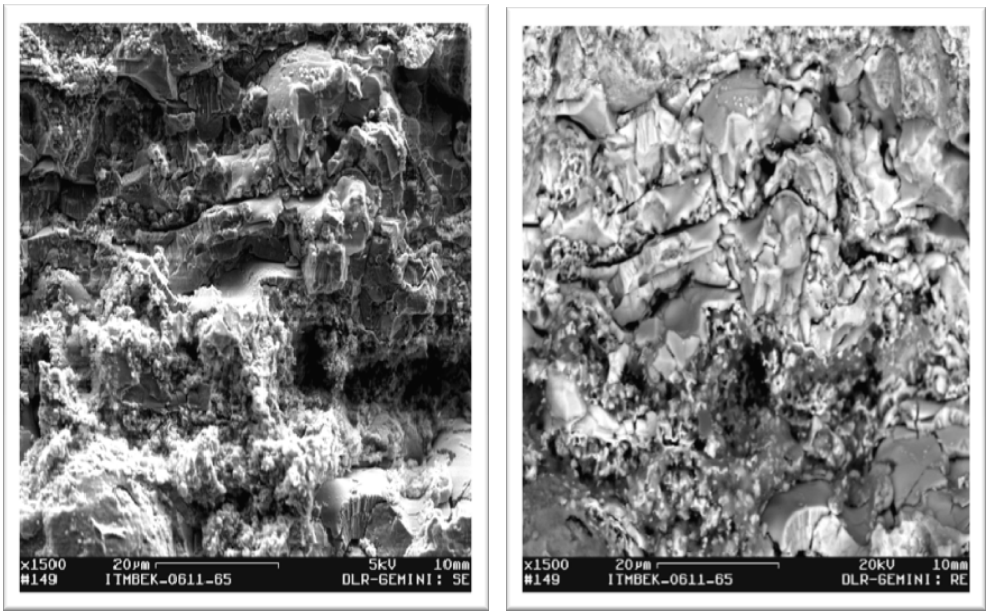

Figure 6.17 The SEM micrographs of anode after (a) sprayed and after (b) electrochemical tests

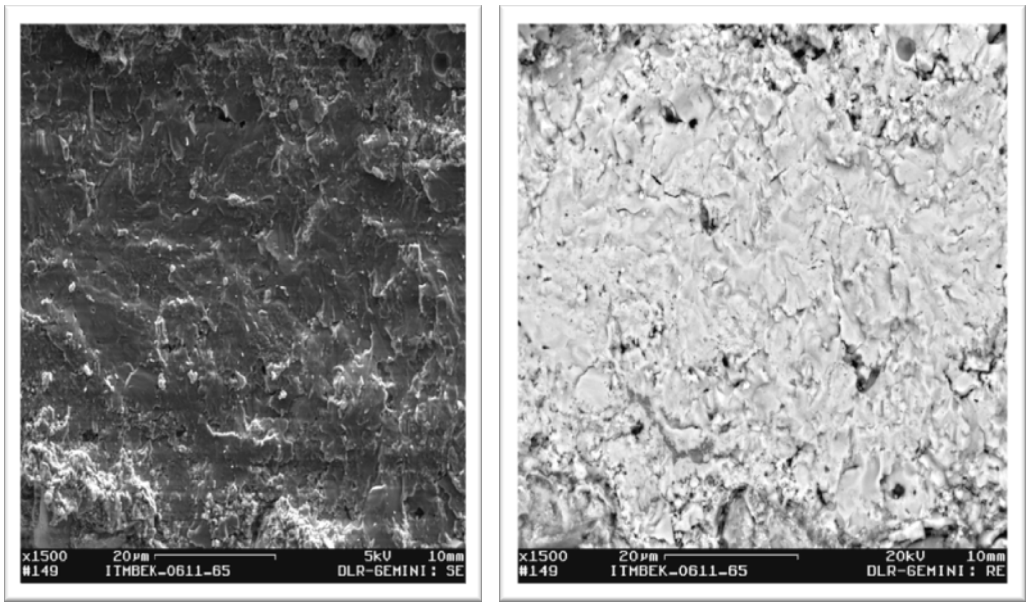

Figure 6.18 The SEM micrographs of electrolyte after (a) sprayed and after (b) electrochemical tests

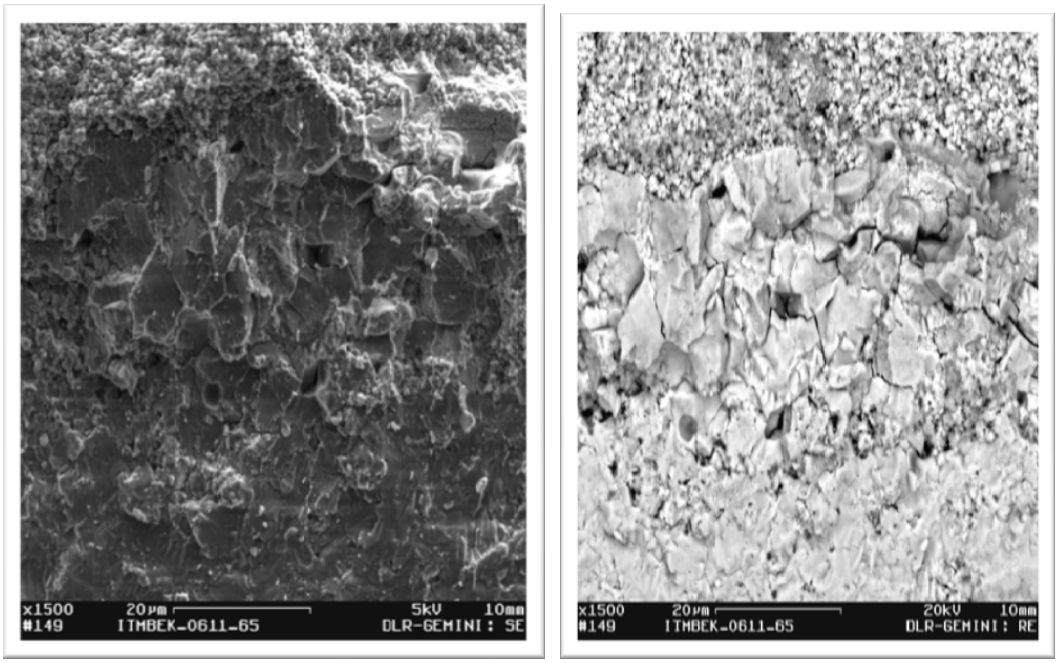

Figure 6.19 The SEM micrographs of cathode after (a) sprayed and after (b) electrochemical tests

At the Figure 6.16, the electrolyte-anode surface adherence seemed to be strong; therefore the three phase boundary provided to occur the reaction efficiently. The next three Figures (6.17, 6.18, 6.19) were showed the effects of electrochemical analyse. As can be seen from the Figure 6.17, Ni particles was sintered and assured to a better accommodation for the porosity with a foamy texture in anode. It is seen from Figure 6.18, the delaminations and crackings were occurred in the electrolyte after long term operation. Finally, the cathode (Figure 6.19) seemed to have an efficient gas diffusion property through the high poros structure of the cell. Pore size became bigger after the electrochemical analyse.

6.2 Redox Cycle in the Furnace

Redox cycling was basically oxidation and reduction of the metallic content of the anode and substrate. During the oxidation, nickel in the anode structure would be oxidized to NiO by feeding air to the system, resulting in an expansion on particle size. When hydrogen was feed to the system, NiO was reduced back to Ni, which would be a size reduction of the particle. The functional layers should have to be flexible to this particle size change during redox process which would be happening several times during operation in reality. In this work, one redox cycle has been

occured in two separate phases. Oxidation was acquired by the flow of the air as well as, reduction was acquired by Ar+5%H_2 flow to the furnace, while keeping the temperature 800 ºC. The permeability test was performed for the substrate and the sprayed anode, besides that the leak rate test was performed with the half cell (sprayed anode and electrolyte on the substrate)

6.2.1. Leak Rate Measurement

In order to measure the gas tightness of the electrolyte, a gas leakage test was carried out at DLR before the electrochemical analyse of the cell. As explained in the experimental part, the recorded pressure was plotted against the time, was shown in the Figure 6.20. Thus, the gas leakage rate against the pressure was displayed in the Figure 6.21. The number of the cell 0704_03 was chosen as an example measurement, which was applied after thermal plasma spray process.

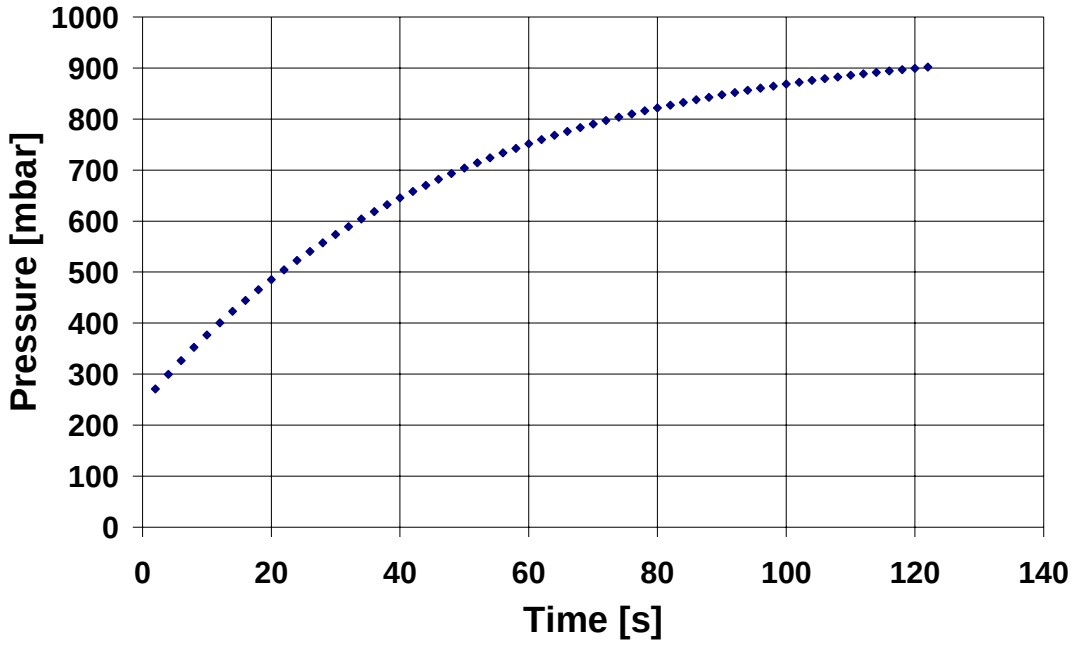

Figure 6.20 The relationship between pressure and time

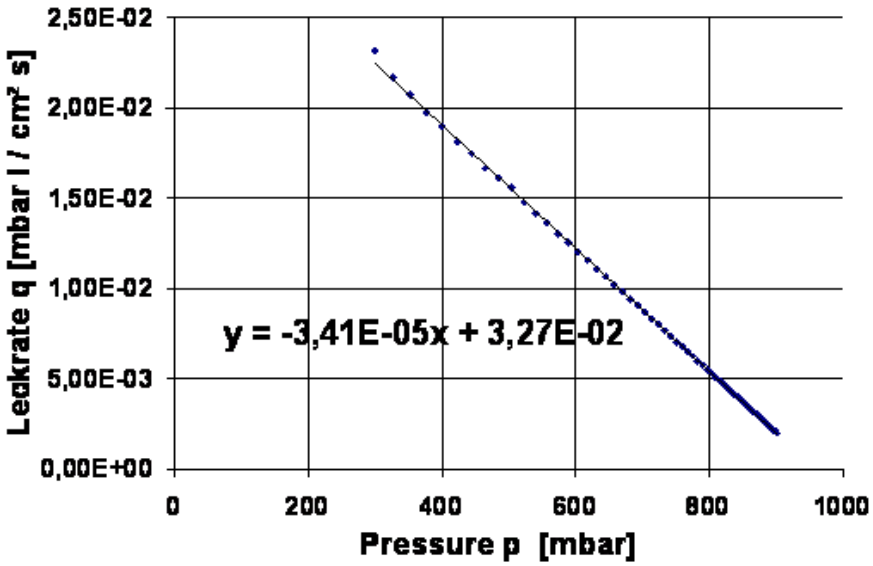

Figure 6.21 The relationship between leak rate and pressure

In SOFC operating conditions maximum 100 mbar of pressure difference was expected between the both sides of the cell. Therefore, the absolute leak rate should be estimated at the point where there were 100 mbar differences. The leakage measurement was performed at room temperature; therefore the values were not the real leak value during operation. However, it could give an idea about the leak tendency of the samples. The procedure was like that; first, the sprayed samples were leak tested; and than redox cycle has applied to the sprayed cells; at last, the redox cycled cells were leak tested. The medium, which was used for measurements, was nitrogen. All the measurements were performed at room temperature and corresponded to pressure of 900 mbar in vacuum chamber. Table 6.5 showed the results obtained from these measurements. Two samples were used to provide the precise result inside each run. It was obvious that the samples having higher amount of the electrolyte mass (provides greater thickness) were more leak tight than the one with less amount of electrolyte mass.

Table 6.5 The identification data for the sample used in leak rate measurement

Run	Scope of Run	Cell Name	Weight of Substrates(g)	Weight of Anode(g)	Weight of Electrolyte(g)	Leak Rate (mbarlt/Scm^2)
1. Run	1 Reduction	0611_38	7,402	0,4254	0,4186	4,77E-03
		0611_39	7,5905	0,4281	0,4299	4,71E-03
2. Run	1 Reduction+1 Redox	0703_01	7,7562	0,4111	0,4114	5,12E-03
		0703_08	7,7737	0,445	0,3843	3,37E-03
3. Run	1 Reduction+5 Redox	0611_35	7,356	0,4504	0,4024	3,36E-03
		0611_36	7,3594	0,4468	0,4015	3,66E-03
4. Run	1 Reduction+10 Redox	0704_05	7,9884	0,4432	0,3961	3,78E-03
		0704_06	7,8589	0,4445	0,4077	3,67E-03
5. Run	1 Reduction+15 Redox	0704-03	7,645	0,407	0,4094	5,14E-03
		0704-04	7,5957	0,4506	0,4098	5,17E-03

After each run, the leak rates of the cells were measured, so the effects of the redox cycles on the half cells could be determined by leak rate differences. During the Nickel oxidation, the particle size of the NiO became bigger than Ni original particle size. Hence, the three phase boundary was damaged by the size expansion of the Ni particles. Moreover, cracking and delamination of the electrolyte was occurred by the effects of this enlargement. Figure 6.22 showed the leak rates comparison between sprayed cells and redox cycled cells at room temperature.

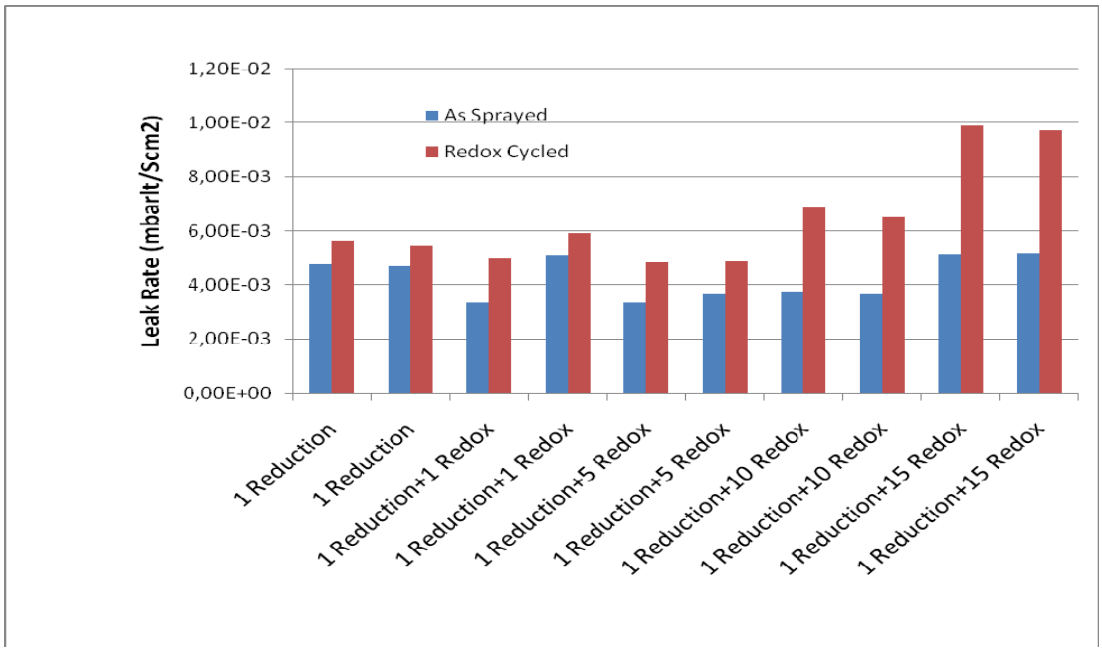

Figure 6.22 The leak rate comparisons with sprayed cells and redox cycled cells

The percentage difference was calculated by the equation (6.3) and the graph of the percentage difference was revealed in the Figure 6.23.

$$\%Difference = \frac{q_{l(sprayed)} - q_{l(redox)}}{q_{l(redox)}} \times 100 \qquad (6.3)$$

where q_l= leak rate (mbar lt/Scm^2).

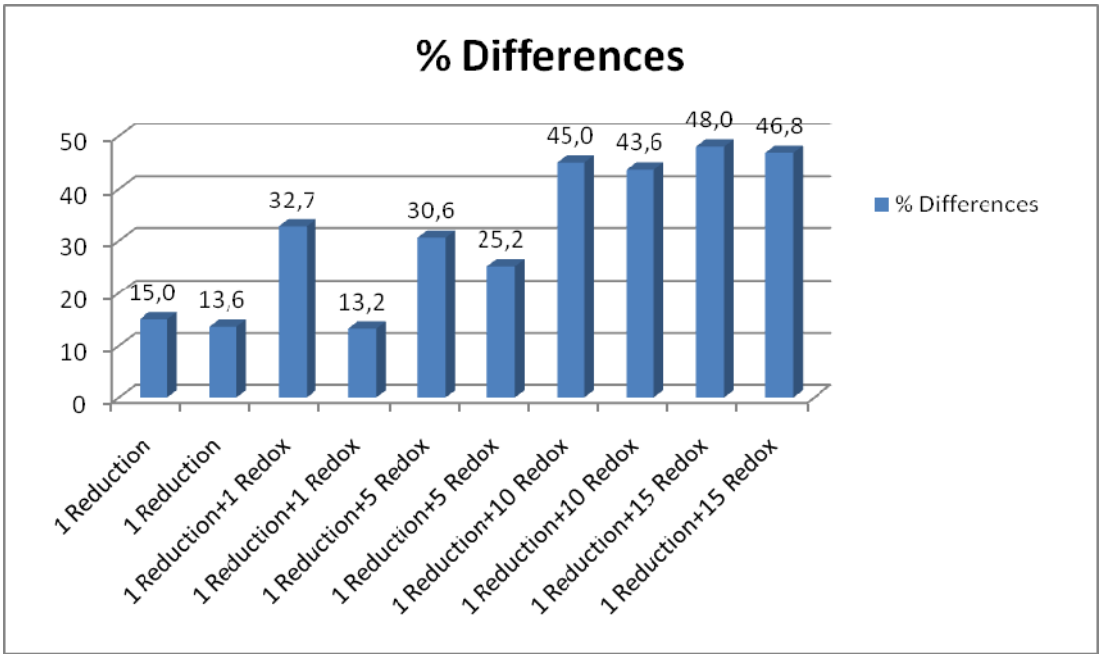

Figure 6.23 The percentage difference of leak rate between sprayed and redox cycled cells

Run 1 exhibited nearly 14% difference; on the other hand, the difference in Run 5 was nearly 47%. This wide range of variation was relatively existed by the number of redox cycle. These measurements concerned to define the formation of the cracks and delamination structure on the electrolyte under the redox athmosphere. At the first and the second runs, the effects of the reduction and redox cycle to the electrolyte were at low level due to the nanostructured Ni+YSZ anode layers which were fabricated by air plasma spray. The biggest change occurred after five redox cycles and it was expected before the experiment. The leak rate was increased, while the numbers of the redox cycles were increased. However, the change of leak rate could be ignored; it means that the electrolyte has not damaged very much from the redox cycles. Highly possible reason of this result; the volume change of the Nickel could not dramatically damage the three phase boundary because of the nanostructured Ni+YSZ anode layer. As well as, nanostructured Ni+YSZ anode layer provided strong three phase boundary.

6.2.2. Permeability Measurement

Permeability tests were also performed for the investigation of the cracking based on nano-structured NiO/YSZ anode layer. This layer was sprayed on the substrate by air plasma spray

technology like as the other components of the cell. The integration onto the substrate should be as much permeable as required from the anode side. The procedure of the permeability measurement was described in section 5.4.2. As explained in the experimental part, the recorded flow rate was plotted against the pressure difference. The permeability coefficient (alpha) could be calculated from the Figure 6.24. The number of the cell 0704_10 was chosen as an example, which was performed to the sprayed cells.

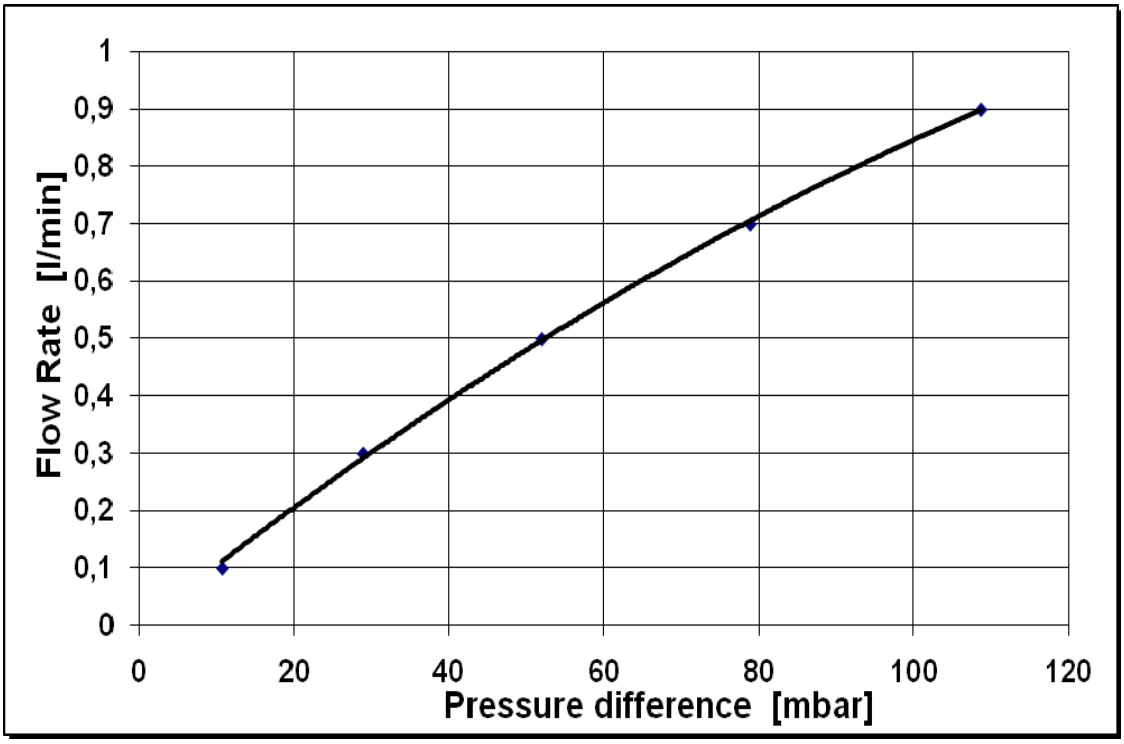

Figure 6.24 The relationship between flow rate and pressure difference

Generally, at permeability tests in DLR, maximum volume flow of 0.9 l/m and minimum volume flow of 0.2 l/m through the sample was controlled by the software when the pressure difference across the sample was 1 bar.

The permeability coefficients (alpha) and the weights of anodes and subsrates were given in the Table 6.6. The comparasion of the permeability coefficient could be seen in the Figure 6.25. In the Figure 6.26 could be seen the % difference to investigate the effects of the redox cycle in detail.

Table 6.6 The details for the sprayed cells which are used for permeability tests

Run	Scope of Run	Cell Name	Weight of Substrates (g)	Weight of Anode (g)	Permeability (m^2)
1. Run	1 Reduction	0611_22	7,8516	0,4428	2,62E-14
		0611_15	7,4617	0,4521	3,18E-14
2. Run	1 Reduction+1 Redox	0703_16	7,6464	0,4815	2,08E-14
		0703_15	7,6904	0,4918	2,11E-14
3. Run	1 Reduction+5 Redox	0611_98	7,0718	0,4892	1,72E-14
		06,11_99	7,1511	0,4972	1,88E-14
4. Run	1 Reduction+10 Redox	0704_09	7,7925	0,4592	2,75E-14
		0704_11	7,7672	0,4527	2,99E-14
5. Run	1 Reduction+15 Redox	0704_10	7,5467	0,492	2,64E-14
		0704_13	7,5854	0,4807	2,33E-14

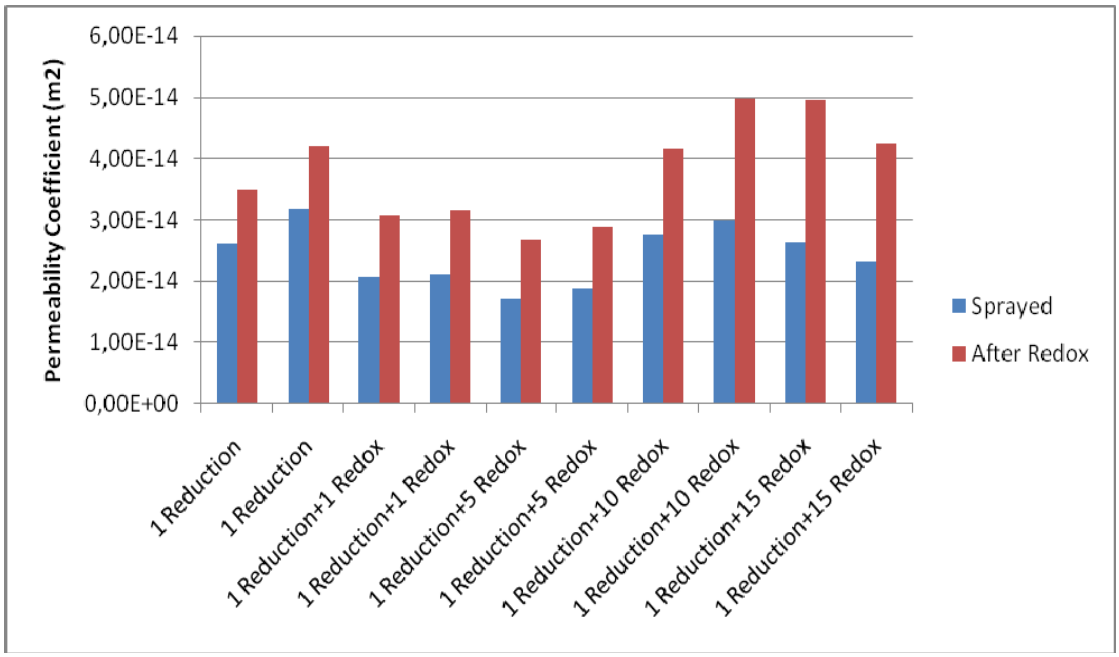

Figure 6.25 The comparision of permeability coefficients betweeen sprayed cells and redox cycled cells

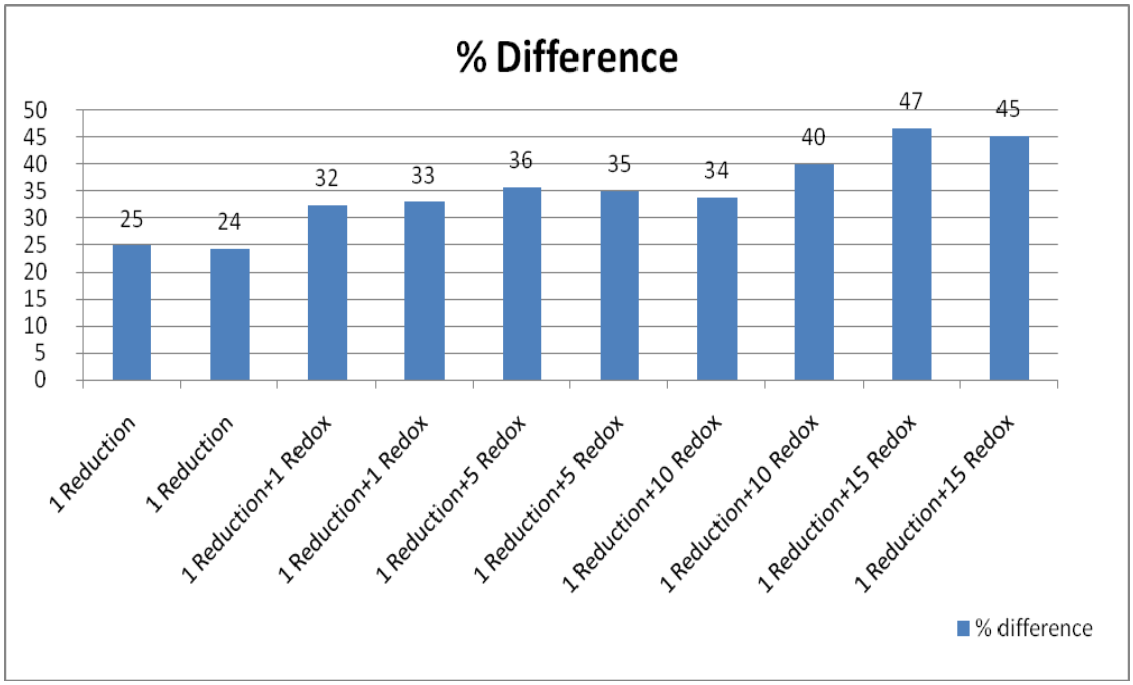

Figure 6.26 The percentage difference of the permeability between sprayed cells and redox cycled cells

At the first run, only reduction was performed, the permeability coefficient was nearly % 25. It was the reason of oxygen replacement in the NiO molecules at the anode side. After the second run, the permeability coefficient began to increase while running of redox cycles. The anode layer became denser after long operation hours due to sintering of the Nickel particles at 800 ºC. The volume flow of fuel gas supply, which reached to the TPB, could reduce through the increment of diffusion polarisation. Hence, the diffusion polarisation increment would decrease the cell performance. On the other side, sintering of the particles avoided the flexibility of the anodes under the redox atmosphere. Thus, this caused the formation of the cracking on the anode side. As well as, the substrate had a same behaviour at high operation temperature. The amount of cracking directly depended on the number of the redox cycles, as can be seen on the Figure 6.25 and Figure 6.24.

The reason of the cracking was not only sintering of the particles, but also the volume change of the anode due to the oxidation and reduction. However, the permeability coefficient did not have an extreme change on account of the redox cycles. It was predicted before the experiments because of the nanostructured anode particles. Anode side was prevented from sintering of the particles and volume change by nanostructured anode particle.

7. CONCLUSIONS

In the auxiliary application, besides the need of high efficiency and power density, the power generation system should also be capable of thermal and reduction oxidation cycling. The aim of this work was to evaluate the redox and long term stability of the SOFCs which was produced by air plasma spray technology.

One of the basic components of SOFC is anode, which brings fuel for electrochemical oxidation at the triple phase boundary, takes back the reaction products and transports electrons from reaction site to the external circuit. Nickel and yttria stabilized zirconia cermet is the most commonly used anode material due to its long term stability and commercial availability. Nickel has excellent catalytic activity and high electronic conductivity. However, the coefficient of thermal expansion (CTE) of nickel mismatches with that of electrolyte (normally fully stabilized YSZ) and nickel may agglomerate at operation temperature. YSZ is added around the Nickel particles in order to counter these issues. Ni/YSZ particle size, volume ratio and distribution are the important parameters for defining the internal resistance, porosity, active surface area and polarization resistance of the anode functional layer. Moreover, the cermet behaves as a mixed ionic electronic conductor (MIEC), increasing the active area for electrochemical reactions and combined with large internal surface in the porous structure may lead to low overpotential.

However, YSZ-Ni anode layer suffers from redox (reduction-oxidation) cycling. Ni can re-oxidize owning to numerous reasons such as switching off the system, breaking off the fuel supply, seal leak, etc, thus it is paramount to be reduced before the operation. During redox cycle nickel has a noticeable bulk volume change. Theoretically NiO contracts by 40.9% upon reduction into Ni and expand by 62% upon re-oxidation to NiO. Though the porosity of the anode functional layer in the SOFC may compensate for some of this volume change, significant volume changes were previously reported. This volume change may cause significant degradation of performance of the SOFC due to micro cracking of anode and electrolyte and delamination at the anode-electrolyte interface. In previous work in DLR, it was reported an increase in the conductivity of the anode as the function of time under

reducing atmosphere which was associated to agglomeration and partial sintering of Ni particles.

In case of sintered cells, redox cycling was reported to create cracks in the anode which propagate into electrolyte causing the failure of the cell. Contrarily, in metal supported plasma sprayed SOFC of the DLR's previous work, no change in the OCV was measured due to redox cycling. During redox cycles, however, the internal resistance of the anode was measured and a dramatic increase in the polarization resistance was recorded. Consequently, the power density has a declination. Three causes were considered to lead to this effect: 1) increase in the internal resistance of the anode; 2) delamination at the interface of anode/electrolyte and 3) oxidation of the substrate during the redox cycle, forming Cr_2O_3 rich oxide scale.[i]

The present work nanostructured Ni+YSZ anode layers were fabricated by vacuum plasma spray. Vacuum plasma spray is the one of the cell production technique which has discrete advantages such as, short fabrication time, simple automation and quality of cell layers [12].Notably, nano particle size can be produced with different parameters by thermal plasma spray. By this way, higher cell performance and much closer structure with anode and electrolyte were predicted.

Electrochemical analyse was used to investigate the losses mechanism in this master thesis. After the fabrication of the cells, four cells (ITMBEK 061162-63-64-65) were mounted in the same test bench DLR 11 (see section 5.2) in order to have comparable results. The SOFC test bench, DLR11, was designed for the electrochemical measurement for four cells. The electrochemical performance of the cells was evaluated by current-voltage curve and electrochemical impedance spectroscopy. The total measurement hours were 328 hours. The impedance spectra were also recorded using the same device (Zahner IM6) for each measurement (see section 5.2.6). The resulting data were related to the effective area of the cell to compare the results with other cells which have different size. The main parameters used in the evaluation were the OCV [V], the power density [mW/cm²], the ohmic and polarization resistances [Ωcm²].

In this work and also in previous works at DLR, it was found that the material and structure of the component has a strong influence not only on the microstructure but also on the electrochemical performance of the fabricated cells.

At the standard conditions, (13h, 81h, 112h,134h), the cells had nearly the same OCV performances (1089-1093 mW). The most interesting and unexpected point was the change in the power density value. It was 302 mW/cm^2 at 13. operation hour than it suddenly decreased to 276 mW/cm^2 at 81. operation hour. After nearly 100 hours, it has rising inclination. This unpredictable power density behaviour was explained by the new short cut way between platinium and nickel element. These short cuts way improved the transportation of the electron from the TBP to the external circuit of the anode.

At the gas variation (81h, 85h, 88h, 93h), the OCV values were between 1056 and 1137 mV. This range expressed better performance comparing with the previous works which were carried out in DLR 11 at the same condition. The OCV values were between 900 and 1000 mV in previous experiments. The amount of the oxygen negatively affected the OCV value because of the voltage difference at the beginning of the operation. Just the opposite, the power density values were relatively increased from the amount of oxygen because of the high partial pressure of the oxygen at the TPB. The most effective performance was shown at the $1H_2$+$2O_2$ due to the highest partial pressure of the hydrogen and oxygen. The power density value were 404 mW/cm^2, it was the highest value within the previous gas variation experiments in DLR 11. The results from fuel gas variation (134h, 136h, 139h, 141h) was that the degradation in the hydrogen supply obviously affected the cell performance, because the TPB could not be reached fuel gas sufficiently. Additionally, the temperature inside the test bench increased independently from the furnace temprature control at the highest partial pressure of the hydrogen. Direct exothermal combustion of H_2, was occured in the furnace due to cell leakages and that is increased the measured cell temperature.

To investigate the cell performance, the permeability and leak rate analyse were performed. Less or no cracking were existed on this type of electrolyte and anode during the redox cycle. In the furnace, five runs have carried out under the reduction and oxidation atmospheres. Between the first run and the fifth run the % difference value were varied in the range of 14 % and 48% in the leak rate measurement. It means that there were not any magnificent delamination and cracking problem in the electrolyte. From this point, it is clear that there is not an integration problem between anode and electrolyte due to the volume change of the NiO particles. The

permeability analyse results were matched with the leak rate measurement results. The % difference were varied between 25% and 47%, it was nearly the same with the leak rate results. This range was explained by nanostructured Ni+YSZ anode layers which have very good mechanical performance when compared with previous master thesis in DLR.

At the temperature variation (112h, 116h, 121h, 123h), the power density depended on the temperature. Power density directly increased when the temperature were raised. That's the reason that the electrochemical reactions required less activation energy at higher temperature. The long term operation is caused to increase the amount of activation energy because of the activation polarization during the operation.

The furnace and the electrochemical test results were demonstrated that the nanostructured Ni+YSZ anode layers fabrication with the air plasma spray had high cell performance. Besides, nano particles NiO+YSZ were provided efficient cell reactions surface and much closer structure with anode and electrolyte. Moreover, that was supported by the SEM analyse which showed the microstructure changes. In conclusion, the electrochemical test and leak rate as well as permeability analysis proved that nanostructured anode provided less or no cracking and delamination on the cell during the redox cycles.

REFERENCES

[1] Singhal, S. C. and Kendal, K., 2002, *High Temperature Solid Oxide Fuel Cells: fundemantels, design and application* , New York Elsevier Advanced Technology, Newyork.

[**2] Appleby, A. J., Foulkes, F. R**., 1989, *Fuel Cells Handbook,* Von Nostrand Reinhold, New York.

[3] Larminie, J., Dicks, A., 2000, *Fuel Cells System Explained,* Wiley, Chichester, England.

[4] Scholta, J. Lecture, 2007, Offenburg Fachhochschule of Applied Science

[5]http://www.nfrcrc.uci.edu/images/yellow/FUELCELLDİAGRAM.gif, 06.05.2007

[6] Governer, G. D., June 2000, *Analyses and Technology Transfer for Fuel Cell Systems,* California Energy Commission, California

[7] EG&G Technical Services Inc, November 2004, *Fuel Cell Handbook*, US Department of Energy Office of Fossil Energy, Morgantown, West Virginia

[8]http://www.nature.com/nature/journal/v414/n6861/images/414345aa.2.jpg,

05.07.2007

[9] Hoogers, G., 2003, *Fuel Cell Technology Handbook,* CRC Press, London

[10] www.seca.doe.gov. Surdoval, W., Williams, M., (National Energy Technology Lab.) McVay, G., Sing, P.,(Pacific Northwest National Laboratory), (2002), SECA program plan

[11] Ajmal, M., 2005, Develeopment of Test Benech for High Temperture Leak Rate Measurement of Plasma Sprayed Solid Oxide Fuel Cells, *Master Thesis*, Hamburg Technical University, Deutsches zentrum für Luft- und Raumfahrt Stuttgart.

[12] Kholwad, T, 2005, Electrical and Electrochemical Characterization of Vacuum Plasma Sprayed Functional Layers in Solid Oxide Fuel Cells, *Master Thesis,*

University of Applied Sciences in Offenburg, Deutsches zentrum für Luft- und Raumfahrt Stuttgart.

[13] **Leo, J. M., Blomen, J., Mugerwa**, M., N., 1993, *Fuel Cell Systems*, Plenum Press, Newyork

[14] Kurzweil P.; 2003, *Brenstoffzellentechnik*, Friedr. Vieweg& Sohn Verlag/GWW fachverlage GmbH, Wiesbaden

[15] **Barbir, F.,** 2005, *PEM Fuel Cells: Theory and Practice*, Elsevier Academic Press, Boston

[16] **Srinivasan, S.**, *Fuel Cells: From Fundamentals to Applications.* Springers, Newyork.

[17] **Ilhan Z.,** 2005, Electrochemical Characterization of Vacuum Plasma Sprayed SolidOxide Fuel cells For Mobile Application under Dynamic Operating Conditions, *MasterThesis*, University of Applied Sciences Offenburg, Deutsches zentrum für Luft- undRaumfahrt Stuttgart.

[18] Auer, C.,2006, Elektrochemische Charakterisierung von SOFC Brennstoffzellen Short-Stacks für mobile Anwendungen, *Diplomarbeit,* Fachhochschule Furtwangen Für Technık Und Wırtschaft Unıversıty Of Applıed Scıences, Deutsches zentrum für Luft- und Raumfahrt Stuttgart

[19] Bareoukov, E,. Macdonald J. R., 2005, *Impedance spectroscopy, theory, experiment, and application*, Wiley, England

[20] http://en.wikipedia.org/wiki/Electrical_resistance, 20.04 2007

[21] Gao, W. and Sammes, N.M. 1999. *An Introduction to Electronic and Ionic materials*. World Scientific Co. New Jersey.

[22] Thomas F., et. Al., 2004, investigation of porous metallic substrates for plasma sprayed thin film SOFC, *Fuel Cell Forum*, Lucerne, 28 June-2 July, CH. P9.

[23] Mihn, N. Q., 1995. Science and Technology of Ceramic Fuel Cells, Elsevier. Amsterdam.

[24] Ivers-Tiffée, E. Lecture; 2000, Werkstoffe für die Energ- und Umwelttechnik, Institut für Werkstoffe der Elektrotechnik, Universität Karlsruhe.

[25] Ralph, J.M. 2002. *Materials for low-temperature solid oxide fuel cells*. Argonne NationalLaboratory, Argonne.

[26] Franco T., Lang M., Schiller G. and Szabo P. 2004. Powder Metallurgical High Performance Materials for Substrate-Supported IT-SOFCs.. *Proc. from 6th European SOFC Forum*, Lucerne, June 28 – July 2, CH p.101

[27] Kerzenmacher, Sven. Solid Oxide Fuel Cell (SOFC) with thin electrolyte and novel cathodes, *Master Thesis*, p.88 Offenburg University of Applied Sciences in Offenburg.

[28] Singhal, S.C., 2000, Advances in Solid Oxide Fuel Cell Technology. *Solid State Ionics* **135**, 305-313

[29] Glatz W.,Kunschert G., Franco T., Lang M., Schiller G., Szabo P., 2004, Powder Metallurgical High Performance Materials for Substrate-Supported IT-SOFCs, *Plansee Aktiengesellschaft, Werstoffwoche,* DLR, Stuttgart

[30] Franco T., Traude H., Lang M., Ruckdäschel R. and Schiller G., *2001*, Powder Metallurgical High Performance Materials*.15th International Plansee Seminar, Reute,* vol.**4***, 64-68.*

[31] HoshiarDin, Z., 2005, Qualification of Perovskite-type LaCrO3 powders for plasma sprayed diffusion barrier layer at substrate-anode interface in SOFC, *Master Thesis*, University of Applied Sciences Offenburg, Deutsches zentrum für Luft- und Raumfahrt Stuttgart.

[32] Zheng, R., 2005, A study of Ni + 8YSZ/8YSZ/La0.6Sr0.4CoO3− ITSOFC fabricated by atmospheric plasma spraying, *Journal of Power Sources,* **140**, 217–225

[33] Franco, Thomas, et al., 2004, Investigation of Porous Metallic Substrates for Plasma Sprayed Thin-Film SOFC, *Fuel Cell Forum*, June 28-2 July 2004; Lucerne, CH. p 9.

[34] Henne, R., et. al. 2000. *3rd European Congress on Thermal Plasma Processes*, Vol. **1166**, p.247-266 Aachen, Germany.

[35] Henne, R., Mayr, W. and Reusch, A. 1993. *Thermische Spritzk**o**nferenz*, , Vol.**152**, p7 -11, Aachen, Germany.

[36] Schaper, S.,1998, Entwicklung und Elektrochemische Charakterisierung von Vakummplasmagespritzten ZrO2-Y2O3-Festelektrolyten für die SOFC, *Diplomarbeit*, University of Siegen, Siegen.

[37] The science and engineering of thermal spray coatings,; Lech Pawlowski **ISBN:** 0471952532

[38] Müller, C. A., Herbstritt, D., Ivers, E., 2002, Development of a multilayer anode for solid oxide fuel cells, *Solid State Ionics,* **152**, 537-542

[39] Spacil, H. S., 1970, *United Stated Patent 3*,No: 558, dated 31.03.1967.

[40] Maier, S. April 2004. Elektrochemische und mikrostrukturelle Charakterisierung vakuumplasmagesprizter Kathoden-Elektrolyte-Grenzflächen bei SOFC, Diplomarbeit, Technical University of Munich, Deutsches zentrum für Luft- und Raumfahrt Stuttgart.

[41] Zhu, W.Z. and S.C. Deevi. 2003. A review on the status of anode materials for solid oxide fuel cells, *Material Science and Engineering,* **A362**, 228-339.

[42] Vogler, M., et. Al.,2006, Towards an Understanding of Ni Anodes in Solid Oxide Fuel Cells: Electrochemical Modeling and Experimental Validation Using Patterned Anodes, *7th European SOFC Forum*, Lucerne, Switzerland, July 3-7, paper B073

[43] Metzger, P., June 2002. Elektrochemische Charakterisierung von vakuumplasmagespritzten Hochtemperatur-Brennstoffzellen (SOFC) in metallischen Gehäusen, *Diplomarbeit*, University of Stuttgart,Stuttgart

[44] Atkins, A,. et. Al., 2004, Advanced anodes for High Temperature Fuel Cells, *Nature Materials*, **Vol. 3**, Issue 1, p. 17-27.

[45] Cuenca, M., M., 2002, Novel Anode Materials For Solid Oxide Fuel Cells, *PhD Thesis,* University of Twente, Santander,Spain

[46] W. G. Bessler, D. G. Goodwin, and J. Warnatz, 2006, The influence of equilibrium potential on electrochemical kinetics of SOFC anodes, *Proceedings of the 7th European Solid Oxide Fuel Cell Forum*, Lucerne, Switzerland .

[47] Waldbillig, D., Wood, A., Ivey,D.G, 2005, Electrochemical and microstructural characterization of the redox tolerance of the solid oxide fuel cells anodes, *Journal of power Sources,* **145,** 206-215.

[48] Pusz, J., Smirnova, A., Mohammadi, A., Sammes, N. M., 2007, Fracture strength of micro-tubular solid oxide fuel cell anode in Redox ycling experiments, *Journal of power Sources,***163**, 900-906.

[49] Müller, A.C., Herbstritt, D., Ivers, E., 2002, Development of multilayer anode for solid oxide fuel cells,*Solid State Ionics,* **152-153**, 537542

[50] Waldbillig, D., Wood, A., Ivey, D.G., 2005, Thermal analysis of the cyclic reduction and oxidation behaviour of SOFC anodes, *Solid State Ionics,* **176,** 847-859

[51] Reichle S. December 2002. Charakterisierung von neuartigen Elektrolyt-Kathoden-Grenzflächen bei SOFC [Diplomarbeit]. Kaiserslautern: University of Kaiserslautern. p. 97

[52] MacDonald, Ross, J. 1997. *Impedance Spectroscopy: Emphasizing Solid Materials and Systems*, p. 346, John Wiley & Sons, New York.

[53] Richter F., Schiller C.A., Wagner N., Hoffmann J. 2002. *Advances in electrochemical applications of impedance spectroscopy*. ZAHNER-Elektrik GmbH, Stuttgart.

[54] Boillot, P., 2006, Electrochemical Characterization of a Substrate-Supported Solid Oxide Fuel Cell Fabricated by Plasma Spraying Process, *Industrial Application İntership Report,* Materiaux Electrochimie Genie des Procedes, DLR Stuttgart.

APPENDIX A

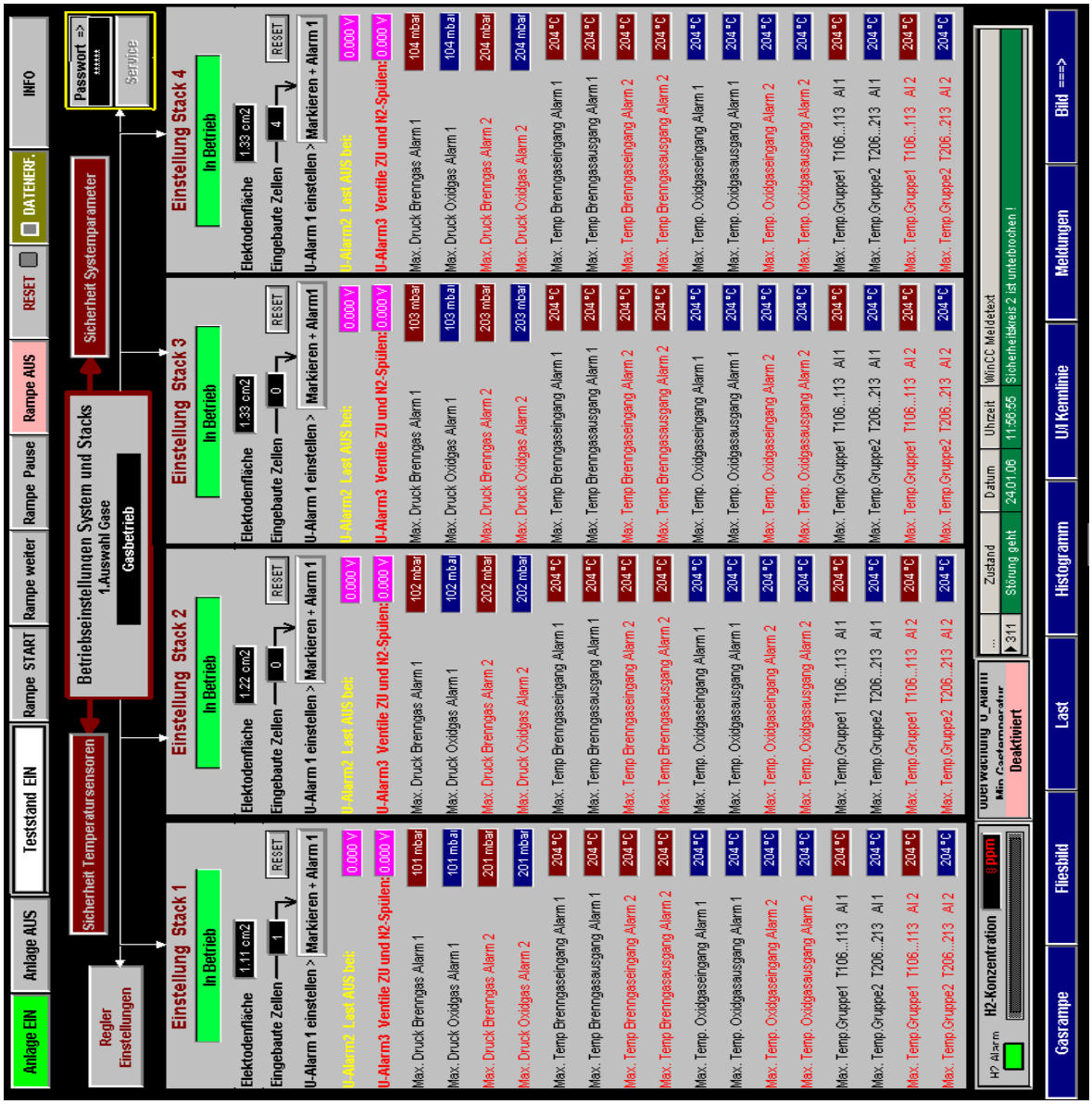

Figure A.1 Flow Chart

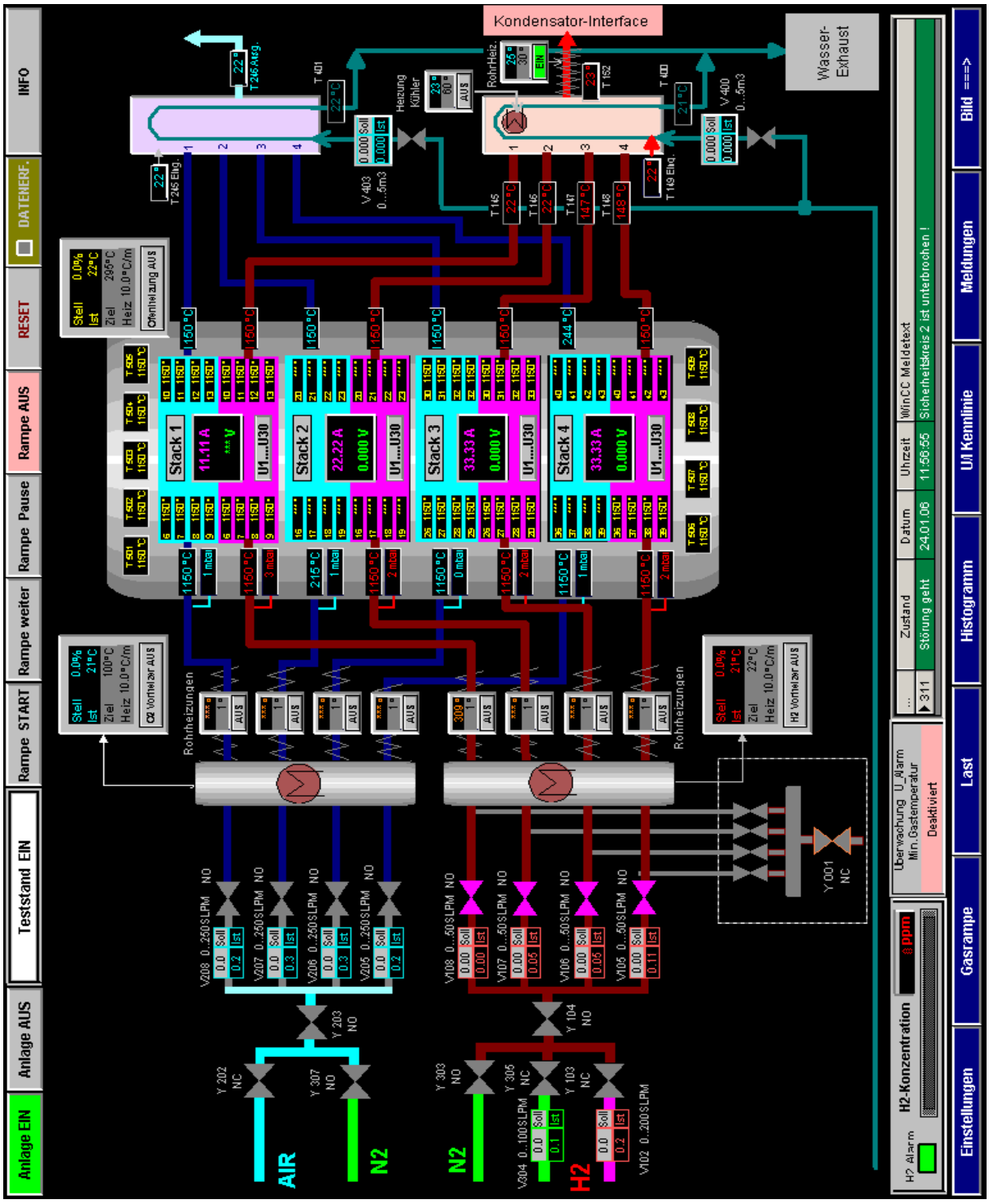

Figure A.2 Visulization of Flow Chart

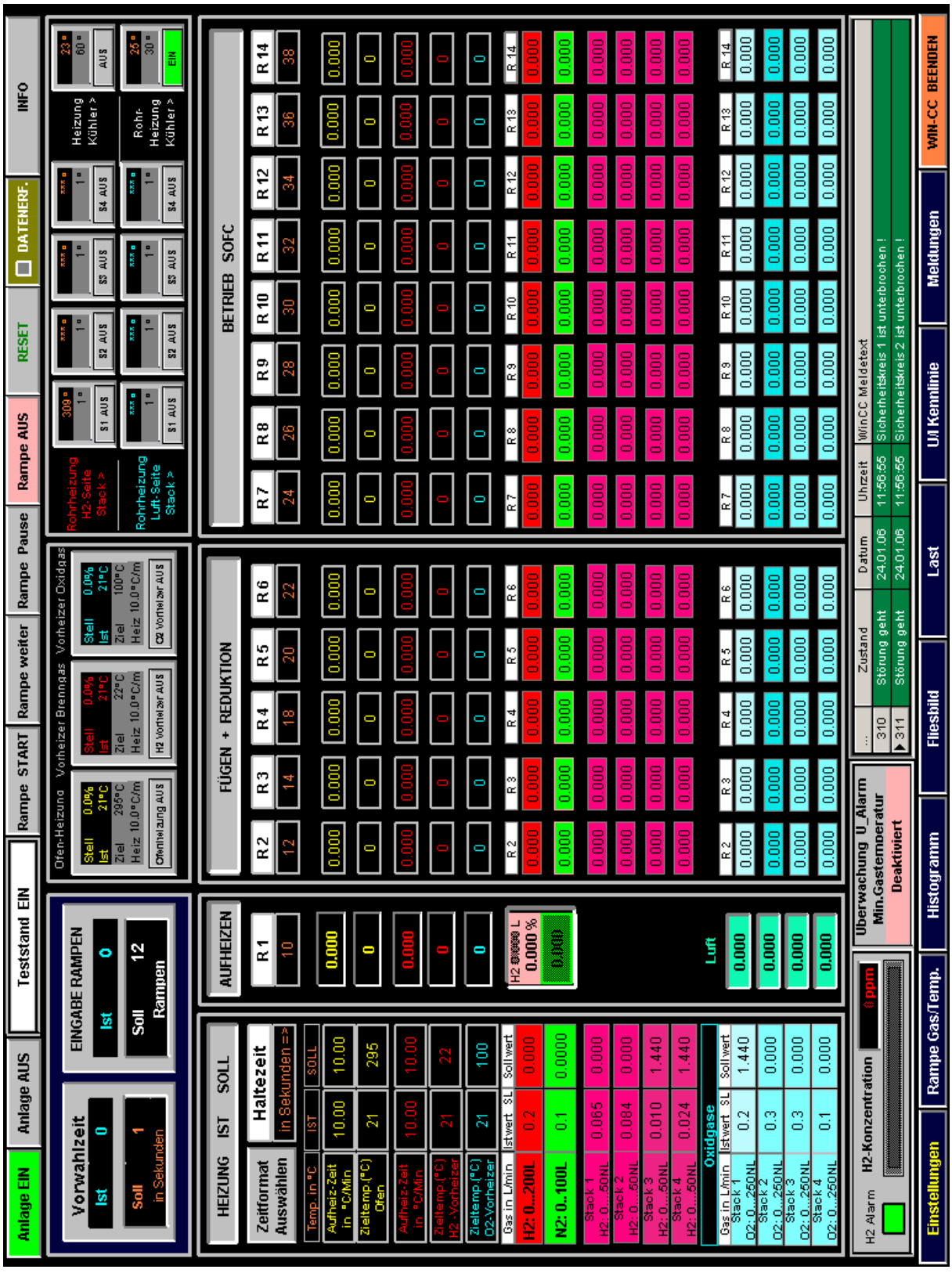

Figure A.3 Visualization of the Gas Ramp

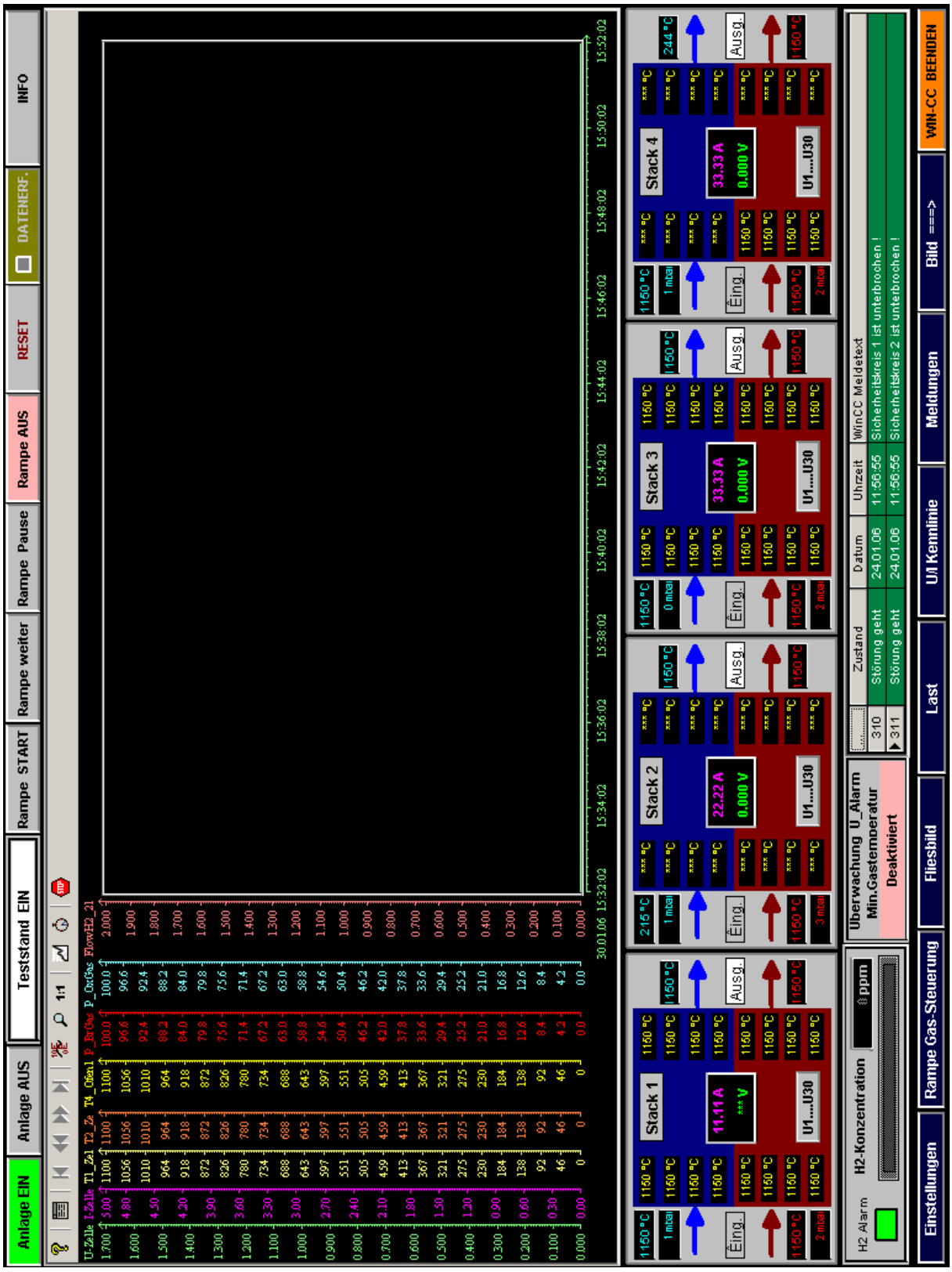

Figure A.4 Visualization of the histogramm

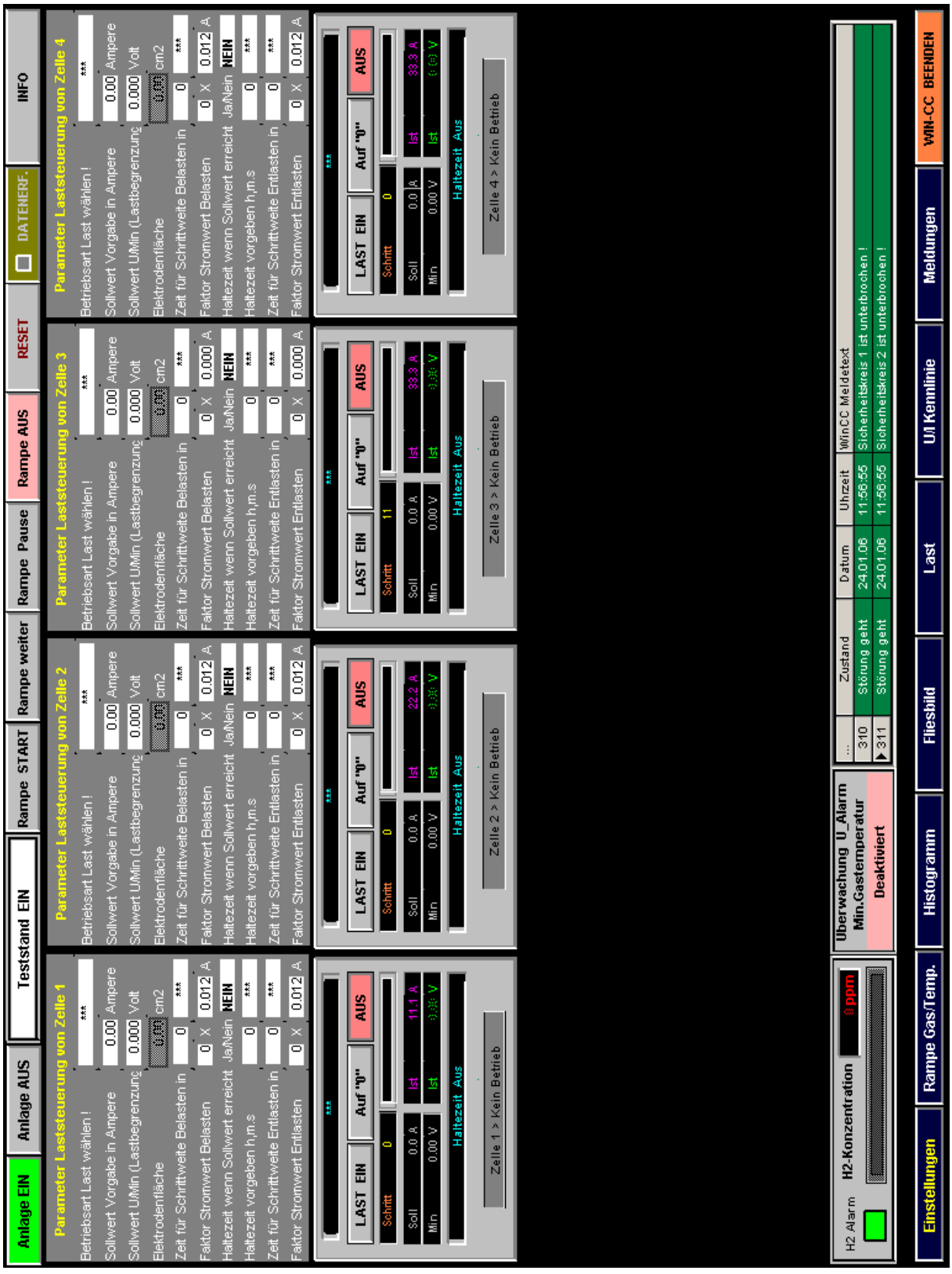

Figure A.5 Visualization of the load regulation

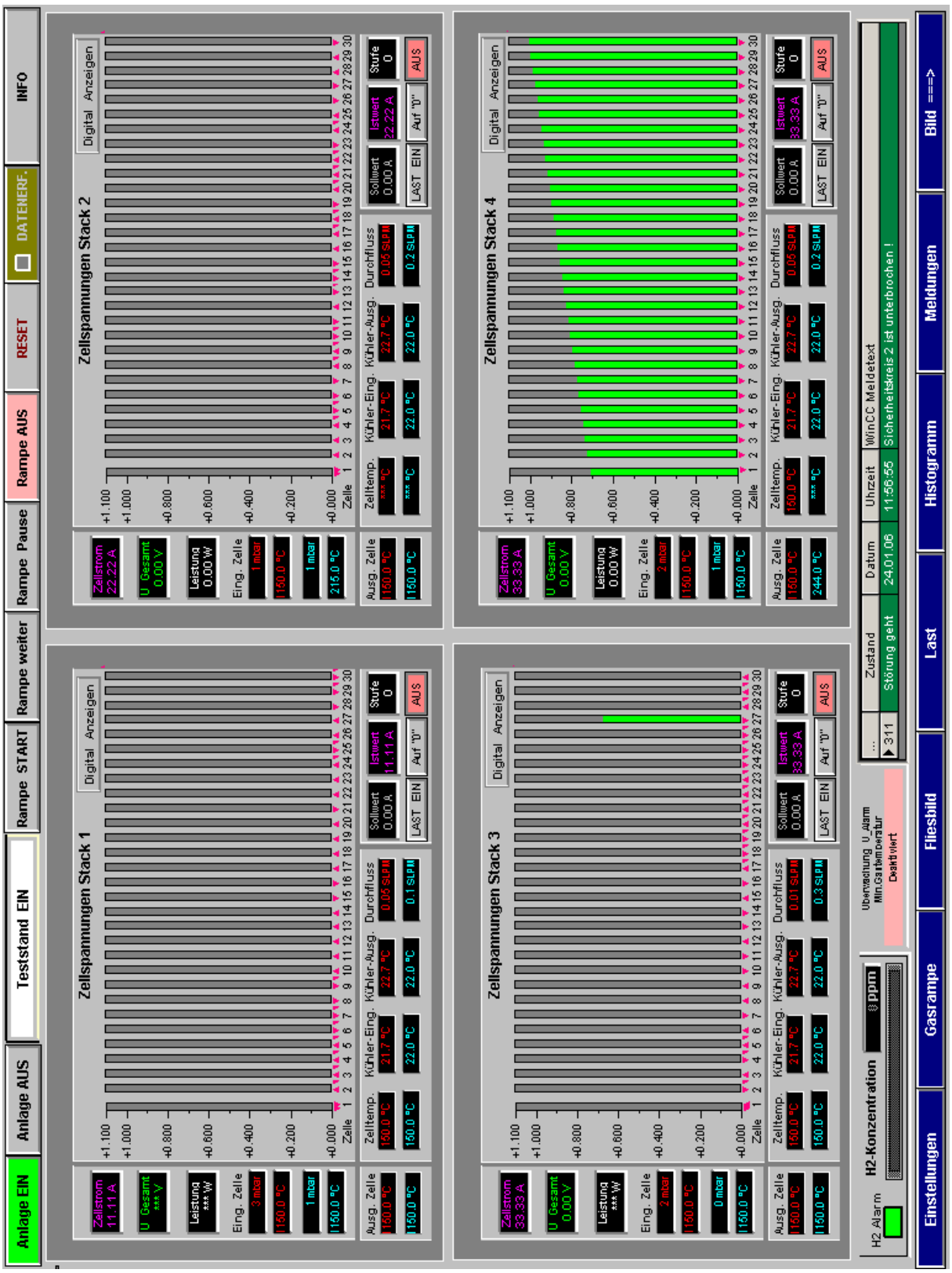

Figure A.6 Visualization of V- I Curve

Appendix B

Table B.1

Date	Date Nr.	t [h]	test	Cell T [°C]	Furnace T [°C]	Fuel gas [lpm]	Oxidgas [lpm]	OCV (initial)	Power Densıty (mW/cm2)	R(ohmic) [mOhm]	R(ges) [mOhm]	R(ohm) [Ohm/cm²]	R(pol) [Ohm/cm²]	R(pol) [Ohm/cm²]2
15.03.07	Heating	18:00	Heating	25,2		0,25 Formier	0,25 Air	1						
		01:00 =		896,2		0,25 Formier	0,25 Air	891						
16.03.07	Reductio	9h	Red Start	795,6		0,25 Formier	0,25 Air	925						
		10h	Red End	798,9		0,5 H2 0,5 N2	2,0 Air	1089						
	Activatio	13h	Activation	800,9	782	0,5 H2 0,5 N2	2,0 Air	1091	302					
	ak	14h	is ocv	800,7		0,5 H2 0,5 N2	2,0 Air	1089		109,3	42,41	1,37	0,53	0,84
	at		is 200	801,2		0,5 H2 0,5 N2	2,0 Air	893		65,69	42,14	0,83	0,53	0,30
		62 h / 0,5 H2+0,5 N2/ 2 Air 2,5A Long term Loading												
19.03.07	6	81h	V-i	800,0	782	0,5 H2 0,5 N2	2,0 Air	1092	275,8					
			is ocv	799,6		0,5 H2 0,5 N2	2,0 Air	1091		121	45,77	1,52	0,58	0,95
			is 200	799,0		0,5 H2 0,5 N2	2,0 Air	872		69,86	45,44	0,88	0,57	0,31
	7	85h	V-i	801,0	780	0,5 H2 0,5 N2	2,0 O2	1056	328,7					
			is ocv	801,1		0,5 H2 0,5 N2	2,0 O2	1055		64,74	41,36	0,81	0,52	0,29
			is 200	801,0		0,5 H2 0,5 N2	2,0 O2	905		56,76	40,76	0,71	0,51	0,20

	8	**88h**	**V-i**	**807,0**	**780**	**1,0 H2**	**2,0 O2**	**1096**	**404,3**					
			is ocv	**806,9**		**1,0 H2**	**2,0 O2**	**1099**		**55,55**	**34,23**	**0,69**	**0,43**	**0,27**
			is 200	**806,8**		**1,0 H2**	**2,0 O2**	**970**		**48,47**	**34,1**	**0,62**	**0,43**	**0,18**
	9	**93h**	**V-i**	**800,8**		**1,0 H2**	**2,0 Air**	**1137**	**380,5**					
			is ocv	**800,8**		**1,0 H2**	**2,0 Air**	**1130**		**106**	**34,44**	**1,33**	**0,43**	**0,90**
			is 200	**801,0**		**1,0 H2**	**2,0 Air**	**950**		**58,9**	**34,15**	**0,74**	**0,43**	**0,31**
20.03.07	**11**	**112h**	**V-I**	**800,5**	**782**	**0,5 H2 0,5 N2**	**2,0 Air**	**1093**	**368,8**					
			is ocv	**800,3**		**0,5 H2 0,5 N2**	**2,0 Air**	**1092**		**108,3**	**30,34**	**1,34**	**0,43**	**0,98**
			is 200	**800,4**		**0,5 H2 0,5 N2**	**2,0 Air**	**917**		**55,26**	**30,42**	**0,70**	**0,38**	**0,31**
	12	**116h**	**V-I**	**850,2**	**833**	**0,5 H2 0,5 N2**	**2,0 Air**	**1083**	**472**					
			is ocv	**850,6**		**0,5 H2 0,5 N2**	**2,0 Air**	**1083**		**96,29**	**21,23**	**1,18**	**0,31**	**0,94**
			is 200	**850,4**		**0,5 H2 0,5 N2**	**2,0 Air**	**939**		**42,86**	**21,26**	**0,59**	**0,31**	**0,27**
	13	**121h**	**V-I**	**702,0**	**682**	**0,5 H2 0,5 N2**	**2,0 Air**	**1109**	**178,6**					
			is ocv	**702,2**		**0,5 H2 0,5 N2**	**2,0 Air**	**1105**		**172,2**	**62,25**	**2,16**	**0,78**	**1,38**
			is 200	**702,1**		**0,5 H2 0,5 N2**	**2,0 Air**	**702,**		**105,3**	**62,85**	**1,32**	**0,79**	**0,53**
	14	**123h**	**V-I**	**751,2**	**732**	**0,5 H2 0,5 N2**	**2,0 Air**	**1101**	**278,7**					
			is ocv	**750,4**		**0,5 H2 0,5 N2**	**2,0 Air**	**1100**		**127**	**41,03**	**1,59**	**0,52**	**1,08**
			is 200	**750,6**		**0,5 H2 0,5 N2**	**2,0 Air**	**879**		**71,51**	**40,87**	**0,90**	**0,51**	**0,39**
21.03.07	**16**	**134h**	**V-I**	**800,8**	**782**	**0,5 H2 0,5 N2**	**2,0 Air**	**1093**	**407,1**					

			is ocv	801,2		0,5 H2 0,5 N2	2,0 Air	1091		104,3	26,52	1,31	0,33	0,98
			is 200	801,2		0,5 H2 0,5 N2	2,0 Air	926		51,13	26,24	0,64	0,33	0,31
	17	136h	V-I	801,0	784	0,25 H2 0,25 N2	2,0 Air	1077	383,3					
			is ocv	800,9		0,25 H2 0,25 N2	2,0 Air	1076		101,3	26,6	1,27	0,33	0,94
			is 200	801,0		0,25 H2 0,25 N2	2,0 Air	912		52,16	26,21	0,65	0,33	0,33
	19	139h	V-I	801,1	785	0,125 H2 0,125	2,0 Air	1048	335,8					
			is ocv	801,1		0,125 H2 0,125	2,0 Air	1048		94,84	26,24	1,22	0,33	0,86
			is 200	801,2		0,125 H2 0,125	2,0 Air	886		62,02	26,47	0,66	0,33	0,45
	21	141h	V-I	801,2	786	0,0625 H2	2,0 Air	1002	225,9					
			is ocv	801,3		0,0625 H2	2,0 Air	1000		96,93	26,06	1,18	0,33	0,89
			is 200	801,3		0,0625 H2	2,0 Air	880		52,16	26,21	0,78	0,33	0,33
22.03.07	23	159h	V-I	800,3	782	0,5 H2 0,5 N2	2,0 Air	1093	411,42					
			is ocv	800,3		0,5 H2 0,5 N2	2,0 Air	1091		104,8	25,46	1,32	0,32	1,00
			is 200	800,3		0,5 H2 0,5 N2	2,0 Air	926		50,75	25,62	0,64	0,32	0,32
	24	162h	V-I	801,0	780	0,5 H2 0,5 N2	2,0 O2	1056	509,8					
			is ocv	800,8		0,5 H2 0,5 N2	2,0 O2	1055		49,19	24,65	0,62	0,31	0,31
			is 200	800,8		0,5 H2 0,5 N2	2,0 O2	945		40,37	24,39	0,51	0,31	0,20
	25	164h	V-I	801,6	775	1 H2	2,0 O2	1102	624,8					
			is ocv	801,6		1 H2	2,0 O2	1101		65,26	25,07	0,82	0,32	0,51

			is 200	801,6		1 H2	2,0 O2	995		44,66	24,78	0,56	0,31	0,25
	26	166h	V-I	800,8	778	1 H2	2,0 Air	1132	478,36					
			is ocv	800,7		1 H2	2,0 Air	1131		98,76	24,66	1,24	0,31	0,93
			is 200	800,7		1 H2	2,0 Air	972		49,65	24,41	0,62	0,31	0,32
	28	169h	V-I	801,2	782	0,5 H2 0,5 N2	0,735 O2 1,265	1073	476,1					
			is ocv	801,2		0,5 H2 0,5 N2	0,735 O2 1,265	1073		65,26	25,07	0,82	0,32	0,51
			is 200	801,2		0,5 H2 0,5 N2	0,735 O2 1,265	942		44,66	24,78	0,56	0,31	0,25
	30	171h	V-I	801,0	781	0,5 H2 0,5 N2	1,368O2 0,632	1063	497,6					
			is ocv	801,2		0,5 H2 0,5 N2	1,368O2 0,632	1063		54,92	24,74	0,69	0,31	0,38
			is 200	801,2		0,5 H2 0,5 N2	1,368O2 0,632	946		42,63	24,51	0,54	0,31	0,23
23.03.07	32	186h	V-I	800,4	783	0,5 H2 0,5 N2	1,045 N2 0,955	1105	332,2					
			is ocv	800,6		0,5 H2 0,5 N2	1,045 N2 0,955	1104		177,3	25,43	2,23	0,32	1,91
			is 200	801,6		0,5 H2 0,5 N2	1,045 N2 0,955	903		56,17	25,13	0,71	0,32	0,39
	34	187h	V-I	801,6	782	0,25 H2 0,75 N2	1,367O2 0,632	1022	396,8					
			is ocv	800,4		0,25 H2 0,75 N2	1,367O2 0,632	1022		56,98	25,1	0,72	0,32	0,40
			is 200	800,6		0,25 H2 0,75 N2	1,367O2 0,632	900		43,75	24,31	0,55	0,31	0,24
	35	189h	V-I	799,9	783	0,125 H2 0,875	1,367O2 0,632	977	259,5					
			is ocv	799,9		0,125 H2 0,875	1,367O2 0,632	977		61,15	25,62	0,77	0,32	0,45
			is 200	799i9		0,125 H2 0,875	1,367O2 0,632	840		51,68	25,12	0,65	0,32	0,33

	38	191h	V-I	800,1	784	0,0625 H2	1,367O2 0,632	934	133,4					
			is ocv	800,5		0,0625 H2	1,367O2 0,632	934		70,08	25,48	0,88	0,32	0,56
			is 150	800,6		0,0625 H2	1,367O2 0,632	845		74,95	25,2	0,94	0,32	0,63
		109 h / 0,5 H2+0,5 N2/ 2 Air 2,5A Long Term Loading												
28.03.07	40	300h	V-I	800	778	0,5 H2 + 0,5 N2	2,0 Luft	1113	385,42					
			is ocv	800	778	0,5 H2 + 0,5 N2	2,0 Luft	1102		119,2	32,28	1,498	0,41	1,09
			is 200	800	778	0,5 H2 + 0,5 N2	2,0 Luft	921		60,22	32,18	0,757	0,40	0,35
	41	304h	V-I	850	827	0,5 H2 + 0,5 N2	2,0 Luft	1104	730,63					
			is ocv	850	827	0,5 H2 + 0,5 N2	2,0 Luft	1102		105	23,67	1,320	0,30	1,02
			is 200	850	827	0,5 H2 + 0,5 N2	2,0 Luft	942		48,02	23,65	0,604	0,30	0,31
	42	324h	V-I	700	677	0,5 H2 + 0,5 N2	2,0 Luft	1129	197,5					
			is ocv	700	677	0,5 H2 + 0,5 N2	2,0 Luft	1125		190,6	59,07	2,396	0,74	1,65
			is 200	700	677	0,5 H2 + 0,5 N2	2,0 Luft	714		158,9	60,99	1,997	0,77	1,23
	43	327h	V-I	750	728	0,5 H2 + 0,5 N2	2,0 Luft	1120	428					
			is ocv	750	728	0,5 H2 + 0,5 N2	2,0 Luft	1117		137,5	40,67	1,728	0,51	1,22
			is 200	750	728	0,5 H2 + 0,5 N2	2,0 Luft	856		117,8	41,39	1,481	0,52	0,96

Autobiograpy

She was born in Karasu/Adapazarı and went to Atatürk Primary School in Babaeski/Kırklareli. She continued her education in Kırklareli Anatolian High School from 1992 to 1997. Between 2000 and 2005, she studied Chemical Engineering in Istanbul Technical University. In 2005, she began her master program in Energy Institute. In her second year of master program, she was accepted as an exchange student in Offenburg University of Applied Sciences in Germany.